DESIGN AND ANALYSIS OF AN INERTIAL PROPERTIES MEASUREMENT DEVICE FOR MANUAL WHEELCHAIRS

A Thesis
Presented To
The Academic Faculty

by

Matthew R. Eicholtz

In Partial Fulfillment
Of the Requirements for the Degree
Master of Science in the
School of Mechanical Engineering

Georgia Institute of Technology
August 2010

DESIGN AND ANALYSIS OF AN INERTIAL PROPERTIES MEASUREMENT DEVICE FOR MANUAL WHEELCHAIRS

Approved by:

Dr. Aldo Ferri, Advisor
School of Mechanical Engineering
Georgia Institute of Technology

Dr. Michael Leamy
School of Mechanical Engineering
Georgia Institute of Technology

Dr. Stephen Sprigle
School of Applied Physiology
and Program in Industrial Design
Georgia Institute of Technology

Mr. Jayme Caspall
School of Mechanical Engineering
Georgia Institute of Technology

Date Approved: July 1, 2010

ACKNOWLEDGMENTS

First, I would like to thank my advisor, Dr. Aldo Ferri, for his continued support of my thesis work and his faith in my potential to be a successful researcher. I had the privilege of learning dynamics and vibrations under Dr. Ferri, and his teaching style is a model that I hope to emulate someday when I become a professor. I am also grateful to Dr. Stephen Sprigle, who first gave me the opportunity to participate in disabilities-related research. His knowledge in the area of rehabilitation engineering and assistive technology is profound and inspires me to continue along this path in future research endeavors.

Also, I would like to thank all the people in the Rehabilitation Engineering and Applied Research (REAR) Laboratory who have contributed to my research. Specifically, I want to acknowledge my fellow AMPS group members, Phuc Dao and Stanley Wang, for their assistance in the development of the iMachine. To Jayme Caspall, the leader of the AMPS team, I am thankful that he always challenged me to be the best researcher I can be. His attention to detail is unmatched, and I have learned from him the value of approaching engineering problems with great ardor and fervency. I am honored to call these people my fellow researchers, but more excited to call them my friends.

Thanks are also due to Dr. Michael Leamy for his willingness to join my thesis reading committee and his flexibility in accommodating my schedule.

I am thankful for the love and support of my family, without which I would not have made it this far. Finally, I am grateful to my beautiful girlfriend Patricia for her constant love and encouragement throughout this endeavor.

TABLE OF CONTENTS

ACKNOWLEDGMENTS iii

LIST OF TABLES vii

LIST OF FIGURES ix

LIST OF SYMBOLS xii

LIST OF ABBREVIATIONS xx

SUMMARY xxii

CHAPTER 1: INTRODUCTION 1

1.1 Purpose 1

1.2 Application 1

1.2.1 AMPS 1

1.2.2 Wheelchair Energy Estimation 2

1.3 Measuring Inertia Properties 10

1.3.1 Gravitational Pendulum Method 10

1.3.2 Torsional Pendulum Method 12

1.3.3 Rotating Platform Method 14

1.3.4 Previous Wheelchair Inertia Research 17

1.4 Summary 17

CHAPTER 2: DESIGN 19

2.1 Design Selection 19

2.2 Theory 20

2.3 Component Specification 21

2.3.1 Structural Frame....................21
2.3.2 Disk....................21
2.3.3 Shaft Assembly....................23
2.3.4 Springs....................28
2.3.5 X-Y Positioning Platform....................37
2.3.6 Hardware....................39
2.3.7 Software....................44
2.4 Summary....................48
CHAPTER 3: MEASUREMENT APPROACH....................49
3.1 Mass....................49
3.2 Center of Mass Coordinates....................49
3.3 Moment of Inertia....................50
3.3.1 Time-Domain Methods....................52
3.3.2 Frequency-Domain Methods....................52
3.3.3 Solving for the Inertia of the Manual Wheelchair....................55
CHAPTER 4: CALIBRATION....................61
4.1 Load Cell Calibration....................61
4.2 Spring Calibration....................63
CHAPTER 5: TESTING AND RESULTS....................73
5.1 Mass Validation....................73
5.2 Center of Mass Validation....................80
5.3 Moment of Inertia Validation....................83
5.4 Wheelchair Testing....................99

CHAPTER 6: CONCLUSIONS AND RECOMMENDATIONS....................................102

REFERENCES 105

LIST OF TABLES

Table 1. Half-spring constant based on desired natural period and spring moment-arm (using lower bound, 10,000 lb-in^2, of inertia range) 31

Table 2. Half-spring constant based on desired natural period and spring moment-arm (using upper bound, 40,800 lb-in^2, of inertia range) 32

Table 3. Maximum angular displacement (in degrees) based on spring parameters. 35

Table 4. Encoder state changes and their meaning 42

Table 5. Load cell calibration factors 61

Table 6. Steel brick mass and geometric properties 64

Table 7. Natural frequency (rad/s) based on time-domain and frequency-domain methods (s_1 = 50.8 mm) 67

Table 8. Natural frequency (rad/s) based on time-domain and frequency-domain methods (s_2 = 76.2 mm) 68

Table 9. Mean and standard deviation for natural frequency measurements 69

Table 10. Moment of inertia of the disk system (kg-m^2) 69

Table 11. Effective spring rate (N/m) based on time-domain and frequency-domain methods (s_1 = 50.8 mm) 70

Table 12. Effective spring rate (N/m) based on time-domain and frequency-domain methods (s_2 = 76.2 mm) 71

Table 13. Mean and standard deviation (N/m) for k_{eff} measurements 72

Table 14. Comparison of calibrated spring rate to manufacturer-provided data 72

Table 15. Accuracy of load cell mass measurement 74

Table 16. Error in mass readings due to position on platform (20.12 kg mass) 76

Table 17. Error in mass readings due to position on platform (24.73 kg mass) 78

Table 18. Center of mass validation test results 82

Table 19. Mass properties and natural frequency for iMachine validation test (one brick) with brick on platform 85

Table 20. Mass properties and natural frequency for iMachine validation test (one brick) without brick on platform 86

Table 21. Validation test (one brick): inertia of the system about the disk origin (kg-m^2) 87

Table 22. Validation test (one brick): inertia of the platform about the disk origin (kg-m^2) 88

Table 23. Validation test (one brick): inertia of the brick about the disk origin (kg-m^2) . 88

Table 24. Validation test (one brick): inertia of the brick about its CG (kg-m^2) 88

Table 25. Validation test (one brick): relative error of test object inertia (%) 89

Table 26. Validation test (four-brick configuration on platform): inertia of the system about the disk origin (kg-m^2) 93

Table 27. Validation test (four-brick configuration on platform): inertia of the platform about the disk origin (kg-m^2) 93

Table 28. Validation test (four-brick configuration on platform): inertia of the test object about the disk origin (kg-m^2) 93

Table 29. Validation test (four-brick configuration on platform): inertia of the test object about its CG (kg-m^2) 94

Table 30. Validation test (four-brick configuration on platform): relative error of test object inertia (%) 94

Table 31. Validation test (four-brick configuration on disk): inertia of the system about the disk origin (kg-m^2) 97

Table 32. Validation test (four-brick configuration on disk): inertia of the disk about the origin (kg-m^2) 97

Table 33. Validation test (four-brick configuration on disk): inertia of the test object about its CG (kg-m^2) 97

Table 34. Validation test (four-brick configuration on disk): relative error of test object inertia (%) 98

Table 35. Wheelchair inertial properties, as determined by the iMachine 100

LIST OF FIGURES

Figure 1. Coordinate axes for the wheelchair 3

Figure 2. Coordinate axes for a wheel 5

Figure 3. Rotation of casters about the swivel point 5

Figure 4. Velocity of wheelchair components during turning 7

Figure 5. Gravitational pendulum model 11

Figure 6. Bifilar gravitational pendulum model 12

Figure 7. Trifilar torsional pendulum model 13

Figure 8. Rotating platform model with falling mass [10] 15

Figure 9. Rotating platform model with torsion spring 16

Figure 10. Model of iMachine design 19

Figure 11. iMachine disk 22

Figure 12. iMachine shaft assembly 23

Figure 13. Modeling the shaft assembly as a beam in bending 25

Figure 14. Model of the spring geometry and contact point on the rotating disk 33

Figure 15. iMachine extension spring in static equilibrium 37

Figure 16. iMachine X-Y positioning platform 38

Figure 17. Load cell mounted to iMachine disk 40

Figure 18. Optical encoder components (U.S. Digital Inc.) 40

Figure 19. Encoder quadrature output 41

Figure 20. Encoder mounted to bottom of iMachine frame 43

Figure 21. LabJack U6 DAQ device 44

Figure 22. LabVIEW iMachine GUI front panel 1

Figure 23. LabVIEW iMachine GUI block diagram (data streaming section).................. 1

Figure 24. iMachine in rotation 48

Figure 25. MATLAB simulation of typical second-order underdamped transient response 51

Figure 26. Sample frequency response of SDOF system showing half-power points...... 54

Figure 27. CG schematic (initial platform position).. 56

Figure 28. CG schematic (after wheelchair is added)... 57

Figure 29. CG schematic (after moving wheelchair and platform to zero system CG).... 58

Figure 30. CG schematic (after removing wheelchair).. 59

Figure 31. Load cell A calibration data 62

Figure 32. Load cell B calibration data.. 62

Figure 33. Load cell C calibration data.. 63

Figure 34. Model of spring calibration test.. 64

Figure 35. Platform configurations for mass validation test.. 75

Figure 36. Interpolated surface plot of absolute error distribution (in kg) on platform (20.12 kg mass)... 77

Figure 37. Interpolated surface plot of absolute error distribution (in kg) on platform (24.73 kg mass)... 79

Figure 38. Static analysis of forces on iMachine platform 80

Figure 39. Time-domain response of iMachine validation test (1 block)......................... 83

Figure 40. Frequency-domain response of iMachine validation test (1 block) 84

Figure 41. Validation test model (four-brick configuration) 90

Figure 42. Comparison of the time-domain response of the system with and without the test object (four-brick configuration on platform)... 91

Figure 43. Comparison of the frequency-domain response of the system with and without the test object (four-brick configuration on platform) 92

Figure 44. Comparison of the time-domain response of the system with and without the test object (four-brick configuration on disk) 95

Figure 45. Comparison of the frequency-domain response of the system with and without the test object (four-brick configuration on disk) 96

Figure 46. Plot of relative error versus inertia ratio 99

Figure 47. Quickie GT chair mounted on iMachine 100

LIST OF SYMBOLS

α, β	angles used in spring geometric analysis
δ	deflection of a beam; deflection of a spring; log decrement
δ_{max}	maximum deflection of spring
$\Delta\theta$	encoder resolution
$\Delta\omega$	bandwidth
ε	eccentricity
ζ	damping ratio
θ	angular coordinate for harmonic motion
θ_0	initial angular displacement
$\dot{\theta}_{\mathrm{frame}}$	pitch rate about the *y*-axis of the wheelchair frame
σ_{allow}	maximum allowable normal stress
σ_y	normal yield stress
τ	input torque
$\dot{\phi}_{\mathrm{LC}}$	spin rate of the left caster
$\dot{\phi}_{\mathrm{LD}}$	spin rate of the left drive wheel
$\dot{\phi}_{\mathrm{RC}}$	spin rate of the right caster
$\dot{\phi}_{\mathrm{RD}}$	spin rate of the right drive wheel
$\dot{\psi}_{\mathrm{frame}}$	yaw rate of the wheelchair frame about the *z*-axis of an inertial reference frame fixed to ground

$\dot{\psi}_{\text{LC/frame}}$ yaw rate of the left caster with respect to the wheelchair frame

$\dot{\psi}_{\text{RC/frame}}$ yaw rate of the right caster with respect to the wheelchair frame

$\overline{\omega}$ angular velocity of a rigid body

ω_0 initial angular velocity

ω_1 fundamental frequency

ω_{cr} Nyquist critical frequency

ω_{final} final angular velocity of rotating platform

$\overline{\omega}_{\text{frame}}$ angular velocity of the wheelchair frame

ω_i natural frequency associated with the *i*th validation test

ω_k frequency associated with the *k*th Fourier coefficient

$\omega_{\max}$ maximum angular speed

ω_{n} natural frequency of a system

ω_q angular velocity component in the *q*-direction

a radial distance from the cable to the center of the lower plate in a torsional pendulum

A arbitrary axis used in discussion of parallel axis theorem; amplitude of transient response

A,B,C load cell ID

B arbitrary axis used in discussion of parallel axis theorem

c damping coefficient; chord length

C_1, C_2, C_3 constants of integration in beam analysis

d — distance between two parallel axes; distance from load cell to center of disk; diameter of circular beam cross section; depth of brick used in validation tests

D — complex frequency response

d_{A} — distance from load cell A to center of rotating disk

d_{B} — distance from load cell B to center of rotating disk

d_{C} — distance from load cell C to center of rotating disk

d_{frame} — distance from the center of gravity of the wheelchair frame to rotation axis

d_{i} — distance from the center of gravity of the component denoted by i to the rotation axis

d_{LC} — distance from the center of gravity of the left caster to rotation axis

d_{LD} — distance from the center of gravity of the left drive wheel to rotation axis

d_{RC} — distance from the center of gravity of the right caster to rotation axis

d_{RD} — distance from the center of gravity of the right drive wheel to rotation axis

d_{sys} — distance from the center of gravity of the wheelchair system to rotation axis

d_{WC2} — distance from the wheelchair center of mass to the rotation axis

E — modulus of elasticity

e_{abs} — absolute error

e_{rel} — relative percent error

F — force

F_{A} — force on load cell A; force at point A

F_{B} — force on load cell B; force at point B

F_{C}	force on load cell C
f_{min}	minimum sampling rate
F_q	force in the q-direction
F_{ratio}	force ratio used in center of mass validation test
F_{total}	total force due to weight on load cells
g	acceleration due to gravity
g_k	kth data point in the time domain
G_k	kth Fourier coefficient
h	height of cable in torsional pendulum
$\overline{H}_{\mathrm{G}}$	angular momentum of a rigid body about its center of mass
i, j, k	indices; unit vectors along coordinate axes
I	moment of inertia (general)
I_{pq}	product of inertia of a rigid body about the plane formed by the p and q-axes
I_{qq}	moment of inertia of a rigid body about the q-axis
I_{ratio}	ratio of testpiece inertia to total system inertia
$I_{\mathrm{theoretical}}$	theoretical moment of inertia
I_A^{P}	moment of inertia about axis A passing through point P
I_B^{G}	moment of inertia about axis B passing through the center of gravity
$\left(I_{qq}\right)_{\mathrm{component}}$	moment of inertia of a component about the q-axis passing through its center of gravity

$\left(I_{qq}^{\mathrm{P}}\right)_{\mathrm{component}}$	moment of inertia of a component about the q-axis passing through point P
k	linear spring constant
k_{eff}	effective linear spring rate
k_{T}	torsional spring constant
l	length of gravitational pendulum; length of steel block used in testing; length of cable between spring and contact point on disk; length of brick used in validation tests
L	total length of spring
ℓ_0	unstretched length of spring
L_1	length between bearings on shaft
L_2	length between upper bearing on shaft and top of disk
m	total mass of a rigid body
M	total mass of the system in the trifilar pendulum model; bending moment along the shaft
m_{brick}	mass of brick used for validation tests
m_{frame}	mass of the wheelchair frame
m_{LC}	mass of the left caster
m_{LD}	mass of the left drive wheel
$M_{\max}$	maximum bending moment on a beam
M_{P}	moment about arbitrary point P
m_{platform}	mass of the platform
M_q	moment about q-axis

m_{RC}	mass of the right caster
m_{RD}	mass of the right drive wheel
m_{WC}	mass of the wheelchair
n	safety factor
N	number of data points; number of test runs
P	arbitrary point
q	generalized displacement
$\dot{q}$	generalized velocity
$\ddot{q}$	generalized acceleration
q_0	initial displacement
q_{actual}	theoretical value of parameter q
q_{measured}	empirical value of parameter q
r	pulley radius; frequency ratio
R	instantaneous center of zero velocity during turning
R	radius of rotating disk; moment arm of spring force
$R_{\mathrm{A}a}$	reaction force at point A in the axial direction
$R_{\mathrm{A}r}$	reaction force at point A in the radial direction
R_{B}	reaction force at point B
$\bar{r}_{i/\mathrm{G}}$	position vector pointing from the center of gravity of the system to the center of gravity of the component denoted by i
s	distance that the mass fell in rotating platform model [10]

S	required section modulus
s_0	initial distance
s_i	distance from edge of brick to rotation axis for *i*th validation test
t	time
T	kinetic energy of a rigid body; period of oscillation; length of data record
T_{d}	damped period of oscillation
T_{frame}	kinetic energy of the wheelchair frame
T_{LC}	kinetic energy of the left caster
T_{LD}	kinetic energy of the left drive wheel
T_{n}	natural period of oscillation
T_{RC}	kinetic energy of the right caster
T_{RD}	kinetic energy of the right drive wheel
T_{sys}	total kinetic energy of a system
$T_{\mathrm{sys,trans}}$	total translational kinetic energy of the system
V	shear force
v, v', v''	deflection of a beam and its first two derivatives
v_0	initial velocity
$\bar{v}_{\mathrm{G}}$	velocity of the center of mass of a rigid body
$\bar{v}_{\mathrm{G,frame}}$	velocity of the center of gravity of the wheelchair frame
$\bar{v}_{\mathrm{G},i}$	velocity of the center of gravity of the component denoted by *i*

$\bar{v}_{\mathrm{G,LD}}$	velocity of the center of gravity of the left drive wheel
$\bar{v}_{\mathrm{G,RD}}$	velocity of the center of gravity of the right drive wheel
$\bar{v}_{\mathrm{G,LC}}$	velocity of the center of gravity of the left caster
$\bar{v}_{\mathrm{G,RC}}$	velocity of the center of gravity of the right caster
w	spring width; width of brick used in validation tests
(x_1, y_1)	coordinates of system center of mass as measured by the iMachine
(x_2, y_2)	coordinates of force at point B
$(x_{\mathrm{p1}}, y_{\mathrm{p1}})$	first location of the platform center of mass
$(x_{\mathrm{p2}}, y_{\mathrm{p2}})$	second location of the platform center of mass
$x_{\mathrm{w}}, y_{\mathrm{w}}, z_{\mathrm{w}}$	principal axes for a wheel
$(x_{\mathrm{WC1}}, y_{\mathrm{WC1}})$	first location of the wheelchair center of mass
$(x_{\mathrm{WC2}}, y_{\mathrm{WC2}})$	second location of the wheelchair center of mass
$(\Delta x_{\mathrm{p}}, \Delta y_{\mathrm{p}})$	change in location of the platform center of mass
$(\Delta x_{\mathrm{WC}}, \Delta y_{\mathrm{WC}})$	change in location of the wheelchair center of mass
X_{G}	*x*-coordinate of system center of mass
x_j	amplitude of *j*th peak in damped harmonic transient response
Y_{G}	*y*-coordinate of system center of mass
Z	phase lag of encoder quadrature signals

LIST OF ABBREVIATIONS

REAR	Rehabilitation Engineering and Applied Research
AMPS	Anatomical Model Propulsion System
3D	Three Dimensional
CG	Center of Gravity
LD	Left Drive wheel
RD	Right Drive wheel
LC	Left Caster
RC	Right Caster
MM	Modal Methods
SDOF	Single-Degree-of-Freedom
LED	Light-Emitting Diode
CPR	Cycles Per Revolution
CW	Clockwise
CCW	Counter-Clockwise
DAQ	Data Acquisition
AI	Analog Input
DI	Digital Input
PC	Personal Computer
GUI	Graphical User Interface
CSV	Comma-Separated Values
DLL	Dynamic Linked Library

FFT	Fast Fourier Transform
DFT	Discrete Fourier Transform
QF	Quality Factor
GRR	Gauge Repeatability and Reproducibility
ANOVA	Analysis of Variance

SUMMARY

The dynamics of rigid body motion are dependent on the inertial properties of the body - that is, the mass and moment of inertia. For complex systems, it may be necessary to derive these results empirically. Such is the case for manual wheelchairs, which can be modeled as a rigid body frame connected to four wheels. While 3D modeling software is capable of estimating inertial parameters, modeling inaccuracies and ill-defined material properties may introduce significant errors in this estimation technique and necessitate experimental measurements. To that end, this thesis discusses the design of a device called the iMachine that empirically determines the mass, location of the center of mass, and moment of inertia about the vertical (yaw) axis passing through the center of mass of the wheelchair.

The iMachine is a spring-loaded rotating platform that freely oscillates about an axis passing through its center due to an initial angular velocity. The mass and location of the center of mass can be determined using a static analysis of a triangular configuration of load cells. An optical encoder records the dynamic angular displacement of the platform, and the natural frequency of free vibration is calculated using several techniques. Finally, the moment of inertia is determined from the natural frequency of the system.

In this thesis, test results are presented for the calibration of the load cells and spring rate. In addition, objects with known mass properties were tested and comparisons are made between the analytical and empirical inertia results. In general, the mass measurement of the test object had greater than 99% accuracy. The average relative error

for the x and y-coordinates of the center of mass was 0.891% and 1.99%, respectively. For the moment of inertia, a relationship was established between relative error and the ratio of the test object inertia to the inertia of the system. The results suggest that 95% accuracy can be achieved if the test object accounts for at least 25% of the total inertia of the system. Finally, the moment of inertia of a manual wheelchair is determined using the device ($(I_{zz})_{\mathrm{WC}}$ = 1.213 kg-m^2), and conclusions are made regarding the reliability and validity of results. The results of this project will feed into energy calculations for the Anatomical Model Propulsion System (AMPS), a wheelchair-propelling robot used to measure the mechanical efficiency of manual wheelchairs.

CHAPTER 1

INTRODUCTION

1.1 Purpose

The dynamics of rigid body motion are dependent on the inertial properties of the body - that is, the mass and moment of inertia. For simple systems with well-defined shapes and densities, these properties can be determined analytically using closed-form formulas. For more complex systems, it may be necessary to derive these results empirically. Such is the case for manual wheelchairs, which can be modeled as a rigid body frame connected to four wheels. While 3D modeling software is capable of estimating inertial parameters, modeling inaccuracies and ill-defined material properties may introduce significant errors in this estimation technique. To address this limitation, this thesis discusses the design and analysis of a device called the iMachine that empirically determines the mass, location of the center of mass, and moment of inertia about the vertical (yaw) axis passing through the center of mass of the test piece. While the device could be used to measure the inertial properties of a variety of irregularly-shaped objects, the primary application of the iMachine is manual wheelchairs.

1.2 Application

1.2.1 AMPS

The motivation for the design and development of the iMachine is another research project at Georgia Tech's REAR Lab called the Anatomical Model Propulsion System (AMPS). The AMPS is an anthropomorphic robot capable of propelling a manual wheelchair much like a human operator. It will be used to create standardized tests for characterizing wheelchair performance. The tests will consist of a canonical set of maneuvers typically used in wheelchair propulsion. By comparing the system input work to the energy output of the chair during these maneuvers, mechanical efficiency ratings are established and comparisons can be made across chairs that will foster better wheelchair design and promote improved clinical prescription to meet the user's mobility needs.

1.2.2 Wheelchair Energy Estimation

The energy output of a wheelchair during propulsion is dominated by its kinetic energy, although potential energy effects need to be included in maneuvers involving elevation changes such as ramps or inclines. The kinetic energy, *T*, of a rigid body in general motion is given by

$$T = \frac{1}{2} m \bar{v}_{\mathrm{G}} \cdot \bar{v}_{\mathrm{G}} + \frac{1}{2} \bar{\omega} \cdot \overline{H}_{\mathrm{G}} \tag{1}$$

where m is the total mass, $\bar{v}_{\mathrm{G}}$ is the velocity of the center of mass, $\bar{\omega}$ is the angular velocity of the body, and $\overline{H}_{\mathrm{G}}$ is the angular momentum. The angular momentum can further be described by the equation,

$$\overline{H}_{\mathrm{G}} = \left(I_{xx}\omega_x - I_{xy}\omega_y - I_{xz}\omega_z\right)\bar{i} + \left(I_{yy}\omega_y - I_{yx}\omega_x - I_{yz}\omega_z\right)\bar{j} + \left(I_{zz}\omega_z - I_{zx}\omega_x - I_{zy}\omega_y\right)\bar{k} \tag{2}$$

where (I_{xx}, I_{yy}, I_{zz}) are the moments of inertia about the three coordinate axes, $(I_{xy}, I_{xz}, I_{yx}, I_{yz}, I_{zx}, I_{zy})$ are the products of inertia, and $(\omega_x, \omega_y, \omega_z)$ are the angular velocity components about each of the three coordinate axes. Note that the products of inertia simplify to three terms by using the following relationships

$$
\begin{aligned}
I_{xy} &= I_{yx} \\
I_{xz} &= I_{zx} \\
I_{yz} &= I_{zy}
\end{aligned} \tag{3}
$$

For the entirety of this thesis, the body-fixed reference frame of the wheelchair shall be defined according to the illustration in Figure 1, where point G represents the center of gravity (CG) of the system.

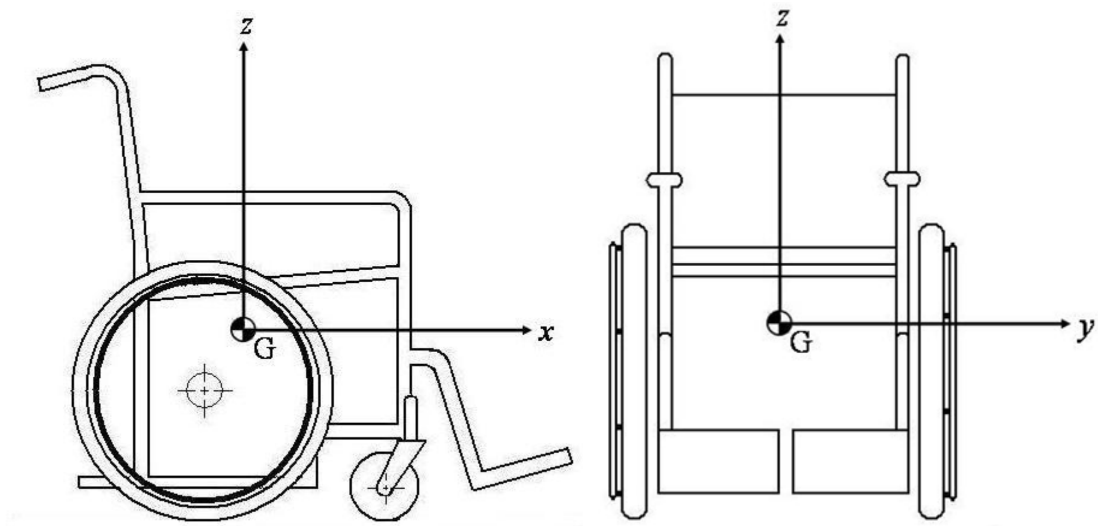

Figure 1. Coordinate axes for the wheelchair

In addition, the following convention will be used to describe the inertia terms: $\left(I_{qq}^{\mathrm{P}}\right)_{\text{component}}$ refers to the inertia of a component about the *q*-axis passing through the point P, whereas $\left(I_{qq}\right)_{\text{component}}$ refers to the inertia of a component about the *q*-axis passing through the CG of that *component*.

The chair can be modeled as a system containing multiple rigid bodies: the frame, two rear drive wheels, and two casters. The kinetic energy of each body can be calculated using (1) and simplified using the kinematic constraints of the system. The total system kinetic energy is simply the sum of these terms,

$$T_{\text{sys}} = T_{\text{frame}} + T_{\text{LD}} + T_{\text{RD}} + T_{\text{LC}} + T_{\text{RC}} \tag{4}$$

where the subscripts LD, RD, LC, and RC refer to the left drive wheel, right drive wheel, left caster, and right caster, respectively.

For this analysis, a body-fixed reference frame is introduced for each rigid body, with the origin being located at the center of mass of the respective body. To simplify the rotational kinetic energy of the frame, notice that the *x* and *z* coordinate axes form a plane of symmetry for the frame, which means that all products of inertia involving the coordinate normal to the plane (in this case, I_{xy} and I_{yz}) are zero. For small angles and assuming that the frame does not roll, it can be shown that the angular velocity is

$$\overline{\omega}_{\text{frame}} = \dot{\theta}_{\text{frame}}\bar{j} + \dot{\psi}_{\text{frame}}\bar{k} \tag{5}$$

where $\dot{\theta}_{\text{frame}}$ is the pitch rate about the *y*-axis of the frame and $\dot{\psi}_{\text{frame}}$ is the yaw rate about the *z*-axis of an inertial reference frame fixed to ground. Then, the frame kinetic energy can be simplified to

$$T_{\text{frame}} = \frac{1}{2}m_{\text{frame}}\bar{v}_{\text{G,frame}} \cdot \bar{v}_{\text{G,frame}} + \frac{1}{2}\left(I_{yy}\right)_{\text{frame}}\dot{\theta}^2_{\text{frame}} + \frac{1}{2}\left(I_{zz}\right)_{\text{frame}}\dot{\psi}^2_{\text{frame}} \tag{6}$$

In most cases, the second term in (6) will equal zero because the only time the frame should rotate about the *y*-axis is during wheelie maneuvers or approaching an incline.

To help solve for the kinetic energy of the wheels, Figure 2 shows the coordinate axes of the reference frame fixed on a wheel. These axes are principal axes, meaning that all the products of inertia equal zero.

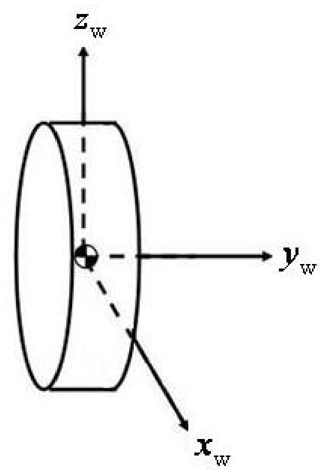

Figure 2. Coordinate axes for a wheel

It is assumed that, with respect to their body-fixed frames, both drive wheels are constrained to rotate only about the y_w -axis relative to the wheelchair frame. The casters follow the same principle with the addition that they can also rotate about the vertical axis passing through the swivel point, as shown in Figure 3. However, the AMPS researchers are neglecting the caster swivel based on the assumption that its effect is small. Still, the casters will have yaw rotational kinetic energy due to the angular velocity of the frame to which they are attached.

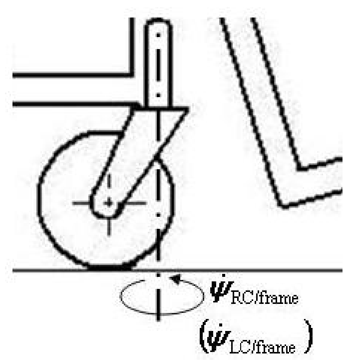

Figure 3. Rotation of casters about the swivel point

Using these constraints and considering that the pitch rate of the frame is negligible in most cases, the kinetic energy of each wheel can be determined by

$$T_{\mathrm{LD}} = \frac{1}{2} m_{\mathrm{LD}} \bar{v}_{\mathrm{G,LD}} \cdot \bar{v}_{\mathrm{G,LD}} + \frac{1}{2} \left(I_{yy}\right)_{\mathrm{LD}} \dot{\phi}_{\mathrm{LD}}^2 + \frac{1}{2} \left(I_{zz}\right)_{\mathrm{LD}} \dot{\psi}_{\mathrm{frame}}^2 \tag{7}$$

$$T_{\mathrm{RD}} = \frac{1}{2} m_{\mathrm{RD}} \bar{v}_{\mathrm{G,RD}} \cdot \bar{v}_{\mathrm{G,RD}} + \frac{1}{2} \left(I_{yy}\right)_{\mathrm{RD}} \dot{\phi}_{\mathrm{RD}}^2 + \frac{1}{2} \left(I_{zz}\right)_{\mathrm{RD}} \dot{\psi}_{\mathrm{frame}}^2 \tag{8}$$

$$T_{\mathrm{LC}} = \frac{1}{2} m_{\mathrm{LC}} \bar{v}_{\mathrm{G,LC}} \cdot \bar{v}_{\mathrm{G,LC}} + \frac{1}{2} \left(I_{yy}\right)_{\mathrm{LC}} \dot{\phi}_{\mathrm{LC}}^2 + \frac{1}{2} \left(I_{zz}\right)_{\mathrm{LC}} \dot{\psi}_{\mathrm{frame}}^2 \tag{9}$$

$$T_{\mathrm{RC}} = \frac{1}{2} m_{\mathrm{RC}} \bar{v}_{\mathrm{G,RC}} \cdot \bar{v}_{\mathrm{G,RC}} + \frac{1}{2} \left(I_{yy}\right)_{\mathrm{RC}} \dot{\phi}_{\mathrm{RC}}^2 + \frac{1}{2} \left(I_{zz}\right)_{\mathrm{RC}} \dot{\psi}_{\mathrm{frame}}^2 \tag{10}$$

where $\dot{\phi}$ is the spin rate of a particular wheel with respect to the frame. Summing (6)-(10), the total kinetic energy of the wheelchair can be estimated by

$$\begin{aligned} T_{\mathrm{sys}} = {} & \frac{1}{2} m_{\mathrm{frame}} \bar{v}_{\mathrm{G,frame}} \cdot \bar{v}_{\mathrm{G,frame}} + \frac{1}{2} \left(I_{zz}\right)_{\mathrm{frame}} \dot{\psi}_{\mathrm{frame}}^2 \\ & + \frac{1}{2} m_{\mathrm{LD}} \bar{v}_{\mathrm{G,LD}} \cdot \bar{v}_{\mathrm{G,LD}} + \frac{1}{2} \left(I_{yy}\right)_{\mathrm{LD}} \dot{\phi}_{\mathrm{LD}}^2 + \frac{1}{2} \left(I_{zz}\right)_{\mathrm{LD}} \dot{\psi}_{\mathrm{frame}}^2 \\ & + \frac{1}{2} m_{\mathrm{RD}} \bar{v}_{\mathrm{G,RD}} \cdot \bar{v}_{\mathrm{G,RD}} + \frac{1}{2} \left(I_{yy}\right)_{\mathrm{RD}} \dot{\phi}_{\mathrm{RD}}^2 + \frac{1}{2} \left(I_{zz}\right)_{\mathrm{RD}} \dot{\psi}_{\mathrm{frame}}^2 \\ & + \frac{1}{2} m_{\mathrm{LC}} \bar{v}_{\mathrm{G,LC}} \cdot \bar{v}_{\mathrm{G,LC}} + \frac{1}{2} \left(I_{yy}\right)_{\mathrm{LC}} \dot{\phi}_{\mathrm{LC}}^2 + \frac{1}{2} \left(I_{zz}\right)_{\mathrm{LC}} \dot{\psi}_{\mathrm{frame}}^2 \\ & + \frac{1}{2} m_{\mathrm{RC}} \bar{v}_{\mathrm{G,RC}} \cdot \bar{v}_{\mathrm{G,RC}} + \frac{1}{2} \left(I_{yy}\right)_{\mathrm{RC}} \dot{\phi}_{\mathrm{RC}}^2 + \frac{1}{2} \left(I_{zz}\right)_{\mathrm{RC}} \dot{\psi}_{\mathrm{frame}}^2 \end{aligned} \tag{11}$$

Equation (11) is furthered simplified by several observations. First, in the case of straight propulsion, the translational kinetic energy terms can be written as

$$T_{\mathrm{sys,trans}} = \frac{1}{2} m \bar{v}_{\mathrm{G}} \cdot \bar{v}_{\mathrm{G}} \tag{12}$$

where

$$m = m_{\mathrm{frame}} + m_{\mathrm{LD}} + m_{\mathrm{RD}} + m_{\mathrm{LC}} + m_{\mathrm{RC}} \tag{13}$$

and $\bar{v}_{\mathrm{G}}$ is the velocity of the center of mass of the *system*. This simplification is not valid in general during turning because the caster movement means that the inertia properties change slightly with time. Figure 4 illustrates the velocity of each of the components during turning maneuvers.

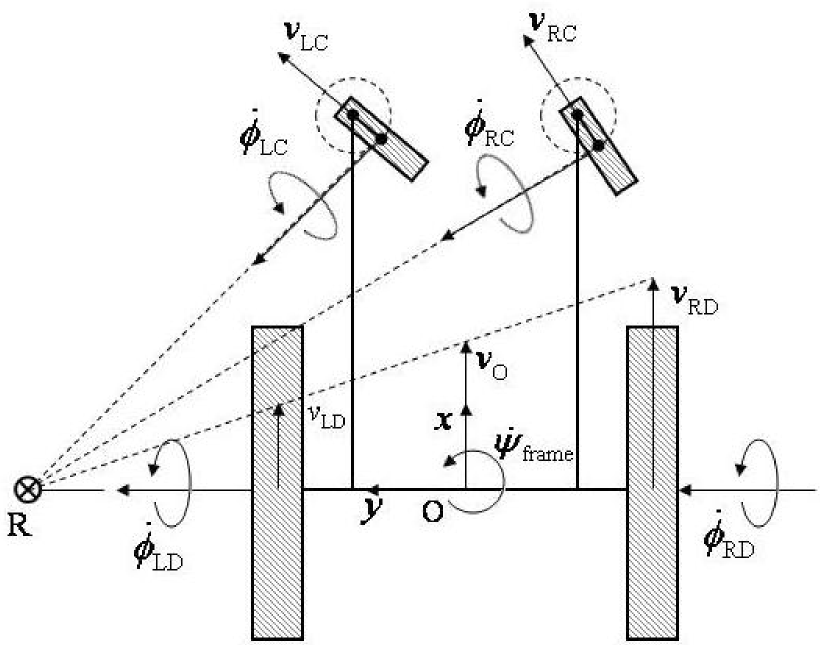

Figure 4. Velocity of wheelchair components during turning

Neglecting the swivel of the casters, the velocity of the CG of each component *i* can be compared to the velocity of the CG of the system as follows,

$$\bar{v}_{\mathrm{G},i} = \bar{v}_{\mathrm{G}} + \dot{\psi}_{\mathrm{frame}} \bar{k} \times \bar{r}_{i/\mathrm{G}} \tag{14}$$

where $\bar{r}_{i/\mathrm{G}}$ is the position vector pointing from the CG of the system to the CG of the component. Taking the dot product yields

$$\bar{v}_{\mathrm{G},i} \cdot \bar{v}_{\mathrm{G},i} = \bar{v}_{\mathrm{G}} \cdot \bar{v}_{\mathrm{G}} + 2\bar{v}_{\mathrm{G}} \cdot \left(\dot{\psi}_{\mathrm{frame}} \bar{k} \times \bar{r}_{i/\mathrm{G}}\right) + \left(\dot{\psi}_{\mathrm{frame}} \bar{k} \times \bar{r}_{i/\mathrm{G}}\right) \cdot \left(\dot{\psi}_{\mathrm{frame}} \bar{k} \times \bar{r}_{i/\mathrm{G}}\right) \tag{15}$$

For each component, the third dot product in the preceding equation can be written as

$$\left(\dot{\psi}_{\text{frame}}\bar{k}\times\bar{r}_{i/\text{G}}\right)\cdot\left(\dot{\psi}_{\text{frame}}\bar{k}\times\bar{r}_{i/\text{G}}\right)=\dot{\psi}_{\text{frame}}^{2}d_{i}^{2} \tag{16}$$

where d_i is the distance from the CG of the component denoted by i to the CG of the system. Since the definition of the system center of mass implies that $\sum_i m_i\,\bar{r}_{i/\text{G}}=\bar{0}$, the middle dot products in (15) will sum to zero when substituted into (11).

With this in mind, the velocity dot products can be substituted back into the kinetic energy given in (11) to form the new expression,

$$\begin{aligned}
T_{\text{sys}} &= \frac{1}{2}m_{\text{frame}}\left(\bar{v}_{\text{G}}\cdot\bar{v}_{\text{G}}+\dot{\psi}_{\text{frame}}^{2}d_{\text{frame}}^{2}\right)+\frac{1}{2}\left(I_{zz}\right)_{\text{frame}}\dot{\psi}_{\text{frame}}^{2}\\
&+\frac{1}{2}m_{\text{LD}}\left(\bar{v}_{\text{G}}\cdot\bar{v}_{\text{G}}+\dot{\psi}_{\text{frame}}^{2}d_{\text{LD}}^{2}\right)+\frac{1}{2}\left(I_{yy}\right)_{\text{LD}}\dot{\phi}_{\text{LD}}^{2}+\frac{1}{2}\left(I_{zz}\right)_{\text{LD}}\dot{\psi}_{\text{frame}}^{2}\\
&+\frac{1}{2}m_{\text{RD}}\left(\bar{v}_{\text{G}}\cdot\bar{v}_{\text{G}}+\dot{\psi}_{\text{frame}}^{2}d_{\text{RD}}^{2}\right)+\frac{1}{2}\left(I_{yy}\right)_{\text{RD}}\dot{\phi}_{\text{RD}}^{2}+\frac{1}{2}\left(I_{zz}\right)_{\text{RD}}\dot{\psi}_{\text{frame}}^{2}\\
&+\frac{1}{2}m_{\text{LC}}\left(\bar{v}_{\text{G}}\cdot\bar{v}_{\text{G}}+\dot{\psi}_{\text{frame}}^{2}d_{\text{LC}}^{2}\right)+\frac{1}{2}\left(I_{yy}\right)_{\text{LC}}\dot{\phi}_{\text{LC}}^{2}+\frac{1}{2}\left(I_{zz}\right)_{\text{LC}}\dot{\psi}_{\text{frame}}^{2}\\
&+\frac{1}{2}m_{\text{RC}}\left(\bar{v}_{\text{G}}\cdot\bar{v}_{\text{G}}+\dot{\psi}_{\text{frame}}^{2}d_{\text{RC}}^{2}\right)+\frac{1}{2}\left(I_{yy}\right)_{\text{RC}}\dot{\phi}_{\text{RC}}^{2}+\frac{1}{2}\left(I_{zz}\right)_{\text{RC}}\dot{\psi}_{\text{frame}}^{2}
\end{aligned} \tag{17}$$

Simplifying the equation yields

$$\begin{aligned}
T_{\text{sys}} &= \frac{1}{2}m_{\text{frame}}\left(\bar{v}_{\text{G}}\cdot\bar{v}_{\text{G}}\right)+\frac{1}{2}\left(I_{yy}\right)_{\text{LD}}\dot{\phi}_{\text{LD}}^{2}+\frac{1}{2}\left(I_{yy}\right)_{\text{RD}}\dot{\phi}_{\text{RD}}^{2}+\frac{1}{2}\left(I_{yy}\right)_{\text{LC}}\dot{\phi}_{\text{LC}}^{2}+\frac{1}{2}\left(I_{yy}\right)_{\text{RC}}\dot{\phi}_{\text{RC}}^{2}\\
&+\frac{1}{2}\left[\left(I_{zz}\right)_{\text{frame}}+m_{\text{frame}}d_{\text{frame}}^{2}\right]\dot{\psi}_{\text{frame}}^{2}+\frac{1}{2}\left[\left(I_{zz}\right)_{\text{LD}}+m_{\text{LD}}d_{\text{LD}}^{2}\right]\dot{\psi}_{\text{frame}}^{2}\\
&+\frac{1}{2}\left[\left(I_{zz}\right)_{\text{RD}}+m_{\text{RD}}d_{\text{RD}}^{2}\right]\dot{\psi}_{\text{frame}}^{2}+\frac{1}{2}\left[\left(I_{zz}\right)_{\text{LC}}+m_{\text{LC}}d_{\text{LC}}^{2}\right]\dot{\psi}_{\text{frame}}^{2}\\
&+\frac{1}{2}\left[\left(I_{zz}\right)_{\text{RC}}+m_{\text{RC}}d_{\text{RC}}^{2}\right]\dot{\psi}_{\text{frame}}^{2}
\end{aligned} \tag{18}$$

At this point, it is beneficial to describe the Parallel Axis Theorem, which states that the moment of inertia of an object about an axis, say A, passing through an arbitrary point P is related to the moment of inertia of the object about a parallel axis B and passing through the object's center of gravity by the mass multiplied by the square of the distance d between the two axes. Mathematically, this can be written as

$$I_A^{\mathrm{P}} = I_B^{\mathrm{G}} + md^2 \tag{19}$$

With this in mind, the rotational kinetic energy terms in (18) due to the yaw rotation $\dot{\psi}_{\mathrm{frame}}$ can be written in terms of the moment of inertia of the system about the z-axis passing through its CG,

$$\frac{1}{2}\left(I_{\mathrm{zz}}^{\mathrm{G}}\right)_{\mathrm{sys}} \dot{\psi}_{\mathrm{frame}}^{2} \tag{20}$$

where the total system inertia is equal to the sum of the inertia of the components,

$$\left(I_{\mathrm{zz}}^{\mathrm{G}}\right)_{\mathrm{sys}} = \left(I_{\mathrm{zz}}^{\mathrm{G}}\right)_{\mathrm{frame}} + \left(I_{\mathrm{zz}}^{\mathrm{G}}\right)_{\mathrm{LD}} + \left(I_{\mathrm{zz}}^{\mathrm{G}}\right)_{\mathrm{RD}} + \left(I_{\mathrm{zz}}^{\mathrm{G}}\right)_{\mathrm{LC}} + \left(I_{\mathrm{zz}}^{\mathrm{G}}\right)_{\mathrm{RC}} \tag{21}$$

In summary, for straight motion that does not involve wheelchair pitch, the total kinetic energy of the system is given by

$$T_{\mathrm{sys}} = \frac{1}{2} m \bar{v}_{\mathrm{G}} \cdot \bar{v}_{\mathrm{G}} + \frac{1}{2}\left(I_{yy}\right)_{\mathrm{LD}} \dot{\phi}_{\mathrm{LD}}{}^{2} + \frac{1}{2}\left(I_{yy}\right)_{\mathrm{RD}} \dot{\phi}_{\mathrm{RD}}{}^{2} + \frac{1}{2}\left(I_{yy}\right)_{\mathrm{LC}} \dot{\phi}_{\mathrm{LC}}{}^{2} + \frac{1}{2}\left(I_{yy}\right)_{\mathrm{RC}} \dot{\phi}_{\mathrm{RC}}{}^{2} \tag{22}$$

and for turning maneuvers with no wheelchair pitch, the kinetic energy is

$$\begin{aligned} T_{\mathrm{sys}} = {} & \frac{1}{2} m \bar{v}_{\mathrm{G}} \cdot \bar{v}_{\mathrm{G}} + \frac{1}{2}\left(I_{yy}\right)_{\mathrm{LD}} \dot{\phi}_{\mathrm{LD}}{}^{2} + \frac{1}{2}\left(I_{yy}\right)_{\mathrm{RD}} \dot{\phi}_{\mathrm{RD}}{}^{2} + \frac{1}{2}\left(I_{yy}\right)_{\mathrm{LC}} \dot{\phi}_{\mathrm{LC}}{}^{2} + \frac{1}{2}\left(I_{yy}\right)_{\mathrm{RC}} \dot{\phi}_{\mathrm{RC}}{}^{2} \\ & + \frac{1}{2}\left(I_{\mathrm{zz}}^{\mathrm{G}}\right)_{\mathrm{sys}} \dot{\psi}_{\mathrm{frame}}^{2} \end{aligned} \tag{23}$$

Clearly, one of the necessary parameters to estimate in order to obtain an accurate measure of the stored kinetic energy during wheelchair propulsion is the moment of inertia of the system about the vertical (yaw) axis, $\left(I_{\mathrm{zz}}^{\mathrm{G}}\right)_{\mathrm{sys}}$. Therein is the motivation for the design of the iMachine.

1.3 Measuring Inertial Properties

Many experimental techniques have been developed to measure the inertial properties of irregularly shaped rigid bodies, leading to several patented devices [1-3]. As mentioned earlier, one simple way of finding the moments of inertia is through the numerical integration tools available in some 3D modeling software [4], but this method requires a precise model, which may not be available, particularly if the object is too complex or designed by someone other than the researcher. More recently, Almeida, *et al.* [5] outlined a handful of modern approaches to inertia parameter identification, including Modal Methods (MM), which derives the inertia tensor of an object by attempting to excite it at its rigid body modes. Despite these new computationally complex attempts to increase the precision with which rigid body mass properties can be measured, conventional methods using simple free vibration principles are well established and offer a sufficient amount of accuracy for most experimental applications. Among these traditional approaches are pendulum devices and rotating platforms, which will be described in the subsequent sections.

1.3.1 Gravitational Pendulum Method

Perhaps the most basic system for estimating inertia properties is the simple gravitational pendulum, depicted in Figure 5.

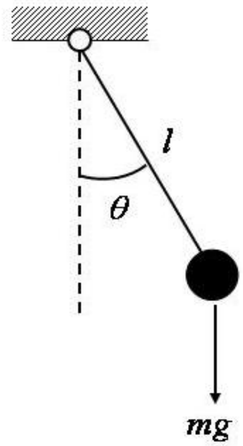

Figure 5. Gravitational pendulum model

Ogata [6] derives the equation of motion by summing the moments about the fixed pivot point,

$$I\ddot{\theta} = -mgl\sin\theta \tag{24}$$

By using a small angle approximation ($\sin\theta \approx \theta$), the general equation takes the form of a single-degree-of-freedom (SDOF) system undergoing simple harmonic motion,

$$\ddot{\theta} + \omega_n^2\theta = 0 \tag{25}$$

where ω_n is the natural frequency in radians per second. If ω_n is measured, the moment of inertia, I, can be determined by its direct relationship to geometric parameters and the natural frequency, ω_n, by

$$I = \frac{mgl}{\omega_n^2} \tag{26}$$

There are several challenges with this method from a practical standpoint including assessing the bounds for which the small angle approximation is valid. In addition, this model assumes that the string to which the object being measured is attached has negligible mass, which is impractical for most cases. If the mass is known, the equation of motion in (24) becomes more complicated because the weight of the string must be taken into account. If the attachment means is an issue, one possible solution is the bifilar pendulum shown in Figure 6.

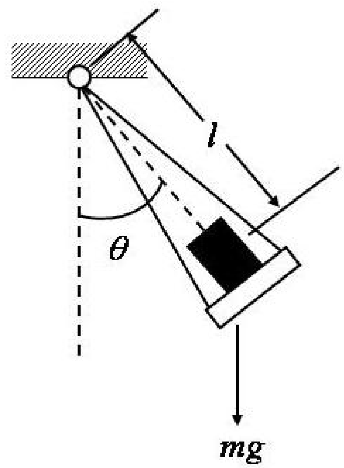

Figure 6. Bifilar gravitational pendulum model

The major challenge with this method, aside from adding complexity to the test procedure, is that the distance from the pivot point to the center of mass of the system is no longer known. Depending on the sensing capabilities of the device, this important parameter may be difficult or impossible to measure.

1.3.2 Torsional Pendulum Method

The torsional pendulum method [7-9] is arguably the most popular inertial parameter estimation technique. This approach uses the same basic Newton-Euler approach as the simple pendulum, but the vibration occurs due to rotation in the horizontal plane rather than the vertical plane. The model for a trifilar pendulum is shown in Figure 7, although bifilar versions have been researched as well.

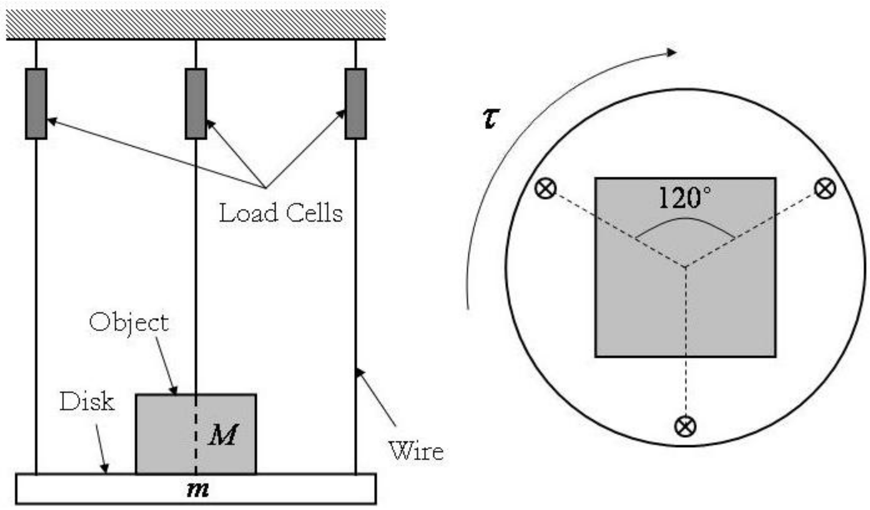

Figure 7. Trifilar torsional pendulum model

The device consists of a stationary upper plate attached to a lower plate via a series of cables. When the lower plate is displaced from equilibrium in the angular direction, the pendulum cables (or files) generate a restoring torque to induce simple harmonic motion. Du Bois, *et al.* [7] suggests that the multifilar pendulum is considered to be the most accurate method, with errors less than 1%. Ogata [6] derived the equation of motion using the assumption that the cables were of equal length and equidistant from the center of the lower plate. Additionally, it was assumed in his analysis that the object to be measured was centered on the plate so that the forces and angle of rotation in each cable was equal. The resulting equation is

$$I = \frac{Mga^2T^2}{4\pi^2 h} \tag{27}$$

where M is the total mass of the system, g is the acceleration due to gravity, a is the radial distance from the cable to the center of the lower plate, T is the natural period of oscillation, and h is the height of each cable.

The most difficult and time consuming part of this method is centering the CG of the object with the axis of rotation. If the axis passing through the CG is not coincident with the rotation axis, several errors could propagate in the results. First, the theory used to derive (27) becomes more complicated because the forces in the cable are not equal, and their rotation angles may differ as well. Second, the weight imbalance may cause the lower plate to tilt, which would result in an inertia measurement about an axis at an angle to the desired vertical axis. In fact, Ringegni, *et al.* [8] demonstrates through experimental measurements that improper centering of the body actually results in an additional longitudinal oscillation due to the CG eccentricity. If nothing else, making constant configuration adjustments will most likely cause the pendulum to swing, which in turn may become a frustrating process for the researcher. Nevertheless, Zhi-Chao, *et al*. [9] seems to have found an efficient solution by strategically adding known weights to balance the plate rather than attempting to move the potentially heavy and cumbersome object. His method resulted in errors less than 1% in general.

1.3.3 Rotating Platform Method

Griffiths, *et al.* [10] designed a rotating platform apparatus to measure the moment of inertia of the human body. The mechanical system design is displayed in Figure 8.

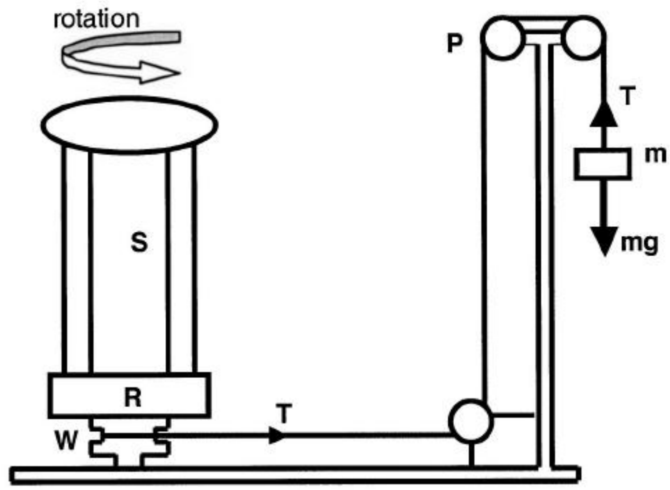

Figure 8. Rotating platform model with falling mass [10]

The system operates by transmitting a torque due to a falling known mass to the turntable via a series of low-friction pulleys. Unlike the previously described methods, Griffith's apparatus does not use simple harmonic motion principles. Instead, a high-resolution motion capture system tracks two retro-reflective markers on the turntable as it rotates. The relation between the inertia and the measured properties is given by the moment equation about the rotation axis of the platform,

$$I = \frac{rTt}{\omega_{\text{final}}} = \frac{rt(mg - ma)}{\omega_{\text{final}}} = \frac{rtm\left(g - \frac{2s}{t^2}\right)}{\omega_{\text{final}}} \tag{28}$$

where ω_{final} is the final angular velocity at time t, r is the pulley radius, m is the known mass that generated the input torque, g is the acceleration due to gravity, and s is the distance that the mass fell.

While there are several difficulties inherent in testing human subjects when they need to be perfectly rigid, the researchers recognized the difficulty in centering the mass on the platform. Additionally, friction had a significant effect on the accuracy of results because it produces a moment not accounted for in (28) that opposes the input torque.

Another way of implementing the rotating platform method is shown in Figure 9. This approach combines the small workspace of the aforementioned apparatus while maintaining the oscillatory nature of the torsional pendulum devices.

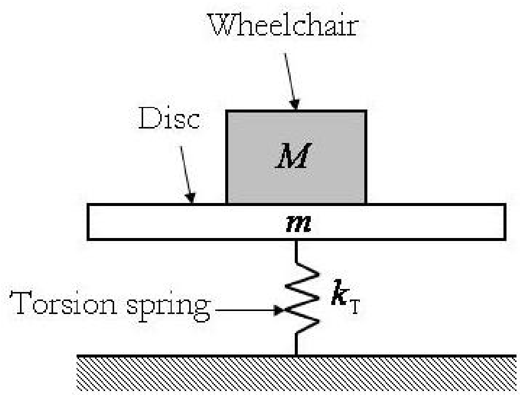

Figure 9. Rotating platform model with torsion spring

The general equation of motion can be expressed in the form of (25) with

$$\omega_n = \sqrt{\frac{k_T}{I}} \tag{29}$$

It is easy to see how the inertia is calculated in a simple, effective manner. This design could handle eccentric loads better if the platform were mounted properly on a sturdy shaft. The challenges for this device are determining efficient measurement techniques for recording the mass, center of mass, and angular position of the platform.

1.3.4 Previous Wheelchair Inertia Research

There has been little research done on implementing inertia parameter identification techniques for manual wheelchairs specifically. Kauzlarich, *et al.* [11] used the torsional pendulum method to determine the inertia of the manual wheelchair with the drive wheels removed, but offered no discussion on the accuracy of results. Ding [12] estimated the moment of inertia by rotating an occupied power wheelchair on a force plate and tracking the angular velocity of the chair using a motion capture system. The desired inertia was derived from Euler moment equations. Wang, *et al.* [13] also studied the inertia of power wheelchairs, but used the more conventional torsional pendulum approach with four cables. The device was calibrated using two objects with known analytical inertia: a metal disk and a cylinder. However, the error for the inertia measurement of the two objects was 9.1042% and 10.3279%, respectively. Wang commented on the error introduced when the object's CG is not coincident with the rotation axis and on the harmful effects that swinging of the pendulum has on accuracy. His methods could be greatly improved by better precision measurement devices, as a simple stopwatch was used to measured the period.

1.4 Summary

The goal of this project is to design a robust, high precision measurement device for determining four inertial properties of manual wheelchairs: the total system mass, coordinates of the center of mass, and inertia about the vertical axis passing through the CG. The design selection will be described in Chapter 2, including theory and component specification. In Chapter 3, a detailed computational approach is presented for calculating the desired inertial parameters using the iMachine. Chapter 4 discusses the test methods for calibrating the load cells and springs. In Chapter 5, validation tests and results are given for each of the inertial parameters, as well as wheelchair inertia results based on iMachine tests. Chapter 6 offers some conclusions based on the test results and provides recommendations for improving the iMachine in the future.

CHAPTER 2

DESIGN

2.1 Design Selection

The final design selection for the iMachine draws from multiple approaches presented in the previous chapter and is illustrated schematically in Figure 10 below. It is a spring-loaded disk that is free to oscillate in the horizontal plane about an axis perpendicular to the *xy*-plane and passing through point O.

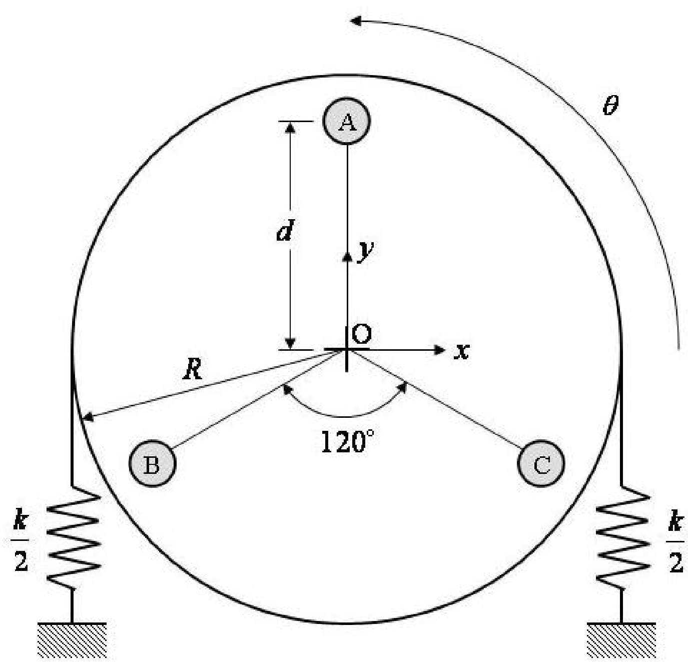

Figure 10. Model of iMachine design

The disk is center-mounted on a stepped shaft (not pictured) that is equipped with an optical encoder for monitoring the angular position of the disk. A fixed collar holds two bearings that support the radial and axial loads on the shaft, reduce the frictional effects on rotation, and restrict the tilt of the platform. Load cells located at points A, B, and C measure the forces due to the weight of the object being tested. The interface between the disk and the test object is a x-y positioning platform (not pictured).

2.2 Theory

The general equation of motion for a SDOF mechanical system undergoing free vibration is given by

$$m\ddot{q} + c\dot{q} + kq = 0 \tag{30}$$

where $q, \dot{q}, \text{and } \ddot{q}$ are the generalized coordinate and its first two derivatives, *m* is the mass of the system, *c* is the damping coefficient, and *k* is the spring constant. The system is subjected to the following initial conditions

$$\begin{aligned} q(0) &= q_0 \\ \dot{q}(0) &= v_0 \end{aligned} \tag{31}$$

In the system under consideration, the generalized coordinate is the angular position of the oscillating disk. Therein, summing the moments about the center of the disk yields the following equation of motion,

$$I\ddot{\theta} + c\dot{\theta} + kR^2\theta = 0 \tag{32}$$

where *I* is the moment of inertia about the axis of rotation, which is the desired parameter to be measured. The device uses two linear springs in parallel, each with spring constant $k/2$, making the total equivalent spring constant *k*. In addition, the distance from the point of application of each spring to the center of the disk, *R* (not necessarily equal to the radius of the disk), must be considered because it is the moment-arm for each spring force.

If we consider (32) to be of the form

$$\ddot{\theta} + 2\zeta\omega_{\mathrm{n}}\dot{\theta} + \omega_{\mathrm{n}}^2\theta = 0 \tag{33}$$

then the moment of inertia can be calculated using the following equation

$$I = \frac{kR^2T_{\mathrm{n}}^2}{4\pi^2} \tag{34}$$

where T_{n} is the natural period of oscillation, derived from the damped period, T_{d}, by noting that

$$T_{\mathrm{n}} = T_{\mathrm{d}}\sqrt{1-\zeta^2} \tag{35}$$

where ζ is the damping ratio. The next section outlines the specifications for each of the system components based on assumptions and the theoretical analysis presented here.

2.3 Component Specification

2.3.1 Structural Frame

The purpose of the structural frame is to provide stability and support for the rest of the device. It needs to have a wide base so that the CG of the system on top is always located within the perimeter of the frame. Other design specifications include low cost, simple to machine, and ease of assembly. As a result, the frame was made using extruded aluminum beams (80/20 Inc., Columbia City, IN) with corner brackets to increase the structural rigidity. The outer dimensions of the frame are 0.762x0.762 m (30x30 in).

2.3.2 Disk

The only major requirements for the disk is that it be large enough in diameter for proper load cell positioning and strong enough to withstand the stresses due to the maximum allowable load. To meet the first requirement, the disk was cut to approximately 24 inches in diameter (measured to be 0.29845 m). This size should be sufficient because it is larger than the wheel width (distance from contact points on the ground) of nearly all of the wheelchairs to be tested. The load cell configuration can be designed to fit within these bounds. Ideally, the disk material should be made of a single material, most likely a strong metal, to keep its material properties homogeneous. However, a large metal disk with moderate thickness can be quite costly. As a result, the disk was made with multiple layers: a core ½" thick wood layer with a thin steel layer laminated to either side using a strong adhesive. The multi-layered disk was machined using a water jet. There is a tradeoff between cost and error, though, as the disk appeared to show slight warping several days after it had been machined. However, given that the angular displacement of the disk is assumed to be small during testing, the warping should have a negligible effect on the dynamics of the system. Figure 11 illustrates the final machined disk design.

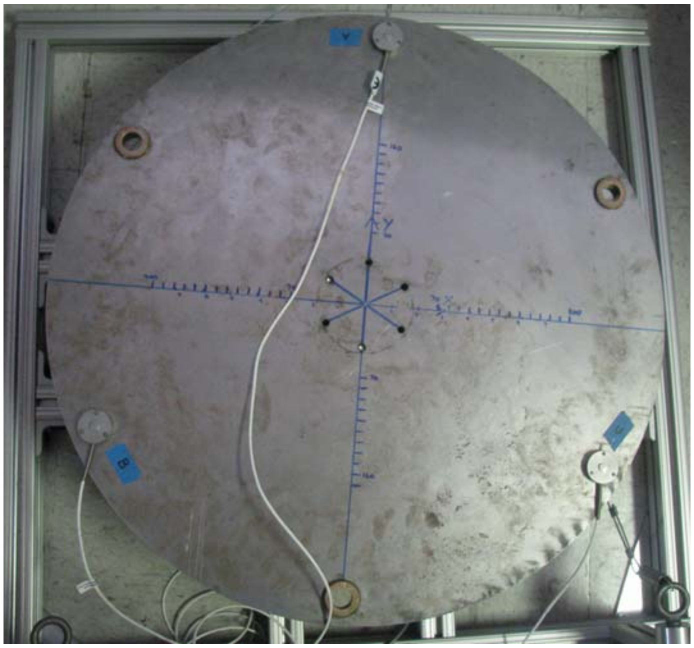

Figure 11. iMachine disk

2.3.3 Shaft Assembly

The shaft assembly is pictured in Figure 12, and it consists of a stepped aluminum shaft, steel shaft collar, aluminum bearing collar, and two steel ball bearings.

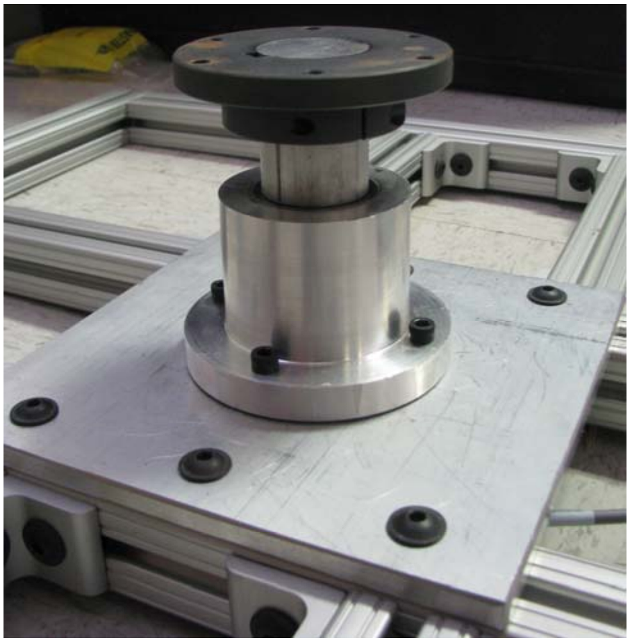

Figure 12. iMachine shaft assembly

A bending stress analysis was performed to select an acceptable shaft diameter. The normal yield stress of Al 6061-T6 is found to be 270 MPa (40 ksi) [14]. Given a safety factor, *n*, the maximum allowable normal stress, σ_{allow}, can be calculated using the relation

$$n = \frac{\sigma_y}{\sigma_{\text{allow}}} \tag{36}$$

so that, for example, a safety factor of 3 dictates a maximum allowable normal stress equal to 90 MPa (13.3 ksi). The load on the platform is bounded above by the weight of an occupied wheelchair, which was reasonably assumed not to exceed 136.071 kg (300 lbs) for this test application. In the rare case that the maximum load is applied at the edge of the disk, the maximum moment generated about the shaft would be equal to 398.4 N-m. Using the equation

$$S = \frac{M_{\max}}{\sigma_{\text{allow}}} \tag{37}$$

the required section modulus, *S,* is determined to be 4427 mm^3. For circular cross sections of diameter *d*, the section modulus is defined as

$$S = \frac{\pi d^3}{32} \tag{38}$$

Therefore, by rearranging (38), the minimum shaft diameter for the given conditions is equal to 35.6 mm (1.40 in).

This analysis assumes a constant diameter shaft, but practically the shaft must be stepped to accommodate the smaller diameter requirements of the bearings and encoder. To ensure an acceptable safety factor for bending stress, the largest diameter of the shaft was set to 38.1 mm (1.5 in). Working backwards through equations (36)-(38), the safety factor can be approximated to equal 3.68, which is more than sufficient for the design.

For completeness, the deflection of the end of the shaft is calculated based on the design parameters listed above. The purpose of this exercise is to ensure that bending is negligible because any significant deflection affects the axis about which the moment of inertia is measured. Suppose the shaft is modeled as shown in Figure 13, where the entire assembly has been rotated 90° to resemble a beam in bending. Note that this “virtual” rotation has no effect on the validity of the analysis. The reactions forces at point A represent that of a thrust bearing, which can take both axial and radial load. The reaction force at point B refers to a simple ball bearing. The force on top of the shaft, F (pictured to the side in Figure 13), produces a moment due to its eccentricity, ε.

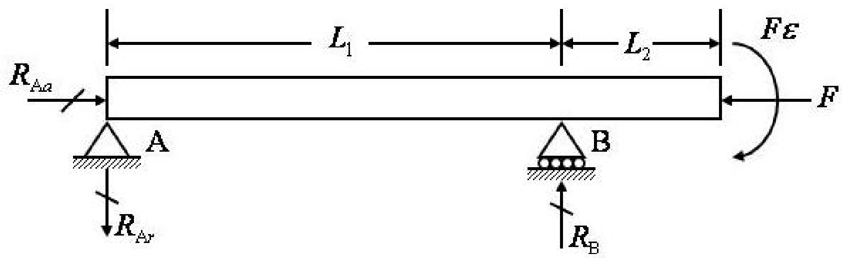

Figure 13. Modeling the shaft assembly as a beam in bending

Taking the sum of the forces in both the radial and axial directions as well as the sum of the moments about point A, the reactions forces can be solved for as follows,

$$\sum F_r = 0 : R_{Ar} = R_B \tag{39}$$

$$\sum F_a = 0 : R_{Aa} = F \tag{40}$$

$$\sum M_A = 0 : R_B L_1 - F\varepsilon = 0 \tag{41}$$

This implies that the reactions forces, and thus the load bearing capacity of each bearing, are given by

$$\begin{aligned} R_B &= F\frac{\varepsilon}{L_1} \\ R_{Ar} &= F\frac{\varepsilon}{L_1} \\ R_{Aa} &= F \end{aligned} \tag{42}$$

Using (42), the shear forces along the shaft can be computed as

$$V = \begin{cases} -F\dfrac{\varepsilon}{L_1}, & (0 < a < L_1) \\ 0, & (L_1 < a < L_1 + L_2) \end{cases} \tag{43}$$

and the bending moments along the shaft are given by

$$M = EIv'' = \begin{cases} -F\dfrac{\varepsilon a}{L_1}, & (0 < a < L_1) \\ -F\varepsilon, & (L_1 < a < L_1 + L_2) \end{cases} \tag{44}$$

where E is the modulus of elasticity, I is the moment of inertia of the shaft, and v'' is the second derivative of the deflection. Integrating (44) gives an equation for the slope along the beam,

$$EIv' = \begin{cases} -F\dfrac{\varepsilon a^2}{2L_1} + C_1, & (0 < a < L_1) \\ -F\varepsilon a + C_2, & (L_1 < a < L_1 + L_2) \end{cases} \tag{45}$$

Since the slope at point B must be continuous, $v'(L_1)$ must be equal for the two equations above. Plugging this in,

$$-F\frac{\varepsilon L_1^2}{2L_1} + C_1 = -F\varepsilon L_1 + C_2 \tag{46}$$

and solving for C_2 in terms of C_1,

$$C_2 = C_1 + F\frac{\varepsilon L_1}{2} \tag{47}$$

Integrate (45) once more to obtain the deflection equations,

$$EIv = \begin{cases} -F\dfrac{\varepsilon a^3}{6L_1} + C_1 a + C_3, & (0 < \mathrm{a} < L_1) \\ -\dfrac{F\varepsilon a^2}{2} + C_2 a + C_3, & (L_1 < \mathrm{a} < L_1 + L_2) \end{cases} \tag{48}$$

The boundary conditions for the first equation are that the deflection equals zero at the bearing locations – that is, $v(0) = v(L_1) = 0$. Applying these conditions to the first equation in (48) gives the following result,

$$v(0) = \frac{1}{EI} C_3 = 0 \quad \Rightarrow \quad C_3 = 0 \tag{49}$$

$$v(L_1) = \frac{1}{EI}\left(-F \frac{\varepsilon L_1^2}{6} + C_1 L_1 \right) = 0 \quad \Rightarrow \quad C_1 = F \frac{\varepsilon L_1}{6} \tag{50}$$

Inserting the value for C_1 found in (50) into (47), C_2 is shown to equal

$$C_2 = F \frac{2\varepsilon L_1}{3} \tag{51}$$

Applying the second boundary condition to the second equation in (48) gives

$$v(L_1) = \frac{1}{EI}\left(-\frac{F\varepsilon L_1^2}{2} + F \frac{2\varepsilon L_1^2}{3} + C_3 \right) = 0 \quad \Rightarrow \quad C_3 = -F \frac{\varepsilon L_1^2}{6} \tag{52}$$

Combining the coefficients from (50) and (52) and plugging into (48), the deflection at the end of the shaft can be written as

$$\delta(L_1 + L_2) = -v(L_1 + L_2) = \frac{F\varepsilon}{6EI}\left[3(L_1 + L_2)^2 - 4L_1(L_1 + L_2) + L_1^2 \right] \tag{53}$$

The elastic modulus of Al 6061-T6 is 70 GPa (10000 ksi), the load and eccentricity are defined as before to cause the maximum moment, and the inertia of the shaft with a constant 38.1 mm (1.5 in) diameter is $1.0344x10^{-7}\,\mathrm{m}^4$. The locations of the bearings were varied iteratively to find a suitable set of parameters that minimized deflection and kept the iMachine height relatively low. The final design is a total shaft length of 70 mm with 30 mm between the two bearings. This produces a deflection of only 0.0458 mm when the maximum moment is applied. In more realistic scenarios – say, with a 15 kg mass (unoccupied wheelchair) applied at no greater than 127 mm (5 in) eccentricity – the deflection of the end of the shaft is 0.0022 mm. Clearly, these shaft parameters will be sufficient in meeting the design specifications, particularly with the addition of the 3 in-diameter steel shaft collar.

Steel ball bearings (McMaster-Carr Inc., Santa Fe Springs, CA) were selected that meet the load capacities outlined in (42). The top bearing (B in Figure 13) has a radial load capacity of 7.2 kN (1,628 lbs), which, according to (42), can withstand a 136.071 kg (300 lbs) load at an eccentricity of up to almost 16.51 cm (6.5 in). The bottom bearing (A in Figure 13) is a dual load angular contact bearing and has a radial load capacity of 13.3 kN (2,990 lbs), which is enough to support even the maximum moment specified above.

2.3.4 Springs

The most important design specifications are those that directly influence the calculation of the moment of inertia, given by Equation (34). While the damping ratio in (35) can be somewhat controlled by modifying the friction in the shaft bearings, it is assumed that the system is underdamped and the effects of a small change in damping are negligible. Instead, the primary controllable design parameter is the springs. Figure 10 showed that a pair of linear springs were chosen rather than a single torsion spring. The primary reason is that linear springs mounted away from the shaft increase accessibility, making it easier to mount and replace them, which may be important for testing objects with widely varying inertia. This section addresses the frequency and geometric constraints of the system with the goal of selecting springs that achieve a practical and reliable design.

2.3.4.1 Frequency Constraints

In analyzing this problem, it is important to consider the effects of frequency on the reliability of the measurements. For example, a natural frequency that is too high may cause unnecessary vibration of the wheelchair if the connection to the rotating platform is not perfectly rigid. In this case, the center of mass of the system would be constantly moving, which in turn affects the rotation of the disk and the ensuing inertia calculations. In addition, a high natural frequency and poor interface between the object and the disk may cause the object to rotate according to a second DOF that lags the angular position of the disk. This compromises the accuracy of the SDOF model and may introduce significant errors in the measurement. On the other hand, a natural frequency that is too low may require an excessive amount of time to record enough data for computing the inertia. Initially, it will be assumed that a natural frequency less than 1 Hz will be sufficient to neglect internal relative motion of the system components. This corresponds to a natural period that is greater than 1 second.

For the purpose of spring selection, it is necessary to estimate the inertia range that will be tested with the device. To that end, a simple prototype of the system design was constructed using a spring-loaded wooden platform mounted to a lazy susan bearing. The platform was loaded with a person sitting in a wheelchair. Upon giving the system an initial angular velocity, the period of oscillation was measured using a stopwatch. The spring constant ($k/2$) is 1814 N/m (10.36 lb/in) and the distance R is approximately 11.43 cm (4.5 in). The average damped period for a 63.5 kg (140 lb) subject occupying a wheelchair was 2.32 s, which results in a moment of inertia of 6.46 kg-m^2 (22,100 lb-in^2), assuming approximately 10% damping. The average damped period for a 86.2 kg (190 lb) subject occupying a wheelchair was 2.66 s, resulting in a moment of inertia of 8.48 kg-m^2 (29,000 lb-in^2). Even though it is not a good idea in practice, the data was extrapolated to estimate the inertia of an unoccupied wheelchair. This is acceptable for this situation because only a rough estimate of the inertia is needed. Taking into account that the mass of the platform of the final system is approximately 22.7 kg (50 lbs) heavier than the wooden prototype, the total moment of inertia of an unoccupied wheelchair on the new system is estimated to be around 2.93 kg-m^2 (10,000 lb-in^2), which forms the lower bound of the desired inertia range. The upper bound is found by assuming a 102.1 kg (225 lb) AMPS occupying the wheelchair, which results in an estimated moment of inertia of 11.94 kg-m^2 (40,800 lb-in^2). Based on these results, springs should be selected to meet the frequency specifications for an inertia range of approximately 3-12 kg-m^2.

To accomplish this, Table 1 and Table 2 show the possible combinations of T_n and R values and the corresponding half-spring constant ($k/2$) for an inertia value of 10,000 lb-in^2 and 40,800 lb-in^2, respectively. English units are used for this tabular data because the manufacturer's springs are specified in this way. The bold column in both tables corresponds to the radius of the rotating disk, which is arguably the easiest distance to use for the spring moment-arm because of mounting ease and lack of interference with the rest of the system.

The spring rate values given at the maximum distance seem reasonable in both tables, so the disk radius is selected as the spring connection point. Based on Table 1, the spring constant needs to be less than 3.70 lb/in, but a spring load rate that is too small may exceed its yield strength during application. If we select springs that are 1 lb/in, the period is 1.926 s, which meets the design specifications. Looking at Table 2, the upper limit of spring load rate based on the maximum distance from the center of the disk is about 15 lb/in. There are two options to accommodate both the unoccupied and occupied-wheelchair scenarios: (a) select 1 spring for both cases, prioritizing the unoccupied case because the limits are more stringent or (b) have several springs of different load rates that could be interchanged on the device depending on the load being tested.

Table 1. Half-spring constant based on desired natural period and spring moment-arm (using lower bound, 10,000 lb-in^2, of inertia range)

	R (in)											
T_n (s)	6.00	6.50	7.00	7.50	8.00	8.50	9.00	9.50	10.00	10.50	11.00	**11.75**
1.0	14.190	12.091	10.425	9.082	7.982	7.071	6.307	5.660	5.108	4.634	4.222	**3.700**
1.1	11.727	9.993	8.616	7.506	6.597	5.843	5.212	4.678	4.222	3.829	3.489	**3.058**
1.2	9.854	8.397	7.240	6.307	5.543	4.910	4.380	3.931	3.548	3.218	2.932	**2.570**
1.3	8.397	7.154	6.169	5.374	4.723	4.184	3.732	3.349	3.023	2.742	2.498	**2.189**
1.4	7.240	6.169	5.319	4.634	4.072	3.607	3.218	2.888	2.606	2.364	2.154	**1.888**
1.5	6.307	5.374	4.634	4.036	3.548	3.142	2.803	2.516	2.270	2.059	1.876	**1.645**
1.6	5.543	4.723	4.072	3.548	3.118	2.762	2.464	2.211	1.996	1.810	1.649	**1.445**
1.7	4.910	4.184	3.607	3.142	2.762	2.447	2.182	1.959	1.768	1.603	1.461	**1.280**
1.8	4.380	3.732	3.218	2.803	2.464	2.182	1.947	1.747	1.577	1.430	1.303	**1.142**
1.9	3.931	3.349	2.888	2.516	2.211	1.959	1.747	1.568	1.415	1.284	1.169	**1.025**
2.0	3.548	3.023	2.606	2.270	1.996	1.768	1.577	1.415	1.277	1.158	1.055	**0.925**
2.1	3.218	2.742	2.364	2.059	1.810	1.603	1.430	1.284	1.158	1.051	0.957	**0.839**
2.2	2.932	2.498	2.154	1.876	1.649	1.461	1.303	1.169	1.055	0.957	0.872	**0.764**
2.3	2.682	2.286	1.971	1.717	1.509	1.337	1.192	1.070	0.966	0.876	0.798	**0.699**
2.4	2.464	2.099	1.810	1.577	1.386	1.228	1.095	0.983	0.887	0.804	0.733	**0.642**
2.5	2.270	1.935	1.668	1.453	1.277	1.131	1.009	0.906	0.817	0.741	0.676	**0.592**
2.6	2.099	1.789	1.542	1.343	1.181	1.046	0.933	0.837	0.756	0.685	0.625	**0.547**
2.7	1.947	1.659	1.430	1.246	1.095	0.970	0.865	0.776	0.701	0.636	0.579	**0.508**
2.8	1.810	1.542	1.330	1.158	1.018	0.902	0.804	0.722	0.652	0.591	0.539	**0.472**
2.9	1.687	1.438	1.240	1.080	0.949	0.841	0.750	0.673	0.607	0.551	0.502	**0.440**
3.0	1.577	1.343	1.158	1.009	0.887	0.786	0.701	0.629	0.568	0.515	0.469	**0.411**
3.1	1.477	1.258	1.085	0.945	0.831	0.736	0.656	0.589	0.532	0.482	0.439	**0.385**
3.2	1.386	1.181	1.018	0.887	0.779	0.690	0.616	0.553	0.499	0.452	0.412	**0.361**
3.3	1.303	1.110	0.957	0.834	0.733	0.649	0.579	0.520	0.469	0.425	0.388	**0.340**
3.4	1.228	1.046	0.902	0.786	0.690	0.612	0.546	0.490	0.442	0.401	0.365	**0.320**
3.5	1.158	0.987	0.851	0.741	0.652	0.577	0.515	0.462	0.417	0.378	0.345	**0.302**
3.6	1.095	0.933	0.804	0.701	0.616	0.546	0.487	0.437	0.394	0.358	0.326	**0.286**
3.7	1.037	0.883	0.762	0.663	0.583	0.516	0.461	0.413	0.373	0.338	0.308	**0.270**
3.8	0.983	0.837	0.722	0.629	0.553	0.490	0.437	0.392	0.354	0.321	0.292	**0.256**
3.9	0.933	0.795	0.685	0.597	0.525	0.465	0.415	0.372	0.336	0.305	0.278	**0.243**
4.0	0.887	0.756	0.652	0.568	0.499	0.442	0.394	0.354	0.319	0.290	0.264	**0.231**

Table 2. Half-spring constant based on desired natural period and spring moment-arm (using upper bound, 40,800 lb-in^2, of inertia range)

	R (in)											
T_n (s)	6.00	6.50	7.00	7.50	8.00	8.50	9.00	9.50	10.00	10.50	11.00	**11.75**
1.0	57.896	49.332	42.536	37.054	32.567	28.848	25.732	23.094	20.843	18.905	17.225	**15.097**
1.1	47.848	40.770	35.154	30.623	26.915	23.841	21.266	19.086	17.225	15.624	14.236	**12.476**
1.2	40.206	34.258	29.539	25.732	22.616	20.033	17.869	16.038	14.474	13.128	11.962	**10.484**
1.3	34.258	29.190	25.169	21.925	19.270	17.070	15.226	13.665	12.333	11.186	10.192	**8.933**
1.4	29.539	25.169	21.702	18.905	16.616	14.718	13.128	11.783	10.634	9.645	8.788	**7.702**
1.5	25.732	21.925	18.905	16.468	14.474	12.821	11.436	10.264	9.263	8.402	7.656	**6.710**
1.6	22.616	19.270	16.616	14.474	12.721	11.269	10.051	9.021	8.142	7.385	6.729	**5.897**
1.7	20.033	17.070	14.718	12.821	11.269	9.982	8.904	7.991	7.212	6.541	5.960	**5.224**
1.8	17.869	15.226	13.128	11.436	10.051	8.904	7.942	7.128	6.433	5.835	5.316	**4.659**
1.9	16.038	13.665	11.783	10.264	9.021	7.991	7.128	6.397	5.774	5.237	4.772	**4.182**
2.0	14.474	12.333	10.634	9.263	8.142	7.212	6.433	5.774	5.211	4.726	4.306	**3.774**
2.1	13.128	11.186	9.645	8.402	7.385	6.541	5.835	5.237	4.726	4.287	3.906	**3.423**
2.2	11.962	10.192	8.788	7.656	6.729	5.960	5.316	4.772	4.306	3.906	3.559	**3.119**
2.3	10.944	9.325	8.041	7.004	6.156	5.453	4.864	4.366	3.940	3.574	3.256	**2.854**
2.4	10.051	8.565	7.385	6.433	5.654	5.008	4.467	4.009	3.619	3.282	2.991	**2.621**
2.5	9.263	7.893	6.806	5.929	5.211	4.616	4.117	3.695	3.335	3.025	2.756	**2.415**
2.6	8.565	7.298	6.292	5.481	4.818	4.267	3.806	3.416	3.083	2.797	2.548	**2.233**
2.7	7.942	6.767	5.835	5.083	4.467	3.957	3.530	3.168	2.859	2.593	2.363	**2.071**
2.8	7.385	6.292	5.426	4.726	4.154	3.680	3.282	2.946	2.659	2.411	2.197	**1.926**
2.9	6.884	5.866	5.058	4.406	3.872	3.430	3.060	2.746	2.478	2.248	2.048	**1.795**
3.0	6.433	5.481	4.726	4.117	3.619	3.205	2.859	2.566	2.316	2.101	1.914	**1.677**
3.1	6.025	5.133	4.426	3.856	3.389	3.002	2.678	2.403	2.169	1.967	1.792	**1.571**
3.2	5.654	4.818	4.154	3.619	3.180	2.817	2.513	2.255	2.035	1.846	1.682	**1.474**
3.3	5.316	4.530	3.906	3.403	2.991	2.649	2.363	2.121	1.914	1.736	1.582	**1.386**
3.4	5.008	4.267	3.680	3.205	2.817	2.495	2.226	1.998	1.803	1.635	1.490	**1.306**
3.5	4.726	4.027	3.472	3.025	2.659	2.355	2.101	1.885	1.701	1.543	1.406	**1.232**
3.6	4.467	3.806	3.282	2.859	2.513	2.226	1.985	1.782	1.608	1.459	1.329	**1.165**
3.7	4.229	3.603	3.107	2.707	2.379	2.107	1.880	1.687	1.522	1.381	1.258	**1.103**
3.8	4.009	3.416	2.946	2.566	2.255	1.998	1.782	1.599	1.443	1.309	1.193	**1.045**
3.9	3.806	3.243	2.797	2.436	2.141	1.897	1.692	1.518	1.370	1.243	1.132	**0.993**
4.0	3.619	3.083	2.659	2.316	2.035	1.803	1.608	1.443	1.303	1.182	1.077	**0.944**

2.3.4.2 Geometric Constraints

In analyzing this problem, there are also geometric constraints to consider when selecting the springs. If the springs are attached in the plane of the disk, then the fully-stretched length of the spring should be no more than the distance between the fixed end of the spring and the point of contact on the disk. Figure 14 shows a close-up view of the spring geometry.

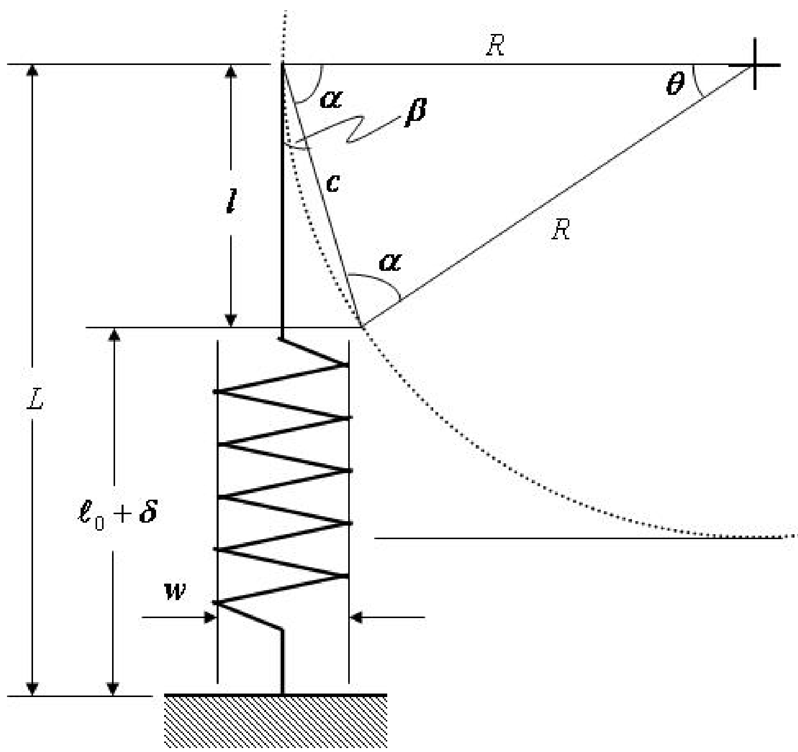

Figure 14. Model of the spring geometry and contact point on the rotating disk

The chord length *c* is computed using the following relation

$$c = 2R\sin\frac{\theta}{2} \tag{54}$$

but θ can be compared to α and β in the following manner

$$\theta + 2\alpha = 180^{\circ} \tag{55}$$

$$\alpha + \beta = 90^{\circ} \tag{56}$$

Substituting (56) into (55) and then (55) into (54), the chord length can be expressed in terms of β as

$$c = 2R\sin\beta = 2R\left(\frac{w/2}{c}\right) \tag{57}$$

Using the Pythagorean theorem,

$$l^2 + (w/2)^2 = c^2 \tag{58}$$

Substituting (57) into (58) yields

$$l^2 + (w/2)^2 = Rw \tag{59}$$

and solving for *l* gives the following expression

$$l = \sqrt{w\left(R - \frac{w}{4}\right)} \tag{60}$$

The stretched length of the spring, $\ell_0 + \delta$, must be no greater than the difference between *l* and the total distance from the fixed end to the center of the disk, *L*; that is,

$$\ell_0 + \delta \le L - l \tag{61}$$

or, in other words, the maximum elongation of the spring beyond its unstretched length is

$$\delta_{\max} = L - \sqrt{w\left(R - \frac{w}{4}\right)} - \ell_0 \tag{62}$$

In this problem, *L* is equal to 13.5 in, and *R* is 11.75 in. Since the spring needs to be in tension at all times, it is a good idea to set $\delta_{\max}$ at twice as large as the desired distance through which the disk will rotate; in other words,

$$\delta_{\max} = 2s_0 = 2R\theta_0 \tag{63}$$

Table 3 lists the variation in maximum initial angular displacement, θ_0, based on the selection of spring width, *w*, and overall unstretched length, l_0.

Table 3. Maximum angular displacement (in degrees) based on spring parameters.

	w (in)							
l_0 (in)	3/32	1/8	3/16	1/4	3/8	1/2	5/8	3/4
0.50	23.653	23.259	22.598	22.042	21.112	20.332	19.647	19.030
0.75	23.044	22.649	21.989	21.433	20.503	19.722	19.037	18.420
1.00	22.434	22.040	21.379	20.823	19.893	19.113	18.428	17.811
1.25	21.825	21.430	20.770	20.214	19.284	18.503	17.818	17.201
1.50	21.215	20.821	20.160	19.604	18.674	17.894	17.209	16.592
1.75	20.606	20.211	19.550	18.995	18.065	17.284	16.599	15.982
2.00	19.996	19.602	18.941	18.385	17.455	16.675	15.990	15.373
2.25	19.387	18.992	18.331	17.775	16.846	16.065	15.380	14.763
2.50	18.777	18.383	17.722	17.166	16.236	15.455	14.770	14.154
2.75	18.168	17.773	17.112	16.556	15.627	14.846	14.161	13.544
3.00	17.558	17.164	16.503	15.947	15.017	14.236	13.551	12.935
3.25	16.949	16.554	15.893	15.337	14.408	13.627	12.942	12.325
3.50	16.339	15.945	15.284	14.728	13.798	13.017	12.332	11.716
3.75	15.730	15.335	14.674	14.118	13.188	12.408	11.723	11.106
4.00	15.120	14.725	14.065	13.509	12.579	11.798	11.113	10.497
4.25	14.510	14.116	13.455	12.899	11.969	11.189	10.504	9.887
4.50	13.901	13.506	12.846	12.290	11.360	10.579	9.894	9.278
4.75	13.291	12.897	12.236	11.680	10.750	9.970	9.285	8.668
5.00	12.682	12.287	11.627	11.071	10.141	9.360	8.675	8.058
5.25	12.072	11.678	11.017	10.461	9.531	8.751	8.066	7.449
5.50	11.463	11.068	10.408	9.852	8.922	8.141	7.456	6.839
5.75	10.853	10.459	9.798	9.242	8.312	7.532	6.847	6.230
6.00	10.244	9.849	9.188	8.633	7.703	6.922	6.237	5.620
6.25	9.634	9.240	8.579	8.023	7.093	6.313	5.628	5.011
6.50	9.025	8.630	7.969	7.413	6.484	5.703	5.018	4.401
6.75	8.415	8.021	7.360	6.804	5.874	5.093	4.408	3.792
7.00	7.806	7.411	6.750	6.194	5.265	4.484	3.799	3.182
7.25	7.196	6.802	6.141	5.585	4.655	3.874	3.189	2.573
7.50	6.587	6.192	5.531	4.975	4.046	3.265	2.580	1.963
7.75	5.977	5.583	4.922	4.366	3.436	2.655	1.970	1.354
8.00	5.368	4.973	4.312	3.756	2.826	2.046	1.361	0.744

With the availability of high-resolution encoders, it is assumed that the rotation of the disk will be on the order of a few degrees. Looking at the data, nearly any combination of spring geometric parameters will allow sufficient angular displacement for the encoder to properly measure the data. Therefore, the geometric constraints will most likely be met for the given system design and spring placement. However, this exercise is important in deriving the operating limits of the system once springs have been selected.

2.3.4.3 Spring Selection

With the aforementioned constraints in mind, a set of precision stainless steel extension springs (McMaster-Carr Inc., Santa Fe Springs, CA) was selected. The spring rate of each spring is specified by the manufacturer to equal 588 N/m (3.36 lb/in), so the equivalent spring rate of the iMachine system is 1177 N/m (6.72 lb/in). The spring width and unstretched length are 15.875 mm (5/8 in) and 7.94 cm (3.126 in), respectively. Based on Table 3, this means that the disk can be rotated more than 13° before the spring will contact the disk. Since the springs do not operate in compression, the spring static displacement must be greater than the desired amplitude of oscillation. One end of the spring connects to the fixed structural frame via a steel eyebolt and the other end hooks to flexible steel rope. The rope wraps around the middle of the disk and a screw pins the rope to the disk at the back. A picture of the spring in static equilibrium is shown in Figure 15. The natural period of oscillation for the unoccupied and occupied wheelchair scenarios is estimated using Table 1 and Table 2 to be approximately 1.1 s and 2.1 s, respectively.

Figure 15. iMachine extension spring in static equilibrium

2.3.5 X-Y Positioning Platform

One of the significant challenges in operating an apparatus to empirically measure the moment of inertia of a large object is the centering the test piece CG on the axis of rotation. To address this issue, the iMachine design includes an X-Y positioning platform to allow for easy repositioning of the test piece in two directions. The platform has similar outer dimensions to the structural frame and is made from the same extruded aluminum parts (80/20 Inc., Columbia City, IN). The platform interfaces with the disk at three contact points, one on each of the load cells. There are three small rods attached to the bottom of the platform that fit in copper bushings mounted to the disk. The rods improve stability by constraining the lateral motion of the platform. Additionally, this platform design ensures that the load is transferred solely through the load cells, while reducing the shear force on the load cells. Figure 16 illustrates the final platform design.

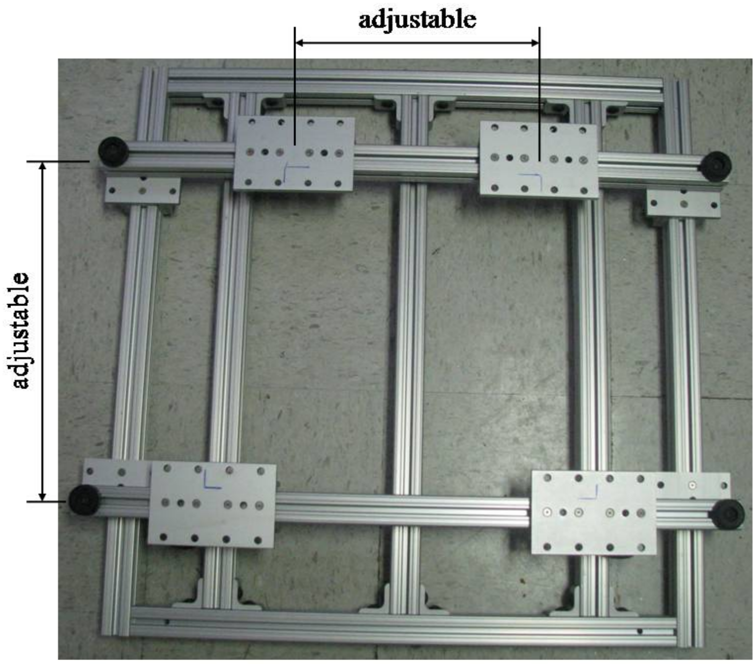

Figure 16. iMachine X-Y positioning platform

The coordinate system in Figure 16 is the same in Figure 10, so that the positive *y*-axis points towards the top of the page. Each bearing is adjustable in one direction based on the orientation of the beam to which it is mounted. Considering only the geometric dimensions of the platform frame, the total stroke lengths in the *x* and *y* directions are 74.93 cm (29.5 in) and 68.58 cm (27 in), respectively. The adjustable range of each bearing is constrained, however, by its dimensions and the fact that each beam contains two bearings. For example, the bearing in the bottom left cannot move all the way to the right end because there is another bearing in the way. Taking into account these constraints, the stroke length for each bearing from the center of the beam is 22.2 cm (8.75 in) in the *x*-direction and 27.1 cm (10.675 in) in the *y*-direction.

During a test, the wheelchair is mounted to the top four linear bearings on the platform. The rear drive wheels attach to the two bearings in the bottom of the figure, while the casters are fixed to the top two bearings. This biases the heavier regions of the wheelchair toward the part of the disk with load cells B and C (refer to Figure 10). Once the wheels are fixed to their respective bearings, the bearings include handles that lock them into place.

2.3.6 Hardware

2.3.6.1 Load Cells

The design specifications for the load cells are that they be low profile, easy to mount, high resolution sensors with load capacity greater than the maximum anticipated weight of the platform and occupied wheelchair. The transducers that were selected are LCGB-250 series miniature industrial compression load cells (Omega Engineering Inc., Stamford, CT). The cells have a button-type interface for even force distribution, and three mounting holes for easy attachment to a flat surface such as the iMachine disk. The load capacity of each is 250 lb, so that the total weight capacity of the load cell supports (750 lb) is more than the anticipated maximum load (300 lb). These have the optimal combination of capacity and resolution that was found and should be sufficient for the measurement technique of this device. The load cell is 32 mm (1.25 in) in diameter and 10 mm (0.39 in) in overall height. The output of each load cell is a differential analog signal on the order of 20mV with 10V nominal excitation. A picture of the load cell mounted to the iMachine disk is illustrated in Figure 17.

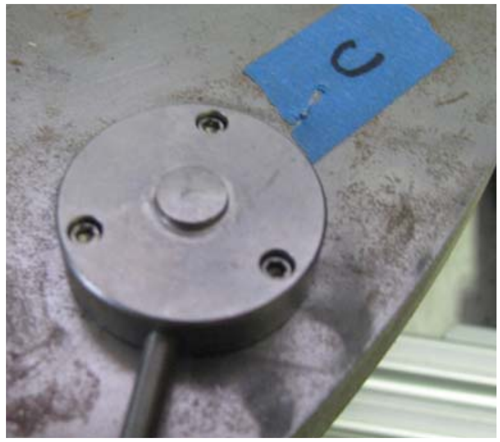

Figure 17. Load cell mounted to iMachine disk

2.3.6.2 Encoder

An optical encoder generally consists of a code wheel, detector module, and mounting housing, as shown in Figure 18.

Figure 18. Optical encoder components (U.S. Digital Inc.)

The code wheel mounts to the rotating shaft, while the detector module remains stationary. The module usually contains a light-emitting diode (LED) source on one end and a detector on the other. As the code wheel rotates, the LED signal is either detected or not, depending on the transparency of the wheel at that location. Monitoring the signal continuously over time creates a squarewave output that can be processed to get the angular position.

The only major design parameter for the encoder is its resolution because it dictates the uncertainty in the angular position measurement. With this in mind, an E3 series optical encoder (U.S. Digital Inc., Vancouver, WA) was selected that has 2 channel quadrature outputs with 2500 Cycles Per Revolution (CPR). Quadrature simply refers to the fact that there are two patterns on the code wheel that produce signals which are out of phase. The phase lag, *Z*, between the two channels determines the resolution of the transducer. Nominally, *Z* equals 1/4 of one cycle, so that the resolution, $\Delta\theta$, is given by

$$\Delta\theta = \frac{1}{4}\,\text{cycles}\left|\frac{1\,\text{rev}}{2500\,\text{cycles}}\right|\left|\frac{360^\circ}{1\,\text{rev}}\right| = 0.036^\circ \tag{64}$$

Figure 19 shows an example of the quadrature output for the encoder. The numbered lines in the figure represent the four possible “states” of the output signal.

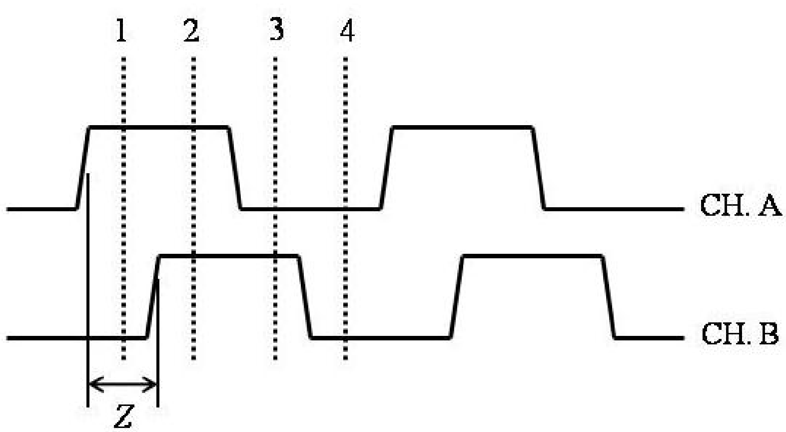

Figure 19. Encoder quadrature output

Assigning incremental sequencing (1,2,3,4) to clockwise (CW) rotation and decremental sequencing (4,3,2,1) to counter-clockwise (CCW) rotation, the angular position of the system can be monitored using the key presented in Table 4. The numbers listed in the column on the left refer to the state recorded at the *i*th time point, and the top column lists the state of the (*i*+1)th time.

Table 4. Encoder state changes and their meaning

		state(i+1)			
		1	2	3	4
state(i)	1	0	+	NA	-
	2	-	0	+	NA
	3	NA	-	0	+
	4	+	NA	-	0

A positive (+) sign indicates the angular position has increased by an amount equal to the encoder resolution, while a negative (-) sign indicates the position has decreased by the same amount. If the state remains the same across two successive data points, it is assumed that the angular position is unchanged. There are also several cases that are not applicable (NA), which means that it is impossible to progress from the *i*th state to the (*i*+1)th states without skipping states. In order to ensure that all states are counted, the time interval between sampled data points must be less than the time it takes to rotate $\Delta\theta$ degrees. For example, if the maximum rotation rate is $\pi/4$ rad/s, then the minimum sampling rate that guarantees each encoder state will be detected is

$$f_{\min} = \frac{\omega_{\max}}{\Delta\theta} = \frac{\pi/4\ \text{rad/s}}{0.036^{\circ}} \left| \frac{180^{\circ}}{\pi\ \text{rad}} \right| = 1250\ \text{Hz} \tag{65}$$

Initially, it is assumed that the prescribed maximum angular speed in (65) is an acceptable upper bound for the iMachine. In addition, it is desired to detect two or more points within each state. Therefore, the minimum sampling rate was set to 2500 Hz, and later tests confirmed that this meets the specifications described here.

The encoder bore size is 10 mm, which defines the diameter of the necessary step size on the bottom of the shaft. The housing mounts to a plate that is rigidly attached to the bottom structural frame of the iMachine. A picture of the mounted setup is shown in Figure 20.

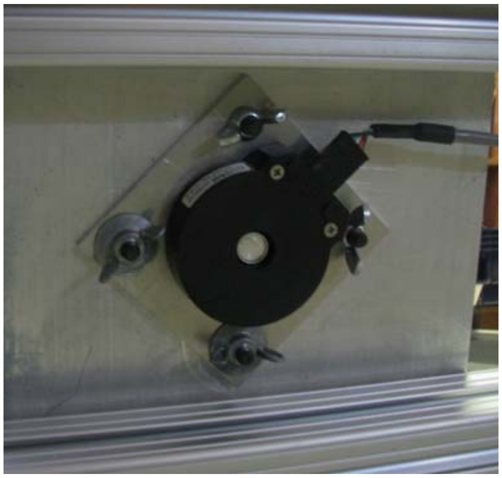

Figure 20. Encoder mounted to bottom of iMachine frame

2.3.6.3 LabJack U6 DAQ Device

The data acquisition device (DAQ) that was selected for this project is the U6 (LabJack Corporation, Lakewood, CO). It has 14 analog input (AI) channels and 20 digital I/O (DI) channels. There are several software programmable gains and varying AI ranges. This is sufficient for the iMachine, which only requires 3 single-ended AI channels for the load cells and 2 DI channels for the quadrature encoder output. Instrumentation amplifiers are used to convert the differential signals from the load cells to single-ended signals. The analog input range of $\pm 0.1\text{V}$ is used to increase resolution since the load cell outputs is on the order of mV. The U6 device can stream input data at rates up to 50 kHz, which is more than enough for the predicted requirements of the iMachine hardware described previously. It supports most programming languages and connects to a personal computer (PC) via USB cable. The LabJack U6 device is pictured below in Figure 21.

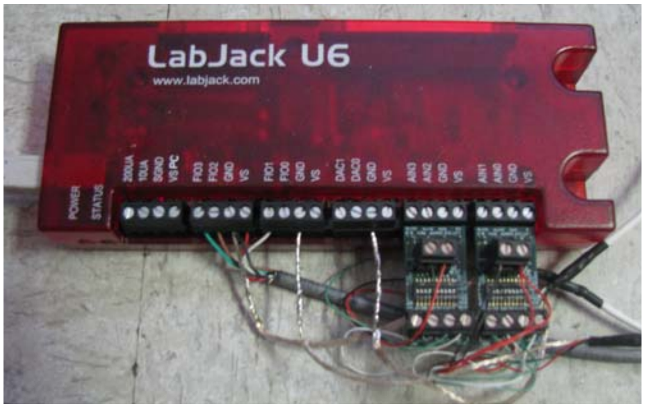

Figure 21. LabJack U6 DAQ device

2.3.7 Software

2.3.7.1 LabVIEW: Data Acquisition

A graphical user interface (GUI) was developed using LabVIEW software (National Instruments Corp., Austin, TX). The purpose of the GUI is to properly stream data from the LabJack U6 and write the important data arrays to a comma-separated values (CSV) file for use with other software. LabVIEW uses code functions provided in

LabJack’s dynamic linked library (DLL) to properly configure the DAQ device and stream the data according to controllable parameters. The GUI is programmed to display the weight of the system on the load cells, the location of the system CG with respect to the axis of rotation, and the angular position of the platform in real time. Figure 22 shows the LabVIEW iMachine GUI, and Figure 23 displays a portion of the block diagram for the code.

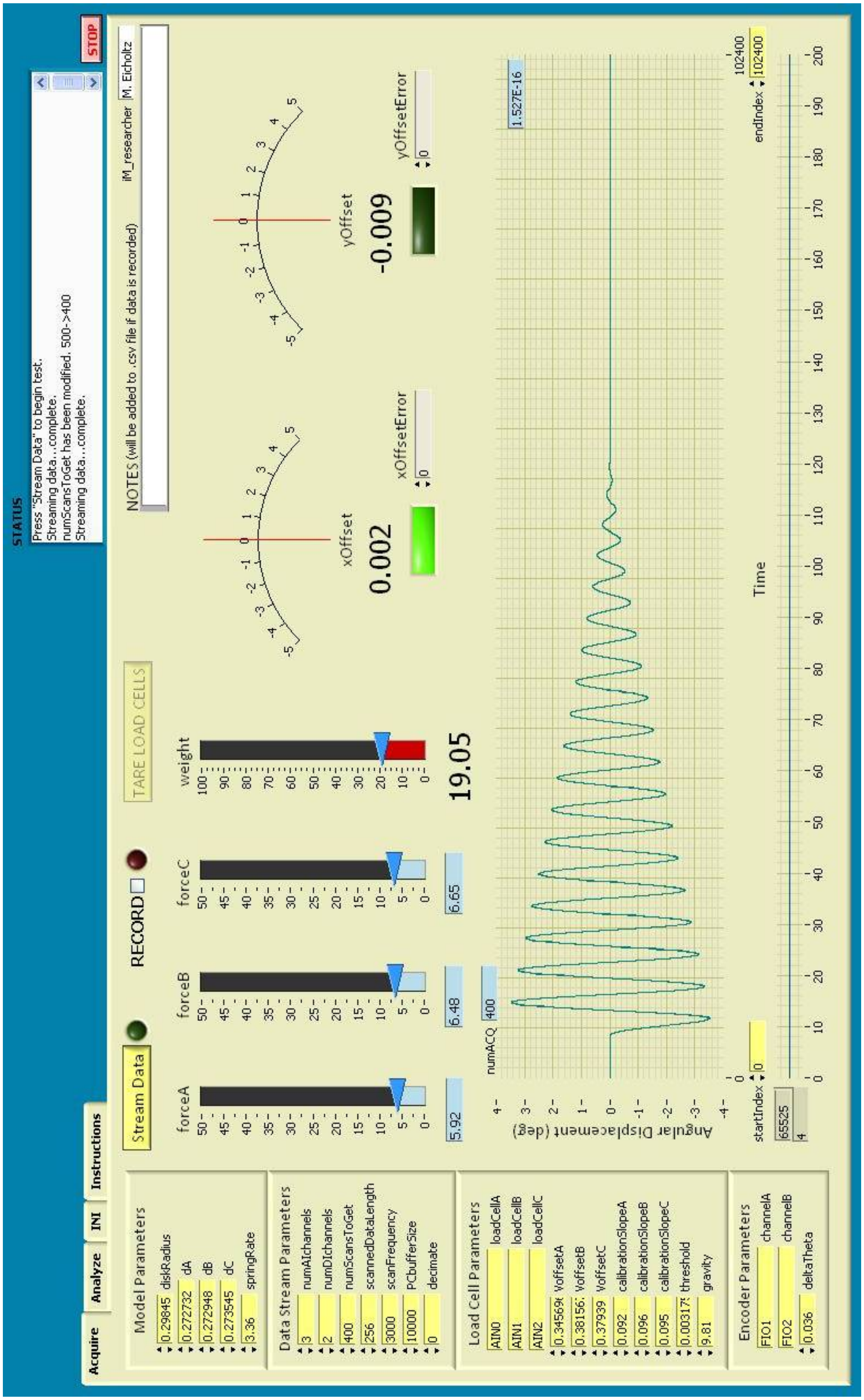

Figure 22. LabVIEW iMachine GUI front panel

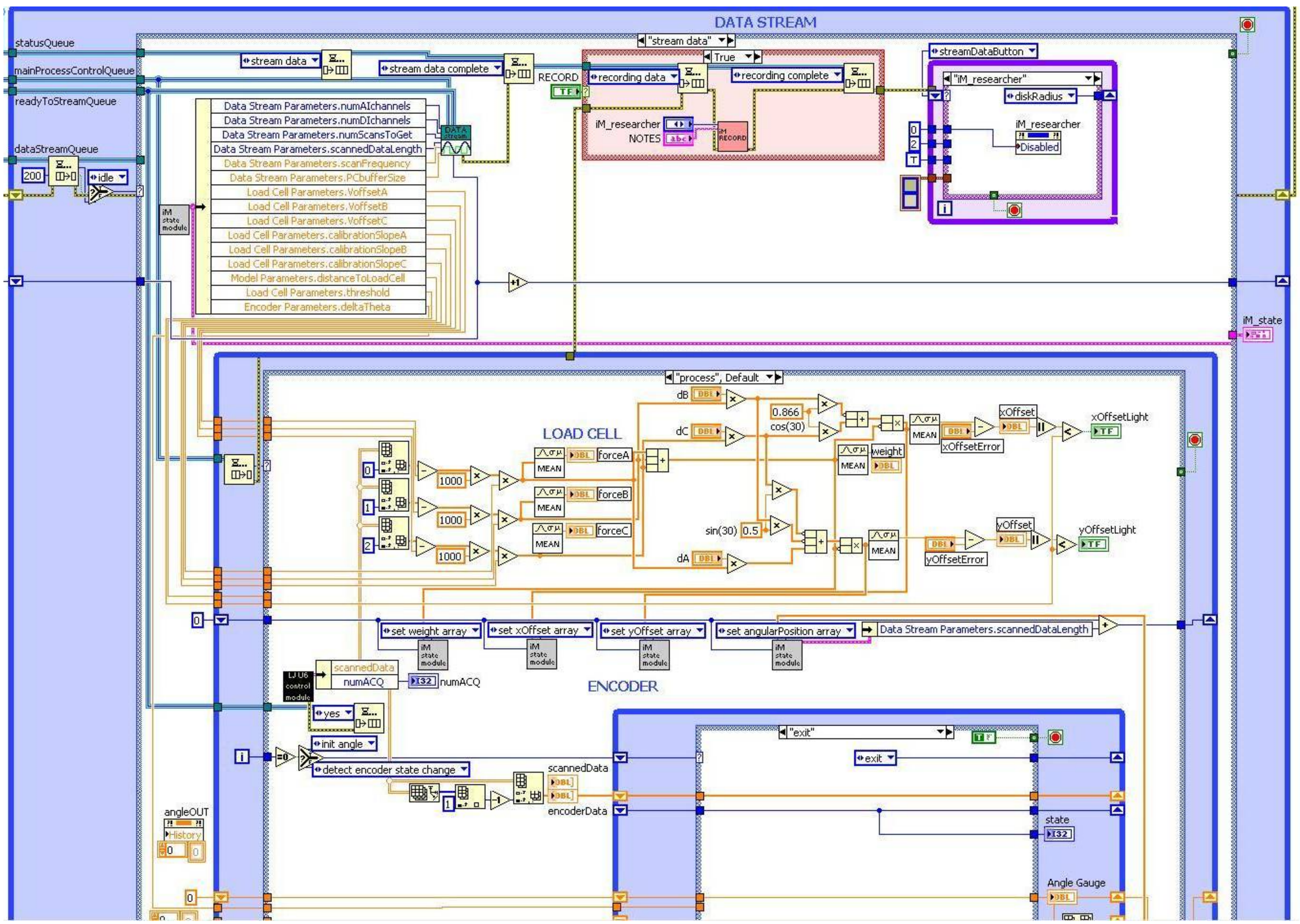

Figure 23. LabVIEW iMachine GUI block diagram (data streaming section)

2.3.7.2 MATLAB: Data Analysis

Once the test data has been acquired using the LabVIEW GUI, it is processed and analyzed using a series of functions developed in MATLAB software (The MathWorks Inc., Natick, MA). The functions draw on the theory developed previously in this thesis and the measurement approach outlined in the next chapter to calculate the desired moment of inertia term.

2.4 Summary

This chapter has delineated the design selection, theoretical inertia calculations, and component specification for the iMachine. A picture of the final constructed device is illustrated in Figure 24.

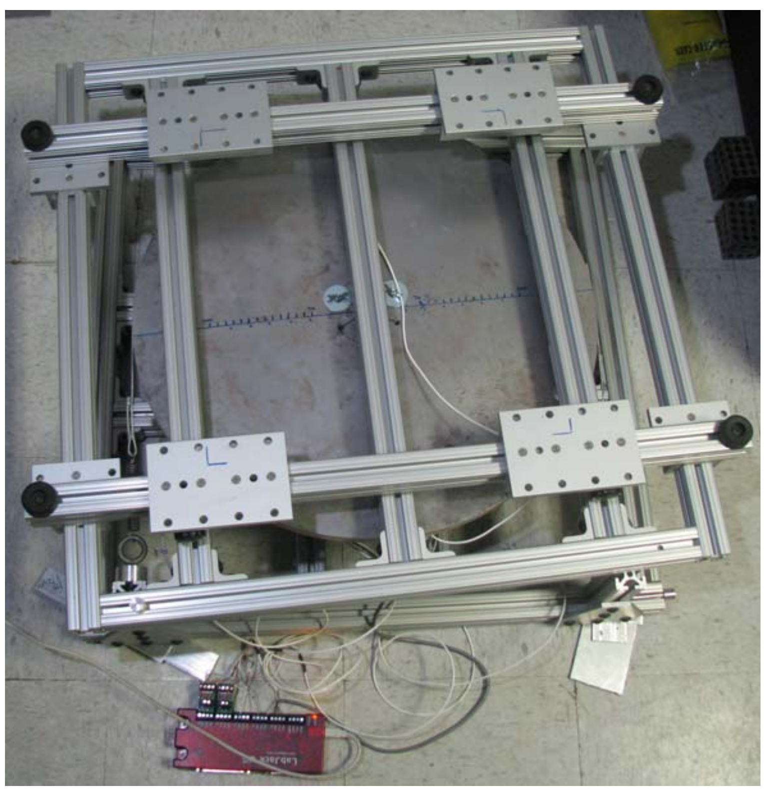

Figure 24. iMachine in rotation

CHAPTER 3

MEASUREMENT APPROACH

Now that the theory has been described and the design components detailed, this chapter discusses the specific measurement approach for using the iMachine effectively. In the sections that follow, the test procedures and calculations will be presented that are utilized to solve for the mass, location of the center of mass, and moment of inertia of a manual wheelchair.

3.1 Mass

The first portion of the test procedure is carried out under static conditions. To begin, the mass of the platform is read and recorded using the LabVIEW GUI. Then, the wheelchair is fixed to the appropriate linear bearings on the positioning platform using cable ties. The total system mass is now recorded. The mass of the wheelchair, m_{WC}, is calculated by taking the difference of the two measurements,

$$m_{\mathrm{WC}} = m_{\mathrm{sys}} - m_{\mathrm{platform}} \tag{66}$$

where m_{sys} is the mass of the wheelchair and platform, and m_{platform} is the mass of the platform only.

3.2 Center of Mass Coordinates

The center of mass is located by summing the moments about *x* and *y*-axes as shown in Figure 10,

$$\begin{aligned} \sum M_x &= 0: F_{\mathrm{A}} d_{\mathrm{A}} - F_{\mathrm{B}} d_{\mathrm{B}} \sin 30^\circ - F_{\mathrm{C}} d_{\mathrm{C}} \sin 30^\circ - F_{\mathrm{total}} Y_{\mathrm{G}} = 0 \\ \sum M_y &= 0: F_{\mathrm{B}} d_{\mathrm{B}} \cos 30^\circ - F_{\mathrm{C}} d_{\mathrm{C}} \cos 30^\circ + F_{\mathrm{total}} X_{\mathrm{G}} = 0 \end{aligned} \tag{67}$$

where (X_G, Y_G) are the center of mass coordinates for the entire system, F_A, F_B, and F_C are the load cell forces, and the total weight is given by

$$F_{\text{total}} = F_A + F_B + F_C \tag{68}$$

Even though the design calls for each of the load cells to be equidistant from the center of the disk, measurements demonstrated that this is not true, so d_A, d_B, and d_C are used to represent the radial distance from each load cell to the axis of rotation. Solving for the location of the center of mass,

$$X_G = \frac{(F_C d_C - F_B d_B)\cos 30^\circ}{F_A + F_B + F_C}; \quad Y_G = \frac{F_A d_A - (F_B d_B + F_C d_C)\sin 30^\circ}{F_A + F_B + F_C}; \tag{69}$$

Therein, if the distances are measured by hand, the total system CG can be located by simply using the three load cell measurements. It is important to note that results in (69) refer to the entire system that is on top of the load cells, not just the wheelchair. In the next section, the location of the wheelchair CG alone will be derived concurrently with measuring the moment of inertia.

3.3 Moment of Inertia

At this point, the wheelchair can be repositioned on the disk by moving the linear bearings along the aluminum extrusions of the platform. In this way, the location of the system center of mass can be driven to approximately zero. The purpose of centering the system CG is to reduce the stress on the shaft and the effect of rotating imbalances on the measurement. This concludes the static analysis portion of the test. In the dynamic portion of the test, the disk/platform/wheelchair assembly may be given an initial angular displacement, θ_0, and released from rest. However, the researchers found this approach to be difficult because of the inability to hold the platform still at an initial angular displacement. In practice, therefore, the system was given an initial angular velocity, v_0, from an angular position equal to zero. The output signal is much cleaner using this approach, so this method was followed for the remainder of the tests presented in this thesis. The system will oscillate freely about the center of the disk, and the encoder measures the angular position as a function of time. A plot of the angular position is qualitatively similar to the simulation shown in Figure 25 below, which is for the case of release from an initial angle. From the recorded data, the natural period can be determined using either time-domain or frequency-domain techniques, which are described below.

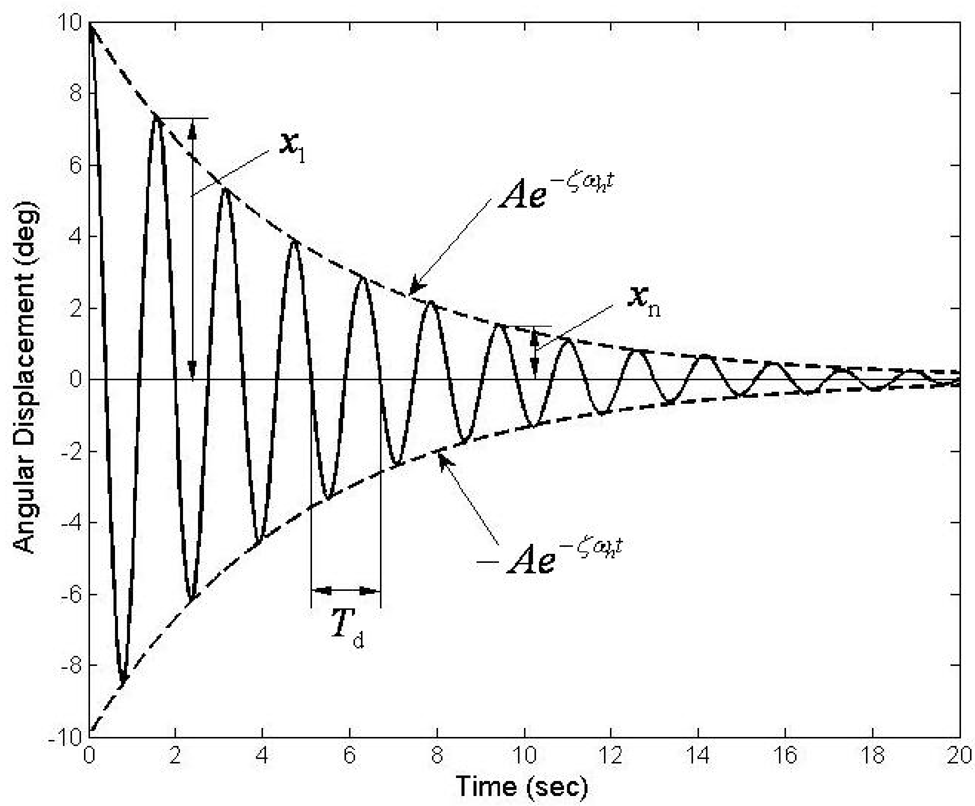

Figure 25. MATLAB simulation of typical second-order underdamped transient response

3.3.1 Time-Domain Methods

The first method for determining the natural period of oscillation is counting the critical points of the response. If zero crossings are counted, then the damped period equals the difference between every three points. If maxima or minima are counted, then the damped period is equal to the difference between successive points. The damping ratio can be found experimentally by comparing the ratio of successive maxima and solving for the log decrement, δ, using the equation

$$\delta = \ln\left(\frac{x_j}{x_{j+1}}\right) = \frac{2\pi\zeta}{\sqrt{1-\zeta^2}} \tag{70}$$

where x_j and x_{j+1} are the *j*th and (*j*+1)th amplitude of successive maxima. Rearranging the above equation to solve for the damping ratio yields

$$\zeta = \frac{\delta}{\sqrt{4\pi^2 + \delta^2}} \tag{71}$$

Then, the natural period of oscillation can be calculated using (35).

3.3.2 Frequency-Domain Methods

The second method for finding the natural period of oscillation is to perform a Fast Fourier Transform (FFT) on the data. An FFT is simply an efficient algorithm that performs a Discrete Fourier Transform (DFT), which transforms discrete-valued time data into complex amplitudes in the frequency domain using the equation

$$G_k = \sum_{n=0}^{N-1} g_k \exp\left(-2\pi i \frac{kn}{N}\right), \qquad k = 0,1,\ldots,N\text{-}1 \tag{72}$$

where G_k is the kth Fourier coefficient, g_k is the kth data point in the time domain, and N is the number of data points. The frequency associated with each Fourier coefficient can be computed as follows

$$\omega_k = k\omega_1 = \frac{2\pi k}{T} \tag{73}$$

where ω_1 is the fundamental frequency, and T is the length or duration of the data record. The algorithm assumes that the discrete time data repeats every T seconds and that N data points refers to one period. The highest frequency that can be computed is called the Nyquist critical frequency, which is equal to the ($N/2$)th harmonic, or

$$\omega_{\mathrm{cr}} = \frac{N}{2}\omega_1 \tag{74}$$

A plot of the frequency spectrum of a free response should reveal a dominant frequency that is very close to the maximum-response frequency in a harmonically-driven SDOF system. In a system with viscous damping, the complex frequency response is given by

$$D(r,\zeta) = \frac{1}{1+2i\zeta r - r^2}, \quad r = \frac{\omega}{\omega_{\mathrm{n}}} \tag{75}$$

where r is the ratio between the excitation and natural frequencies. Ginsberg [15] solves for the frequency at which the maximum complex amplitude occurs, and the result is

$$r = \left(1 - 2\zeta^2\right)^{1/2} \quad \text{for } \max(|D|) \tag{76}$$

To ascertain the value of the damping ratio for the system, let us first examine the frequency response of the system, an example of which is illustrated in Figure 26. The half-power points are the frequencies that correspond to the 70.7% of the maximum amplitude. The bandwidth of the system, $\Delta\omega$, is defined as the difference between the two half-power points. The quality factor (QF) is a measure of the narrowness of the maximum peak, and for a lightly damped system it can be estimated as [15]:

$$\mathrm{QF} = \frac{\omega_\mathrm{n}}{\Delta\omega} \approx \frac{1}{2\zeta} \tag{77}$$

Therefore, if the natural frequency is known and the bandwidth is measured, the damping ratio can be calculated from

$$\zeta \approx \frac{\Delta\omega}{2\omega_\mathrm{n}} \tag{78}$$

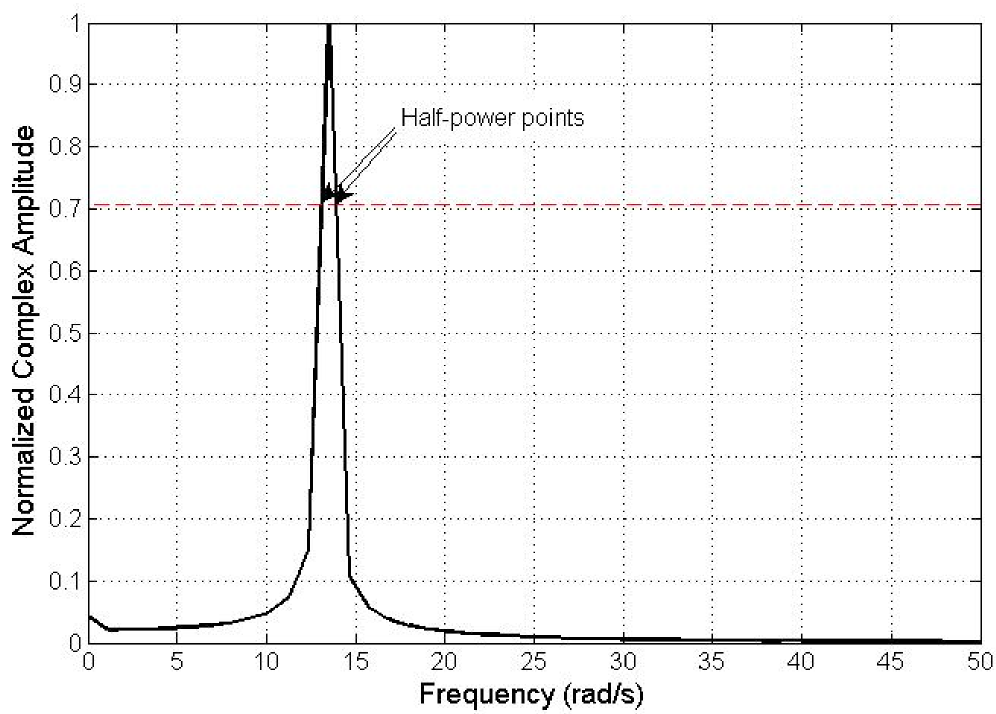

Figure 26. Sample frequency response of SDOF system showing half-power points

For systems with light damping, the peak frequency is approximately equal to the natural frequency. For systems with structural damping, the peak frequency is always equal to the natural frequency, regardless of the structural damping loss factor. The natural period of oscillation is related to the natural frequency in the following manner,

$$\omega_{\mathrm{n}} = \frac{2\pi}{T_{\mathrm{n}}} \tag{79}$$

3.3.3 Solving for the Inertia of the Manual Wheelchair

Once the natural period of oscillation is known, the moment of inertia can be calculated using (34). It is important to note that the inertia calculated here refers to the moment of inertia of the *entire system* about the axis of rotation. In order to find the moment of inertia for the wheelchair alone, we must consider the inertia of each system component; that is,

$$\left(I_{zz}^{\mathrm{O}}\right)_{\mathrm{sys}} = \left(I_{zz}^{\mathrm{O}}\right)_{\mathrm{disk}} + \left(I_{zz}^{\mathrm{O}}\right)_{\mathrm{platform}} + \left(I_{zz}^{\mathrm{O}}\right)_{\mathrm{WC}} \tag{80}$$

where, in general, $\left(I_{zz}^{\mathrm{O}}\right)_{\mathrm{C}}$ refers to the moment of inertia of the component C about the *z*-axis passing through point O. In order to determine $\left(I_{zz}^{\mathrm{O}}\right)_{\mathrm{WC}}$, the wheelchair is removed, and the dynamic test is executed again. It is important that the platform configuration remain unchanged during this process so that its mass distribution is uniform across tests. When the moment of inertia is calculated a second time, it will include the same components as described by (80) with the exception of the wheelchair inertia; that is,

$$\left(I_{zz}^{\mathrm{O}}\right)_{\mathrm{sys,2}} = \left(I_{zz}^{\mathrm{O}}\right)_{\mathrm{disk}} + \left(I_{zz}^{\mathrm{O}}\right)_{\mathrm{platform}} \tag{81}$$

Therefore, the moment of inertia of the wheelchair can be calculated as

$$\left(I_{zz}^{\mathrm{O}}\right)_{\mathrm{WC}} = \left(I_{zz}^{\mathrm{O}}\right)_{\mathrm{sys}} - \left(I_{zz}^{\mathrm{O}}\right)_{\mathrm{sys,2}} \tag{82}$$

However, the analysis is not yet complete because the point O is *not* on the vertical axis passing through the wheelchair's center of mass. To demonstrate this concept, Figure 27-

Figure 30 track the location of the center of mass of each component throughout the test. For simplicity, assume that both the platform and the wheelchair are point masses with magnitude equal to their respective total mass and located at their respective center of mass. Also, for this example, assume that the wheelchair is occupied such that the mass of the wheelchair is greater than the mass of the platform. Finally, assume that the disk is inherently centered about the origin so that its inertia calculation does not require the parallel axis theorem.

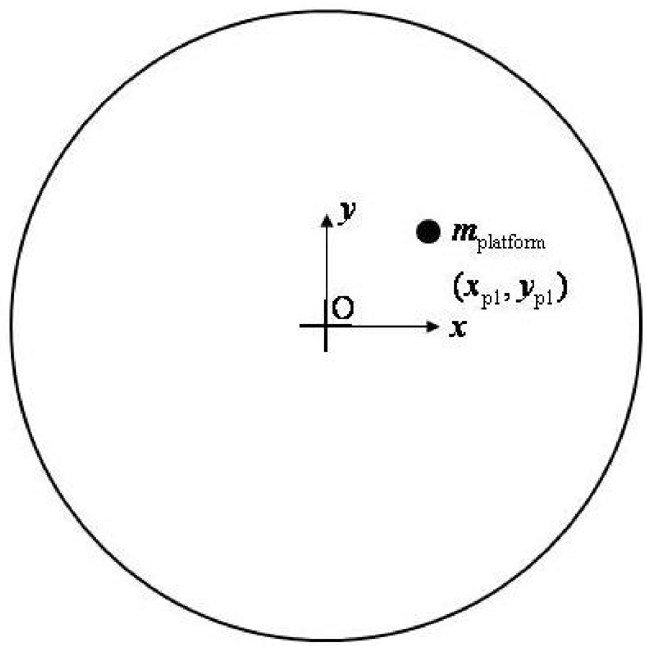

Figure 27. CG schematic (initial platform position)

At the beginning of the test, only the platform is detected by the load cells; Figure 27 shows a possible situation where the CG coordinates (x_{p1}, y_{p1}) are located in Quadrant I. Figure 28 illustrates the CG locations when the wheelchair is added to the system.

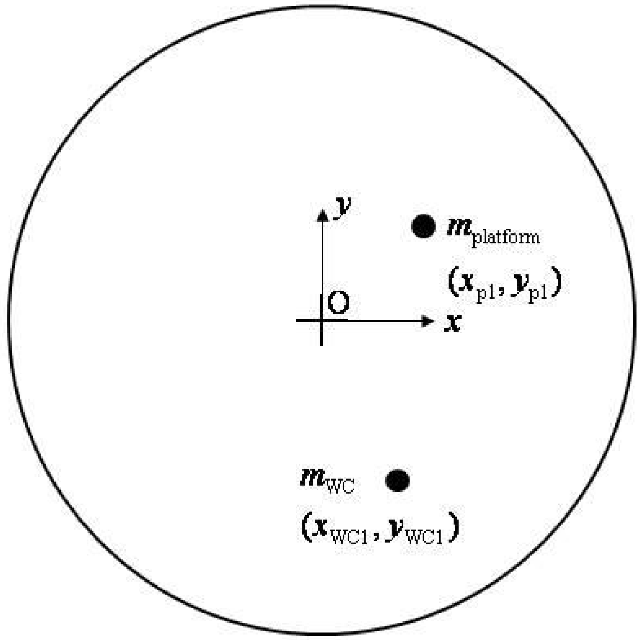

Figure 28. CG schematic (after wheelchair is added)

Once again, the position of the wheelchair (x_{WC1}, y_{WC1}). is somewhat arbitrary in this figure, but it is assumed that the CG is biased toward the negative *y*-direction because the heavier drive wheels are located toward that end. Note that neither of the coordinates need to be equal for the wheelchair and platform, although it is possible that the *x*-coordinates be the same, which would simplify the problem. At this point, the wheelchair is repositioned on the bearings to (ideally) zero the system CG. Figure 29 shows this concept, and several observations can be made accordingly.

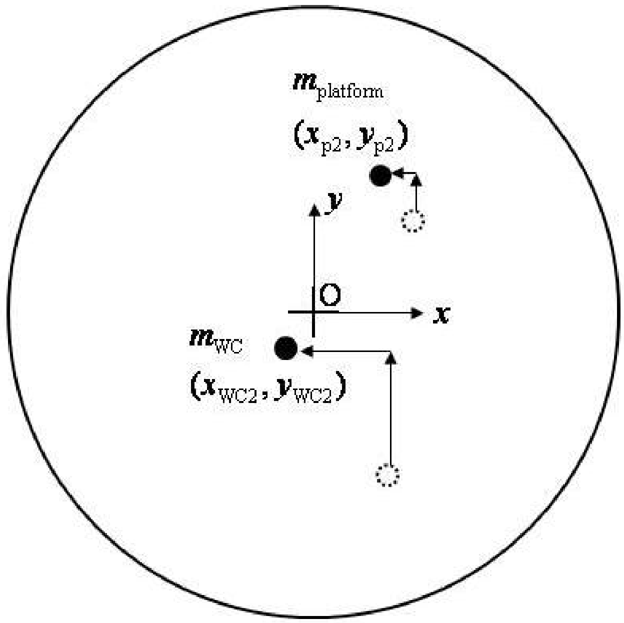

Figure 29. CG schematic (after moving wheelchair and platform to zero system CG)

Note that the center of mass of the platform moves as well, but in smaller increments. This effect happens because an arbitrary movement of the system center of mass corresponds to movement of the entire wheelchair but only partial movement of the platform (the linear bearings). It can also be seen that

$$\frac{\Delta x_{\text{p}}}{\Delta x_{\text{WC}}} < \frac{\Delta y_{\text{p}}}{\Delta y_{\text{WC}}} \tag{83}$$

because more platform mass (the aluminum extrusion connecting the linear bearings) is moved during a repositioning in the *y*-direction than the *x*-direction. Also, even though the platform is assumed to be symmetric about the *yz*-plane, the figure assumes a small asymmetry in the wheelchair mass distribution about this plane. If the wheelchair were indeed aligned symmetrically about the *yz*-plane, as is the ideal case, then both x_{WC2} and x_{p2} would be zero. The most distinguishing characteristic of Figure 29, though, is that the wheelchair center of mass is not located at the origin. Still, the calculated moment of inertia in (74) refers to the configuration shown in this figure. To resolve this challenge, simply record the system center of mass location when the wheelchair is removed (Figure 30), which corresponds to $(x_{\mathrm{p2}}, y_{\mathrm{p2}})$.

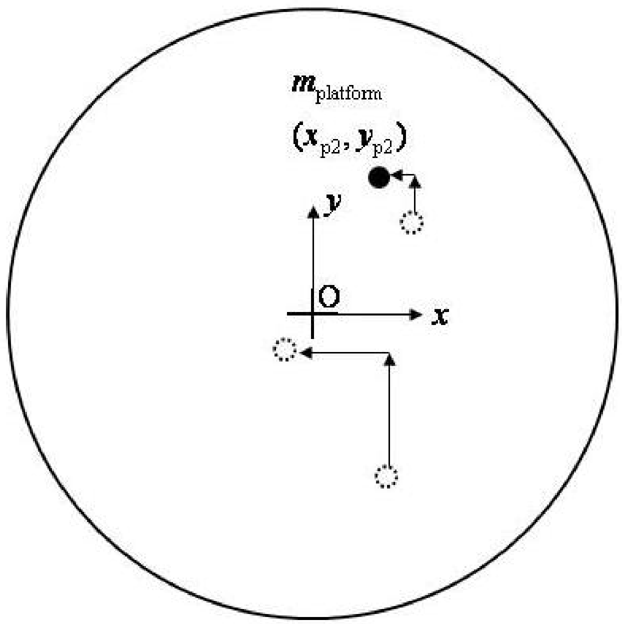

Figure 30. CG schematic (after removing wheelchair)

The coordinates $(x_{\mathrm{WC2}}, y_{\mathrm{WC2}})$ can be determined by taking a sum of the moments in Figure 29,

$$\begin{aligned} \sum M_x &= 0 : -m_{\mathrm{platform}} g y_{\mathrm{p2}} + m_{\mathrm{WC}} g y_{\mathrm{WC2}} = MgY_{\mathrm{CG}} \\ \sum M_y &= 0 : m_{\mathrm{platform}} g x_{\mathrm{p2}} - m_{\mathrm{WC}} g x_{\mathrm{WC2}} = -MgX_{\mathrm{CG}} \end{aligned} \tag{84}$$

and solving for the wheelchair coordinates

$$x_{\mathrm{WC2}} = \frac{m_{\mathrm{platform}} x_{\mathrm{p2}} + MX_{\mathrm{CG}}}{m_{\mathrm{WC}}}$$
$$y_{\mathrm{WC2}} = \frac{m_{\mathrm{platform}} y_{\mathrm{p2}} + MY_{\mathrm{CG}}}{m_{\mathrm{WC}}} \tag{85}$$

or, if $X_{\mathrm{CG}} \approx Y_{\mathrm{CG}} \approx 0$, which was the goal, we have the relation

$$x_{\mathrm{WC2}} = \frac{m_{\mathrm{platform}}}{m_{\mathrm{WC}}} x_{\mathrm{p2}}$$
$$y_{\mathrm{WC2}} = \frac{m_{\mathrm{platform}}}{m_{\mathrm{WC}}} y_{\mathrm{p2}} \tag{86}$$

Using the Parallel Axis Theorem from (19), we can solve for the desired moment of inertia of the wheelchair, $(I_{zz})_{\mathrm{WC}}$,

$$(I_{zz})_{\mathrm{WC}} = (I_{zz}^{\mathrm{O}})_{\mathrm{WC}} - m_{\mathrm{WC}} d_{\mathrm{WC2}}{}^2 \tag{87}$$

where

$$d_{\mathrm{WC2}}{}^2 = x_{\mathrm{WC2}}{}^2 + y_{\mathrm{WC2}}{}^2 \tag{88}$$

Now, all of the desired inertial parameters of the manual wheelchair have been determined, and the iMachine test procedure is complete.

CHAPTER 4

CALIBRATION

The purpose of this chapter is to detail the methods and results for calibrating the load cells and springs. By analyzing the factors that influence the inertia measurement, potential sources of error can be detected and addressed to increase the overall accuracy of the machine.

4.1 Load Cell Calibration

Each of the load cells was calibrated to accurately determine the scaling factor between the voltage output and the force input. The procedure involved adding known weights on top of the transducer and recording the voltage output. The range of weights that was tested is approximately 0-50 lbs (0-22.7 kg), and these values were acquired using a 0.05 lb-resolution scale. This means that the resolution-based uncertainty in the force measurement is 0.025 lb (0.01134 kg), which is 0.05% of the total range. Weights were incremented first, then decremented to check for hysteresis effects. Figure 31-Figure 33 plot the calibration results. The data has been fitted with a linear regression line that has a *y*-intercept set to zero. The slopes of the linear regression lines are summarized in Table 5, which lists the calibration factors for converting mV signals to kg. Converting to kg rather than N means that the measurement will be in mass rather than weight. This takes the acceleration due to gravity into account ahead of time.

Table 5. Load cell calibration factors

Load Cell ID	A	B	C
Cal. Factor	0.092	0.096	0.095

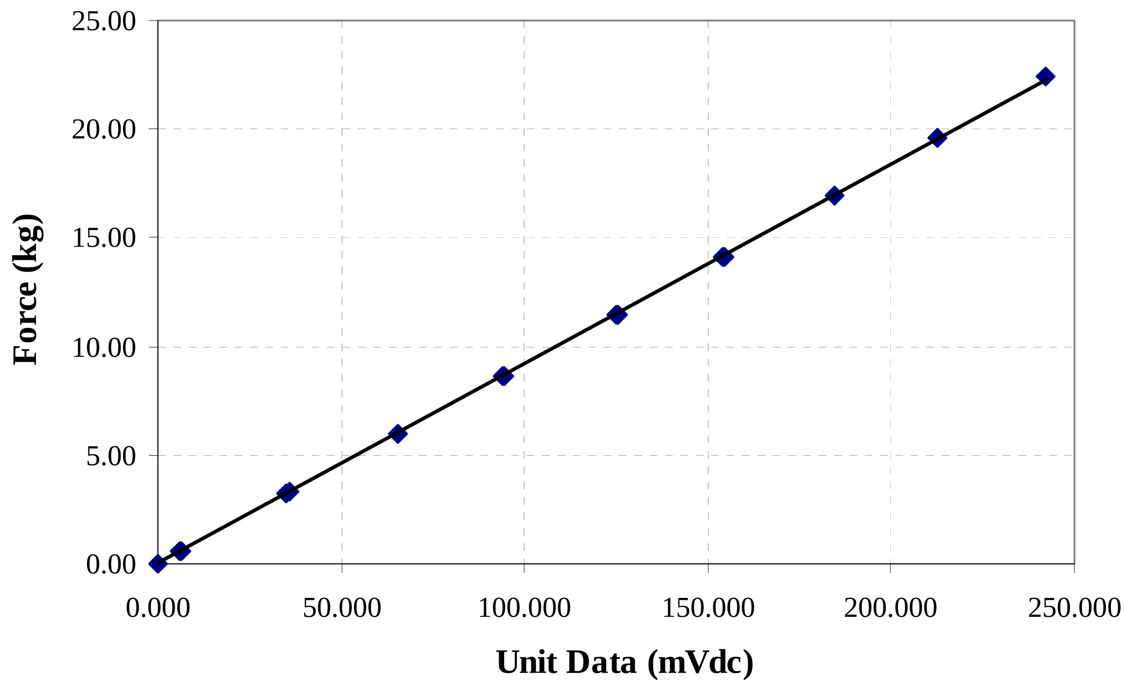

Figure 31. Load cell A calibration data

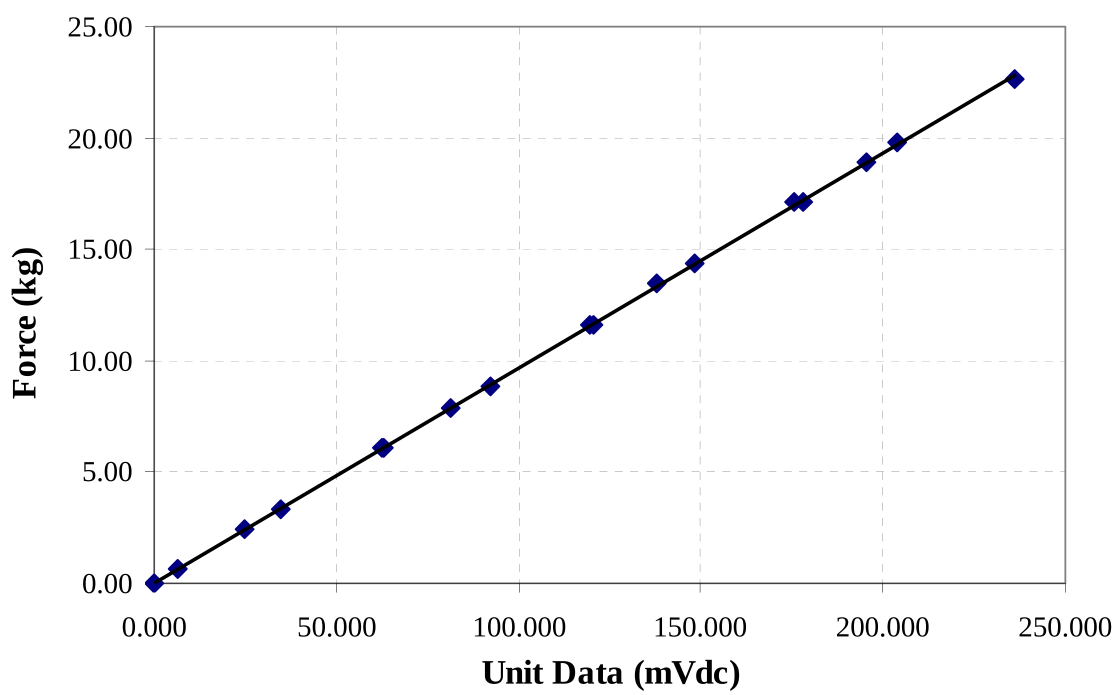

Figure 32. Load cell B calibration data

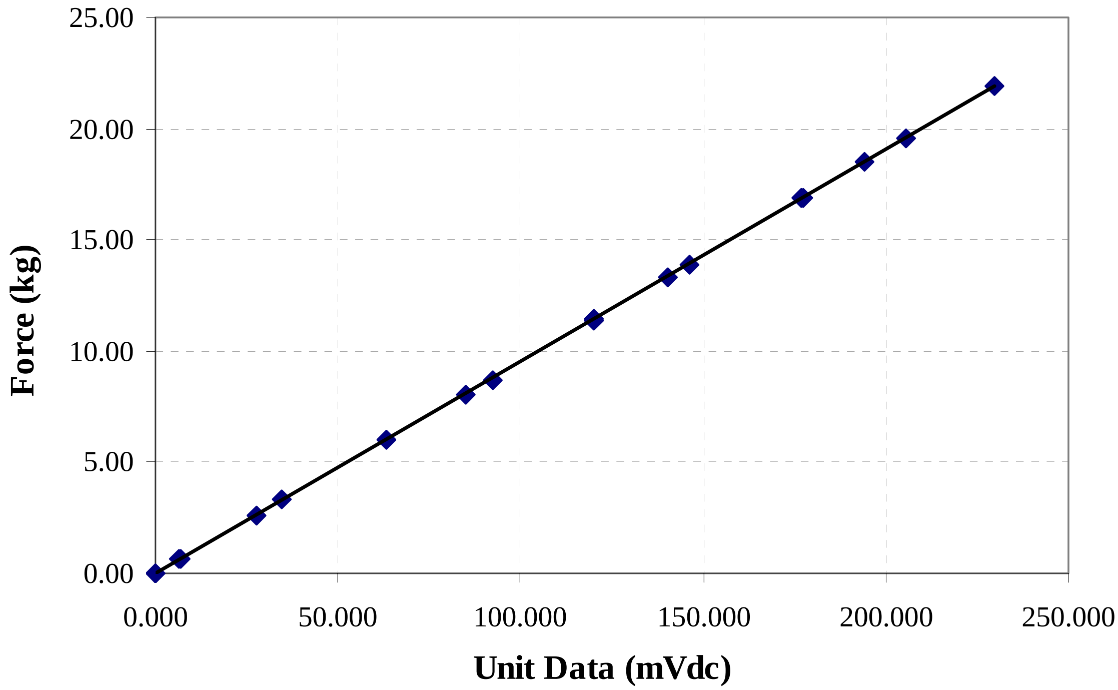

Figure 33. Load cell C calibration data

Clearly, the data is highly linear in all three cases, and the R^2 values are all greater than 0.999, so it is assumed that there is minimal error in the individual load cell measurements.

After running several tests, it is apparent that the DC offset in the transducer signals can vary slightly between runs. As a result, a tare control has been added to the LabVIEW GUI that instantaneously zeros the readings on all load cells. This should decrease the effect of an inconsistent voltage offset on the error in the measurement.

4.2 Spring Calibration

The spring calibration was performed *in situ* so that any uncertainty in the normal operation of the iMachine would be taken into account in the determination of the spring rate. To accomplish this test, two diametrically-opposed steel bricks were placed on the device as shown in Figure 34. Not shown in the figure are the X-Y platform and a wooden board, both of which are mounted to the disk. The platform is used to simulate actual testing conditions, and the board has marked dimensions to improve measurement accuracy. For simplicity, the inertia of the system excluding the bricks will be referred to as $\left(I_{zz}^{\mathrm{O}}\right)_{\mathrm{disk}}$ in the calibration analysis. Each brick has the mass and geometric properties listed in Table 6.

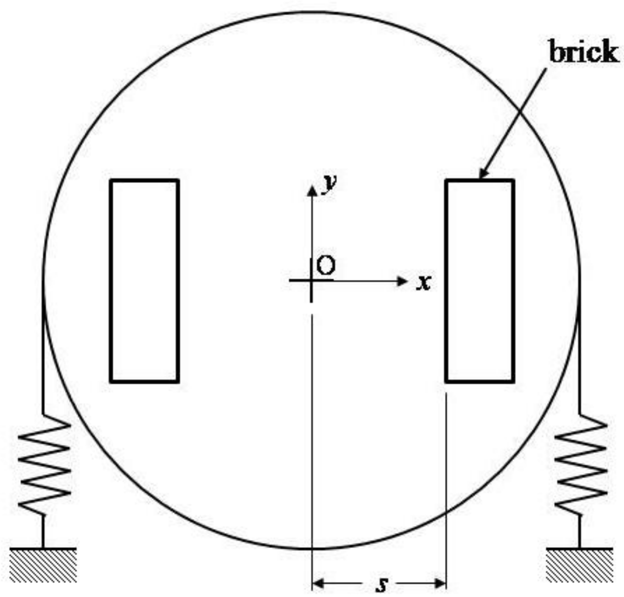

Figure 34. Model of spring calibration test

Table 6. Steel brick mass and geometric properties

Parameter	Symbol	Units	Value
mass	m_{brick}	kg	5.52
length	l	mm	242.96
width	w	mm	76.22
depth	d	mm	38.16

For the calculations performed in this calibration, the theoretical inertia of each brick about its CG is used according to the equation

$$\left(I_{zz}\right)_{\text{brick}} = \frac{m_{\text{brick}}}{12}\left(l^2 + w^2\right) \tag{89}$$

When the iMachine is run with the system in Figure 34, the measured moment of inertia corresponds to

$$\left(I_{zz}^{\text{O}}\right)_{\text{sys}} = \left(I_{zz}^{\text{O}}\right)_{\text{disk}} + 2\left(I_{zz}^{\text{O}}\right)_{\text{brick}} \tag{90}$$

where the inertia terms are about the *z*-axis passing through the origin. To relate the third term in (90) to the theoretical inertia of the brick in (89), use the parallel axis theorem as follows

$$\left(I_{zz}^{\text{O}}\right)_{\text{brick}} = \left(I_{zz}\right)_{\text{brick}} + m_{\text{brick}}\left(s + \frac{w}{2}\right)^2 \tag{91}$$

where s is the measured distance from the edge of the brick to the axis of rotation. The measured inertia can be related to the system dynamics by

$$\left(I_{zz}^{\text{O}}\right)_{\text{sys}} = \frac{k_{\text{eff}} R^2}{\omega_{\text{n}}^2} \tag{92}$$

where k_{eff} is the effective linear spring rate of the system and is equal to twice the spring rate of each individual spring. Substituting (89), (91), and (92) into (90) yields the following result,

$$\frac{k_{\text{eff}} R^2}{\omega_{\text{n}}^2} = \left(I_{zz}^{\text{O}}\right)_{\text{disk}} + 2\left[\frac{m_{\text{brick}}}{12}\left(l^2 + w^2\right) + m_{\text{brick}}\left(s + \frac{w}{2}\right)^2\right] \tag{93}$$

If the test is executed at two different distances, s_1 and s_2, then two natural frequencies arise, ω_1 and ω_2. Using the relationship established in (93), these parameters can be compared by taking the ratio

$$\frac{\omega_1^2}{\omega_2^2} = \frac{\left(I_{zz}^{\mathrm{O}}\right)_{\mathrm{disk}} + \frac{m_{\mathrm{brick}}}{6}\left(l^2 + w^2\right) + 2m_{\mathrm{brick}}\left(s_2 + \frac{w}{2}\right)^2}{\left(I_{zz}^{\mathrm{O}}\right)_{\mathrm{disk}} + \frac{m_{\mathrm{brick}}}{6}\left(l^2 + w^2\right) + 2m_{\mathrm{brick}}\left(s_1 + \frac{w}{2}\right)^2} \tag{94}$$

which, when rearranged, can be used to solve for the inertia of the disk as follows,

$$\left(I_{zz}^{\mathrm{O}}\right)_{\mathrm{disk}} = \frac{\frac{m_{\mathrm{brick}}}{6}\left(l^2 + w^2\right)\left(\omega_2^2 - \omega_1^2\right) + 2m_{\mathrm{brick}}\left(s_2 + \frac{w}{2}\right)^2 \omega_2^2 - 2m_{\mathrm{brick}}\left(s_1 + \frac{w}{2}\right)^2 \omega_1^2}{\left(\omega_1^2 - \omega_2^2\right)} \tag{95}$$

Once the disk inertia has been calculated, it can be substituted into (93) to solve for the effective spring rate.

For this calibration, the two distances that were tested are 50.8 mm (2 in) and 76.2 mm (3 in). Each distance was tested twenty times for reliability, and the natural frequency results for each of the four methods described in the previous chapter are listed in Table 7 and Table 8, where the columns “zero”, “maxima”, “minima”, and “fft” refer to determination of the natural frequency using zero crossings, time between consecutive maxima, time between consecutive minima, and peak FFT methods, respectively. The mean and standard deviation of these measurements is provided in Table 9. All of the natural frequency estimation methods appear to be very precise and repeatable, with the worst standard deviation equal to 0.00869 rad/s.

Table 7. Natural frequency (rad/s) based on time-domain and frequency-domain methods (s_1 = 50.8 mm)

run #	zero	maxima	minima	fft
1	5.569	5.546	5.558	5.536
2	5.546	5.532	5.532	5.519
3	5.529	5.514	5.521	5.508
4	5.545	5.537	5.533	5.517
5	5.546	5.531	5.535	5.519
6	5.545	5.536	5.533	5.515
7	5.543	5.532	5.525	5.517
8	5.552	5.535	5.535	5.518
9	5.551	5.537	5.532	5.517
10	5.548	5.539	5.542	5.519
11	5.542	5.532	5.526	5.517
12	5.555	5.547	5.539	5.527
13	5.548	5.535	5.532	5.519
14	5.553	5.542	5.536	5.522
15	5.546	5.528	5.532	5.518
16	5.554	5.542	5.543	5.521
17	5.566	5.556	5.548	5.531
18	5.553	5.537	5.543	5.521
19	5.552	5.536	5.534	5.522
20	5.538	5.534	5.531	5.517

Table 8. Natural frequency (rad/s) based on time-domain and frequency-domain methods (s_2 = 76.2 mm)

run #	zero	maxima	minima	fft
1	5.520	5.494	5.510	5.486
2	5.509	5.497	5.495	5.479
3	5.519	5.505	5.495	5.488
4	5.522	5.513	5.506	5.491
5	5.500	5.483	5.486	5.471
6	5.497	5.488	5.490	5.470
7	5.503	5.483	5.491	5.474
8	5.499	5.489	5.482	5.472
9	5.505	5.485	5.491	5.476
10	5.489	5.478	5.480	5.468
11	5.505	5.490	5.499	5.473
12	5.503	5.495	5.490	5.475
13	5.510	5.489	5.496	5.478
14	5.499	5.494	5.491	5.478
15	5.502	5.494	5.488	5.480
16	5.501	5.490	5.489	5.471
17	5.511	5.500	5.490	5.477
18	5.505	5.492	5.496	5.473
19	5.508	5.494	5.487	5.475
20	5.509	5.489	5.495	5.478

Table 9. Mean and standard deviation for natural frequency measurements

	zero	maxima	minima	fft
mean(s_1)	5.54904	5.5363	5.53551	5.519912
SD(s_1)	0.00869	0.00843	0.00835	0.005888
mean(s_2)	5.50581	5.49213	5.49241	5.476734
SD(s_2)	0.00807	0.00788	0.00705	0.005994

The average natural frequencies for each estimation method were used along with the brick properties found in Table 6 to solve for the inertia of the system in (95). The results are listed in Table 10.

Table 10. Moment of inertia of the disk system (kg-m^2)

zero	maxima	minima	fft
3.467	3.381	3.469	3.452

The values listed in the table above were substituted back into (93) along with the parameters already given to solve for the effective spring rate of the system, k_{eff}. The moment arm of the spring force, *R*, is equal to the radius of the disk, which is 0.29845 m (11.75 in). To maintain consistency, the effective spring rate was calculated four times for each test at both distances, one corresponding to each of the time-domain and frequency-domain techniques. Each natural frequency was paired with the disk inertia of the same method – that is, only the natural frequencies that were calculated via FFT use the disk inertia that was calculated via FFT. The effective spring rates are shown in Table 11 and Table 12, and the statistical mean and standard deviation appear in Table 13.

Table 11. Effective spring rate (N/m) based on time-domain and frequency-domain methods (s_1 = 50.8 mm)

run #	zero	maxima	minima	fft
1	1258.28	1218.33	1253.78	1238.05
2	1248.04	1212.24	1242.18	1230.48
3	1240.47	1204.27	1237.25	1225.84
4	1247.68	1214.11	1242.55	1229.65
5	1247.98	1211.65	1243.57	1230.89
6	1247.54	1213.77	1242.72	1228.82
7	1246.66	1212.18	1239.20	1229.64
8	1250.68	1213.47	1243.62	1230.09
9	1250.40	1214.27	1242.12	1229.68
10	1249.10	1215.20	1246.66	1230.90
11	1246.42	1212.03	1239.32	1229.64
12	1251.92	1218.60	1245.55	1234.24
13	1248.82	1213.24	1242.05	1230.47
14	1251.16	1216.36	1243.80	1232.15
15	1248.00	1210.18	1242.31	1230.02
16	1251.56	1216.60	1247.20	1231.74
17	1256.99	1222.87	1249.58	1235.95
18	1251.30	1214.19	1247.04	1231.74
19	1250.63	1213.91	1243.30	1232.15
20	1244.51	1212.89	1241.79	1229.61

Table 12. Effective spring rate (N/m) based on time-domain and frequency-domain methods (s_2 = 76.2 mm)

run #	zero	maxima	minima	fft
1	1255.72	1214.89	1251.66	1235.09
2	1250.76	1216.06	1244.85	1232.06
3	1255.52	1219.81	1244.98	1236.30
4	1256.74	1223.28	1250.02	1237.57
5	1246.72	1209.94	1241.04	1228.29
6	1245.33	1212.29	1242.67	1228.27
7	1248.19	1210.08	1243.17	1229.97
8	1246.16	1212.49	1239.01	1229.11
9	1248.90	1210.75	1243.10	1230.81
10	1241.84	1207.82	1238.39	1226.99
11	1249.25	1213.11	1246.67	1229.59
12	1248.05	1215.34	1242.85	1230.37
13	1251.47	1212.62	1245.32	1231.66
14	1246.51	1214.92	1242.96	1231.63
15	1247.83	1214.78	1241.99	1232.49
16	1247.40	1213.10	1242.16	1228.71
17	1251.63	1217.29	1242.85	1231.24
18	1249.03	1214.11	1245.45	1229.55
19	1250.24	1215.01	1241.41	1230.43
20	1250.85	1212.66	1245.06	1231.66

Table 13. Mean and standard deviation (N/m) for k_{eff} measurements

	zero	maxima	minima	fft
mean(s_1)	1249.407	1214.018	1243.78	1231.087
SD(s_1)	3.9144	3.69623	3.756386	2.627633
mean(s_2)	1249.406	1214.017	1243.78	1231.088
SD(s_2)	3.664118	3.487711	3.194249	2.696008

To understand these results, it is necessary to compare the spring rate to that provided by the manufacturer. A summary of the comparison, including relative percent error estimates, is given in Table 14. It is difficult to draw conclusions regarding the accuracy of the calibrated results, but they are relatively close to the data given by the manufacturer, which is expected. Validation tests are needed to examine the effect of the calibrated spring rate on the accuracy of the moment of inertia measurement, and the results of these tests will be presented in the next chapter.

Table 14. Comparison of calibrated spring rate to manufacturer-provided data

	k (lb/in)	k (N/m)	k_{eff} (N/m)	% error
zero	3.57	624.70	1249.41	6.17
maxima	3.47	607.01	1214.02	3.16
minima	3.55	621.89	1243.78	5.69
fft	3.51	615.54	1231.09	4.61
mfr.	3.36	588.43	1176.85	-

CHAPTER 5

TESTING AND RESULTS

This chapter begins with an analysis of validation tests for each of the inertial parameter measurements. For each parameter, objects with known mass properties were tested and the empirical results are compared to the theoretical predictions using closed-form formulas. Then, a manual wheelchair was tested and the inertia measurement juxtaposed against the previous test results. Conclusions regarding the accuracy and reliability of results as well as a discussion of potential sources of error are presented in the following chapter.

5.1 Mass Validation

Now that the load cells have been calibrated individually, the next step is to check the accuracy of the mass measurement when all three load cells are working as a system. To achieve this goal, comparisons were made between the measurements of the load cells and a commercially-available scale. The scale has a resolution of 0.02 lb, making the resolution-based uncertainty 0.01 lb. The platform was weighed beforehand and its mass is 19.00 kg. Then, the load cells and platform were mounted to the disk. Next, the mass was monitored according to the load cell readings, and known weights were added incrementally. The data is presented below in Table 15. The error equations are given by

$$e_{\text{abs}} = q_{\text{measured}} - q_{\text{actual}} \tag{96}$$

$$e_{\text{rel}} = \left| \frac{q_{\text{measured}} - q_{\text{actual}}}{q_{\text{actual}}} \right| (100\%) \tag{97}$$

where e_{abs} is the absolute error, e_{rel} is the relative percent error, $q_{measured}$ is the measured data parameter, and q_{actual} is the actual data parameter. In this case, the parameter is the mass, and the actual value refers to the scale reading.

Table 15. Accuracy of load cell mass measurement

Scale (kg)	Load Cells (kg)	Absolute Error (kg)	Percent Error (%)
19.00	19.07	0.07	0.368
19.90	19.90	0.00	0.000
20.80	20.90	0.10	0.481
21.70	21.98	0.28	1.290
22.60	22.86	0.26	1.150
24.50	24.69	0.19	0.776
25.40	25.57	0.17	0.669
26.30	26.63	0.33	1.255
27.20	27.53	0.33	1.213
28.10	28.33	0.23	0.819
29.98	30.09	0.11	0.367
30.88	31.01	0.13	0.421
31.78	31.97	0.19	0.598
32.68	32.90	0.22	0.673
33.58	33.83	0.25	0.744
35.50	35.90	0.40	1.127
36.40	36.80	0.40	1.099
37.30	37.61	0.31	0.831
38.20	38.52	0.32	0.838
39.10	39.38	0.28	0.716
41.00	41.28	0.28	0.683
41.90	42.23	0.33	0.788
42.80	43.08	0.28	0.654
43.70	44.04	0.34	0.778
44.60	44.92	0.32	0.717
	AVERAGE	0.24	0.762

The data looks fairly good, with an average relative accuracy of 99.24%. The absolute error ranges from 0.00-0.40 kg, and the load cell measurement is always higher than the predicted scale value. During the test, it was noted that the load cell mass reading varied depending on where the mass was located. The weights were placed arbitrarily during the test, but perhaps a more calculated strategy could shed light on the relationship between mass position and the associated error.

To investigate this hypothesis, the platform was set in a symmetric configuration so that the CG measured to be approximately zero. A small mass was placed at different locations on the platform and the mass recorded. Figure 35 shows the different configurations used, with each number identifying a position of the small mass.

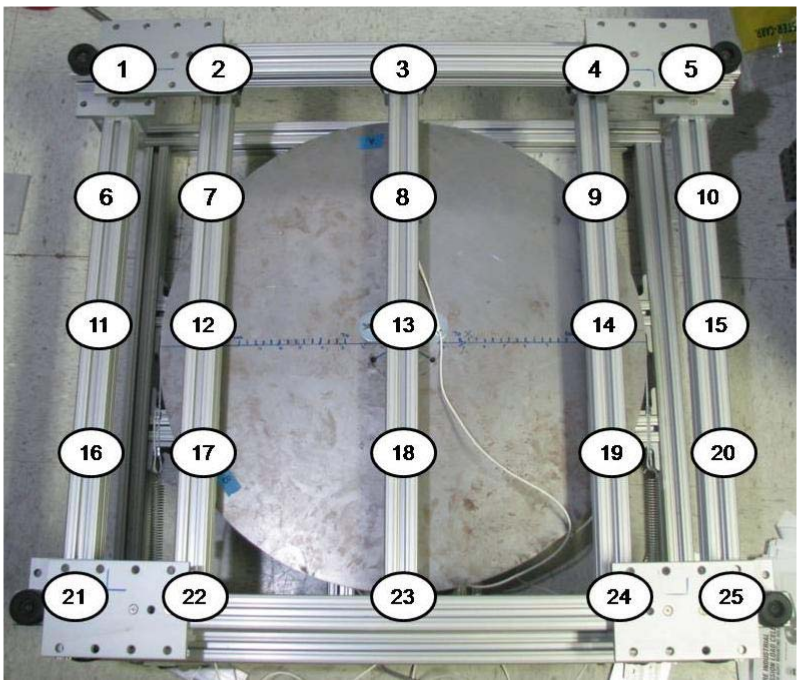

Figure 35. Platform configurations for mass validation test

The actual mass value is 20.12 kg for this test, and the results are presented in Table 16. The range of absolute error for this test is 0.11 kg, which equates to 0.547% of the expected value. This is an encouraging result; the maximum relative percent error is 0.348%, and all configurations provide accuracy of greater than 99.6%.

Table 16. Error in mass readings due to position on platform (20.12 kg mass)

Configuration	Measured Value (kg)	Absolute Error (kg)	Relative Error (%)
1	20.09	-0.03	0.149
2	20.08	-0.04	0.199
3	20.09	-0.03	0.149
4	20.12	0.00	0.000
5	20.13	0.01	0.050
6	20.08	-0.04	0.199
7	20.09	-0.03	0.149
8	20.11	-0.01	0.050
9	20.12	0.00	0.000
10	20.11	-0.01	0.050
11	20.09	-0.03	0.149
12	20.10	-0.02	0.099
13	20.14	0.02	0.099
14	20.12	0.00	0.000
15	20.13	0.01	0.050
16	20.14	0.02	0.099
17	20.14	0.02	0.099
18	20.15	0.03	0.149
19	20.14	0.02	0.099
20	20.13	0.01	0.050
21	20.18	0.06	0.298
22	20.19	0.07	0.348
23	20.18	0.06	0.298
24	20.15	0.03	0.149
25	20.13	0.01	0.050
	AVERAGE	0.01	0.121

To understand how the error changes based on the position of the mass on the platform, Figure 36 illustrates an interpolated surface plot of the absolute error distribution across the platform dimensions. The most accurate measurements occur in Quadrant II, while the worst occur in Quadrant I. To see if the amount of mass in these positions affects the error, the test was repeated using heavier weights. The actual mass value is 24.73 kg, and the results are listed in Table 17.

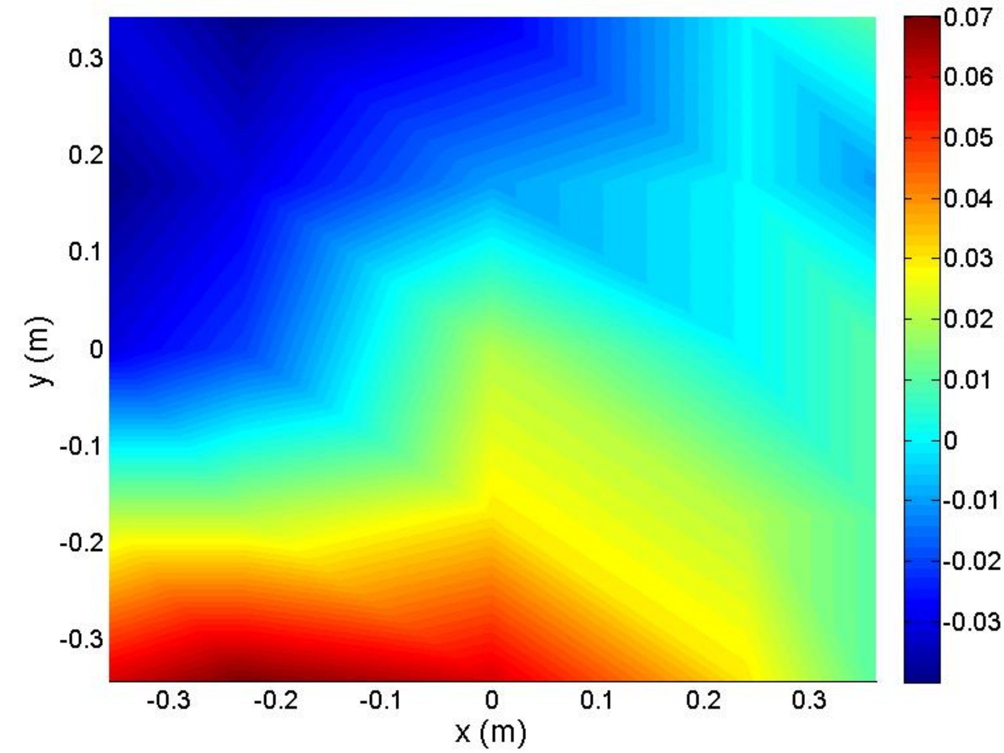

Figure 36. Interpolated surface plot of absolute error distribution (in kg) on platform (20.12 kg mass)

Table 17. Error in mass readings due to position on platform (24.73 kg mass)

Configuration	Measured Value (kg)	Absolute Error (kg)	Relative Error (%)
1	24.40	-0.33	1.334
2	24.42	-0.31	1.254
3	24.47	-0.26	1.051
4	24.59	-0.14	0.566
5	24.57	-0.16	0.647
6	24.51	-0.22	0.890
7	24.54	-0.19	0.768
8	24.60	-0.13	0.526
9	24.71	-0.02	0.081
10	24.74	0.01	0.040
11	24.67	-0.06	0.243
12	24.66	-0.07	0.283
13	24.74	0.01	0.040
14	24.83	0.10	0.404
15	24.82	0.09	0.364
16	24.81	0.08	0.323
17	24.85	0.12	0.485
18	24.90	0.17	0.687
19	24.86	0.13	0.526
20	24.85	0.12	0.485
21	24.92	0.19	0.768
22	24.97	0.24	0.970
23	24.97	0.24	0.970
24	24.95	0.22	0.890
25	24.95	0.22	0.890
	AVERAGE	0.0020	0.619

In this case, the range of absolute error is 0.57 kg, which equates to 2.305% of the expected value. Most configurations are greater than 99% with the maximum relative percent error for the data set being 1.334%. These results are slightly higher in error than the previous test, which begs the question of whether the relative percent error increases with increasing mass. Figure 37 displays the surface plot of the interpolated absolute error for the test with a larger mass. The distribution is fairly similar to Figure 36, and still indicates that placing the mass in Quadrant II produces the greatest accuracy.

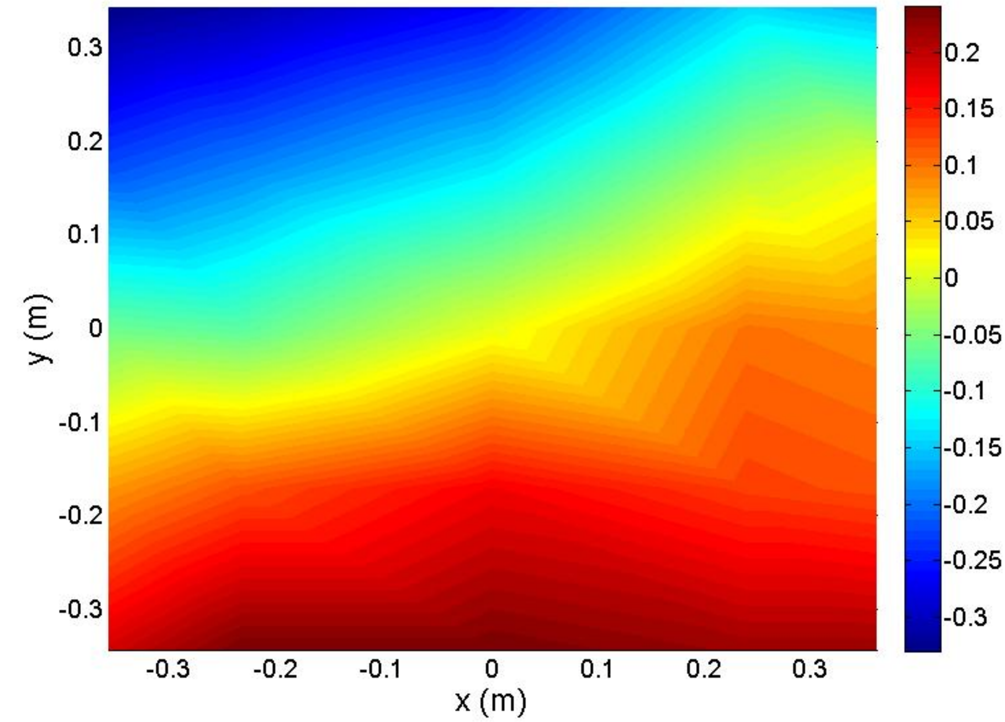

Figure 37. Interpolated surface plot of absolute error distribution (in kg) on platform (24.73 kg mass)

There are many possible reasons for the error trend in Figure 37. One explanation is poor calibration of the load cells, specifically B and C, since the error tends to get worse as the mass is moved closer to them. However, the previous calibration results exhibit high correlation and do not reflect the inaccuracy expected if this were the cause of error. Another potential explanation of the error trend is that something in the structural design is altering the load seen by the transducers. The only interface between the platform and the disk other than the load cells is the stability rods to prevent lateral motion. If binding occurs between the rods and the copper bearings, the rods will support some of the load. However, this should cause the load cells to underestimate the mass, which is not the case for most of the error. Whatever the cause, the error is sufficiently small for this measurement and most of the mass tested on the iMachine will not be concentrated in the red regions of the previous figure.

5.2 Center of Mass Validation

A static test was performed to determine the error in the calculation of the center of mass. The test object was a stack of steel blocks, weighing 16.53 kg. A wooden board with marked distances from the center along the *x* and *y* coordinate axes was situated on the platform in a configuration that placed the system CG at the origin of the disk. Then, the centroid of the test object, determined theoretically using closed-form equations, was lined up with the board markings. The actual coordinates of the object's CG were recorded according to the board. To calculate the measured CG coordinates of the object, it is necessary to recall that the load cell-based CG measurement includes the weight of the system including both the test object and the platform. To illustrate this concept, consider the diagram shown in Figure 38.

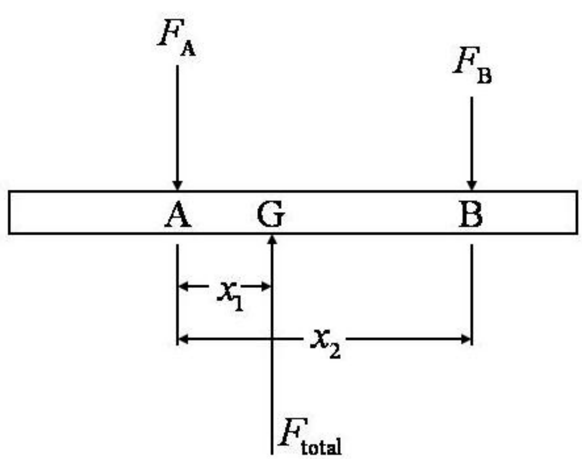

Figure 38. Static analysis of forces on iMachine platform

Summing the moments about point A and assuming static equilibrium,

$$\sum M_{\mathrm{A}} = 0: \quad F_{\mathrm{B}} x_2 = F_{\mathrm{total}} x_1 \tag{98}$$

where the total force is equal to the sum of F_{A} and F_{B}. Solving for the moment-arm of the force at point B,

$$x_2 = \frac{\left(F_{\mathrm{A}} + F_{\mathrm{B}}\right)}{F_{\mathrm{B}}} x_1 = F_{\mathrm{ratio}} x_1 \tag{99}$$

Similarly, for the *y*-coordinate,

$$y_2 = \frac{\left(F_{\mathrm{A}} + F_{\mathrm{B}}\right)}{F_{\mathrm{B}}} y_1 = F_{\mathrm{ratio}} y_1 \tag{100}$$

Now, in the given problem, the force acting at B is the weight of the test object, while the force acting at A is due to the platform. The total force acting at G, which corresponds to the system CG, is the reaction force output by the load cells. The location of the test object CG corresponds to $\left(x_2, y_2\right)$.

For this test, the distance from the axis of rotation to the edge of the test object was varied between 10 mm and 150 mm in 20 mm-increments. Note that, by dividing the numerator and denominator in (99) and (100) by the acceleration due to gravity, the force ratio can be written in terms of masses, which is what the iMachine measures. The ratio was found empirically by recording the mass measurement before and after loading the test object on the platform, and plugging the appropriate values into (99) and (100). The test data is summarized in Table 18. Using the same methods as the mass measurement validation test, the mass relative error is 0.961% for this test. The percent error for both coordinates was calculated using equation (97).

Table 18. Center of mass validation test results

x_actual (m)	y_actual (m)	x_CG (m)	y_CG (m)	F_ratio	x_meas (m)	y_meas (m)	%error_x	%error_y
0.0000	0.0483	-0.000757	0.020000	2.37133	-0.001795	0.047427	-	1.8082
0.0000	0.0683	-0.001277	0.028000	2.37717	-0.003037	0.066561	-	2.5466
0.0000	0.0883	-0.001128	0.036190	2.38262	-0.002688	0.086226	-	2.3488
0.0000	0.1083	-0.001212	0.044531	2.38217	-0.002887	0.106080	-	2.0503
0.0000	0.1283	-0.001302	0.052573	2.38676	-0.003108	0.125479	-	2.1991
0.0000	0.1483	-0.001024	0.061049	2.38594	-0.002444	0.145659	-	1.7810
0.0000	0.1683	-0.001310	0.069438	2.38837	-0.003129	0.165843	-	1.4596
0.0000	0.1883	-0.001371	0.077877	2.39380	-0.003282	0.186421	-	0.9979
0.0483	0.0000	0.019865	-0.001781	2.36208	0.046923	-0.004207	2.8506	-
0.0683	0.0000	0.028609	-0.001692	2.36057	0.067533	-0.003995	1.1228	-
0.0883	0.0000	0.037394	-0.001870	2.34533	0.087701	-0.004385	0.6780	-
0.1083	0.0000	0.045868	-0.001805	2.34093	0.107375	-0.004226	0.8543	-
0.1283	0.0000	0.054552	-0.001792	2.34118	0.127716	-0.004196	0.4552	-
0.1483	0.0000	0.063306	-0.001986	2.34127	0.148217	-0.004649	0.0563	-
0.1683	0.0000	0.071508	-0.002133	2.34517	0.167698	-0.005001	0.3578	-
0.1883	0.0000	0.079853	-0.002484	2.34026	0.186877	-0.005814	0.7559	-

Initially, the average error for the *x* and *y*-coordinates was 0.891% and 3.643%, respectively. The greatest error occurred when the object CG was near the origin, which is somewhat expected since the instrument resolution has the most effect when the terms in the numerator of (69) are approximately equal. Nonetheless, significant error near the origin is unacceptable since the iMachine test method involves an attempt to drive the CG coordinates to zero. However, upon retesting at distances in the *y*-direction of 10 mm and 30 mm (first two rows in the table), the percent error reduced to 1.808% and 2.547%, respectively, and these are the values that are shown in Table 18. This test was repeated multiple times with consistent results, so it is assumed that the original results for these cases were outliers and can be neglected. Therein, the new average error in the calculation of *y*-coordinate of the center of mass is 1.99%.

5.3 Moment of Inertia Validation

To validate the moment of inertia measurement, tests are run on objects with known mass properties, and comparisons are made between the theoretical inertia predictions and empirical results. The first test object is the same steel brick used during the spring calibration test, so refer to Table 6 for the mass and geometric properties. The theoretical inertia can be determined by the equation

$$I_{\text{theoretical}} = \frac{m}{12}\left(l^2 + w^2\right) \tag{101}$$

which, when plugging in the values from Table 6, results in $I_{\text{theoretical}} = 29826 \text{ kg} \cdot \text{mm}^2$.

The iMachine was run thirty times with and without the brick centered on the platform. Figure 38 and Figure 39 display the time-domain and frequency-domain response of the system, respectively, for one of the test runs.

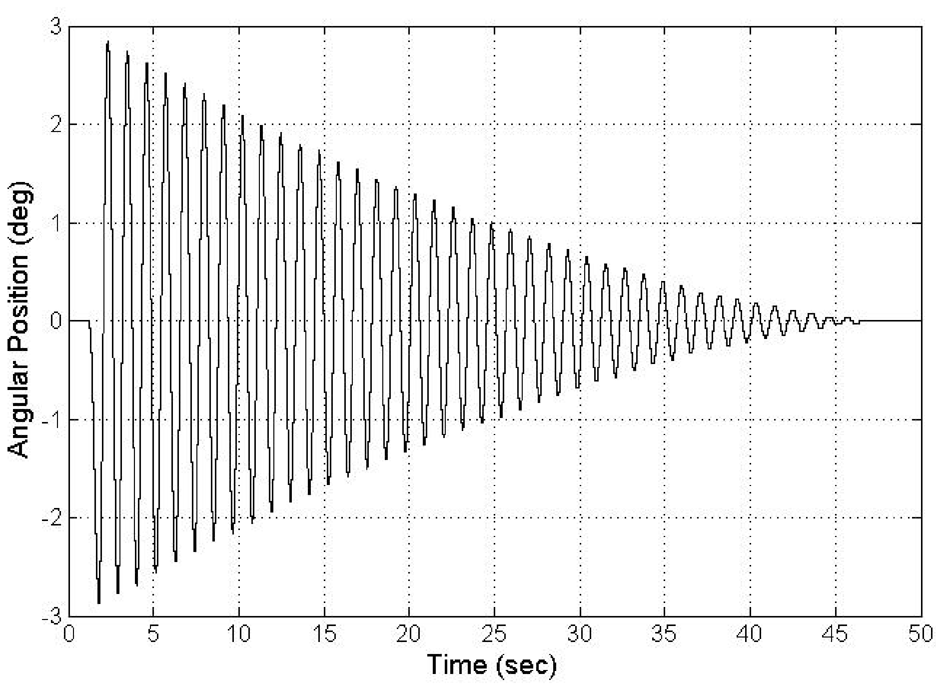

Figure 39. Time-domain response of iMachine validation test (1 block)

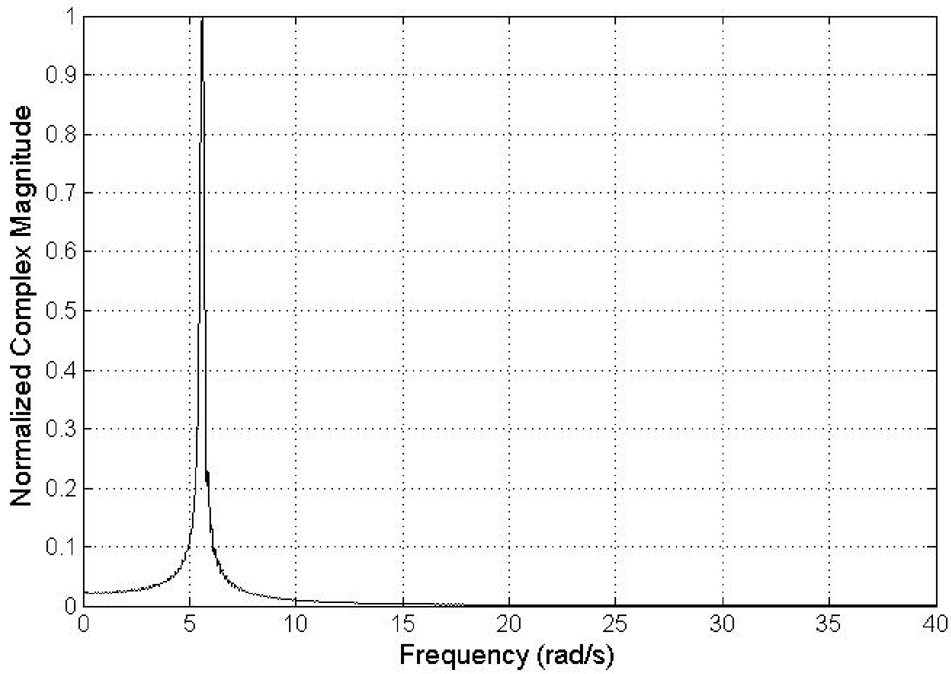

Figure 40. Frequency-domain response of iMachine validation test (1 block)

It is clear from both figures that the system is lightly damped. To quantify the damping in the time domain, the log decrement was used. For each run with *N* peaks, (*N-1*) damping ratios were computed by comparing the 1st peak to the *i*th peak, where *i* varies from 2 to *N*. The mean value was computed for each run, and the average of the mean across all tests was 0.0092. To quantify the damping in the frequency domain, the half-power strategy given in (77) and (78) was used. The average peak frequency based on the FFT is 5.600 rad/s, and the narrow bandwidth yields damping ratios of approximately 1-2%. Therefore, for both time-domain and frequency-domain methods, it is sufficient to assume that the damped natural frequency is approximately equal to the natural frequency of the system. This frequency was calculated using all four of the techniques outlined in the Measurement Approach chapter, and the results for each validation test run are presented in Table 19. Table 20 summarizes these parameters for the case when the brick was removed from the system.

Table 19. Mass properties and natural frequency for iMachine validation test (one brick) with brick on platform

	Mass (kg)	Center of mass (m)		Natural frequency (rad/s)			
run#	m_{sys}	X_{CG}	Y_{CG}	zero	maxima	minima	fft
1	28.3455	0.0002	-0.0002	5.6298	5.6159	5.6233	5.6005
2	28.3494	0.0003	0.0001	5.6289	5.6116	5.6192	5.6080
3	28.3467	0.0002	0.0000	5.6258	5.6185	5.6209	5.6015
4	28.3583	0.0002	0.0001	5.6422	5.6257	5.6333	5.6136
5	28.3553	0.0002	-0.0001	5.6065	5.5968	5.5991	5.5918
6	28.3539	0.0002	0.0000	5.6108	5.6094	5.5996	5.6011
7	28.3504	0.0002	0.0000	5.6268	5.6150	5.6104	5.5968
8	28.3580	0.0002	0.0000	5.6042	5.5961	5.5992	5.5891
9	28.3531	0.0003	-0.0001	5.5924	5.5882	5.5864	5.5852
10	28.3775	0.0001	-0.0003	5.6000	5.5911	5.5988	5.5926
11	28.3687	0.0003	-0.0001	5.6553	5.6449	5.6371	5.6249
12	28.3790	0.0002	-0.0001	5.6257	5.6189	5.6095	5.5968
13	28.3715	0.0002	-0.0002	5.6288	5.6205	5.6143	5.5987
14	28.3651	0.0002	-0.0002	5.6243	5.6113	5.6197	5.5968
15	28.3845	0.0001	0.0000	5.6245	5.6113	5.6177	5.6005
16	28.3625	0.0002	-0.0002	5.6314	5.6192	5.6120	5.6015
17	28.3665	0.0002	-0.0001	5.6327	5.6121	5.6264	5.6043
18	28.3647	0.0002	-0.0002	5.6241	5.6169	5.6113	5.5996
19	28.3574	0.0003	0.0000	5.6067	5.5993	5.6068	5.5946
20	28.3626	0.0002	-0.0002	5.6315	5.6185	5.6158	5.6024
21	28.3542	0.0002	-0.0002	5.6311	5.6196	5.6168	5.6005
22	28.3646	0.0002	0.0000	5.6089	5.5989	5.6008	5.5955
23	28.3617	0.0002	-0.0001	5.6306	5.6143	5.6199	5.6024
24	28.3507	0.0003	-0.0002	5.6353	5.6153	5.6199	5.6052
25	28.3638	0.0002	-0.0002	5.6357	5.6242	5.6244	5.6089
26	28.3816	0.0002	-0.0001	5.6061	5.5947	5.6012	5.5964
27	28.3718	0.0002	0.0000	5.6036	5.5982	5.5935	5.5954
28	28.3612	0.0003	-0.0002	5.6007	5.5974	5.5956	5.5926
29	28.3649	0.0003	-0.0001	5.6299	5.6165	5.6139	5.6042
30	28.3691	0.0002	-0.0001	5.6134	5.6014	5.6014	5.5993
MEAN	28.36247	0.000219	-0.00011	5.62159	5.61072	5.61161	5.60003
STD.DEV	0.010136	0.00005	0.00008	0.0146	0.01233	0.01215	0.00757

Table 20. Mass properties and natural frequency for iMachine validation test (one brick) without brick on platform

	Mass (kg)	Center of mass (m)		Natural frequency (rad/s)			
run#	$m_{platform}$	$x_{platform}$	$y_{platform}$	zero	maxima	minima	fft
1	22.8246	0.0009	0.0000	5.6294	5.6192	5.6275	5.6155
2	22.8197	0.0011	0.0000	5.6493	5.6417	5.6363	5.6231
3	22.8323	0.0010	0.0000	5.6488	5.6359	5.6419	5.6212
4	22.8257	0.0009	-0.0001	5.6583	5.6423	5.6440	5.6297
5	22.8265	0.0009	-0.0001	5.6574	5.6425	5.6471	5.6278
6	22.8316	0.0009	0.0000	5.6569	5.6464	5.6462	5.6297
7	22.8228	0.0009	-0.0001	5.6592	5.6501	5.6500	5.6334
8	22.8216	0.0010	-0.0001	5.6633	5.6500	5.6533	5.6326
9	22.8240	0.0010	0.0000	5.6597	5.6397	5.6420	5.6325
10	22.8126	0.0009	-0.0001	5.6646	5.6519	5.6571	5.6326
11	22.8229	0.0009	0.0000	5.6434	5.6327	5.6371	5.6276
12	22.8190	0.0009	-0.0001	5.6503	5.6362	5.6420	5.6231
13	22.8165	0.0009	-0.0001	5.6544	5.6400	5.6379	5.6297
14	22.8118	0.0008	-0.0001	5.6520	5.6477	5.6383	5.6278
15	22.8211	0.0009	0.0000	5.6445	5.6347	5.6355	5.6286
16	22.8260	0.0010	-0.0002	5.6526	5.6444	5.6416	5.6241
17	22.8133	0.0009	-0.0002	5.6486	5.6428	5.6366	5.6269
18	22.8241	0.0009	0.0000	5.6594	5.6441	5.6399	5.6325
19	22.8290	0.0010	0.0001	5.6612	5.6460	5.6392	5.6335
20	22.8158	0.0010	-0.0001	5.6564	5.6422	5.6436	5.6307
21	22.8087	0.0008	-0.0002	5.6581	5.6395	5.6457	5.6343
22	22.8238	0.0007	-0.0002	5.6528	5.6339	5.6373	5.6250
23	22.8206	0.0007	-0.0002	5.6579	5.6391	5.6507	5.6316
24	22.8264	0.0007	0.0000	5.6609	5.6538	5.6499	5.6372
25	22.8275	0.0007	0.0001	5.6581	5.6471	5.6510	5.6306
26	22.8120	0.0007	-0.0002	5.6655	5.6551	5.6549	5.6363
27	22.8170	0.0007	-0.0002	5.6773	5.6513	5.6507	5.6448
28	22.8156	0.0007	-0.0002	5.6619	5.6500	5.6484	5.6316
29	22.8353	0.0007	-0.0002	5.6570	5.6458	5.6449	5.6306
30	22.8259	0.0006	-0.0001	5.6620	5.6494	5.6466	5.6316
MEAN	22.8218	0.000866	-0.0001	5.65604	5.64318	5.64391	5.62987
STD.DEV	0.006581	0.000121	0.0001	0.00846	0.00753	0.00671	0.00543

The measurements exhibit good repeatability, and the natural frequencies are very similar across estimation methods. As expected, the mass of the system decreases and the natural frequency increases when the brick is removed from the platform. To calculate the mass of the brick, subtract the average mass in Table 20 from the average mass in Table 19 according to (66). As a result, m_{brick} equals 5.541 kg for this test, which has 0.375% relative error compared to the measured value using a scale. The next step is to determine the CG coordinates of the test object with respect to the origin of the disk using equation (85). Substituting the average values from the tables above, the x and y-coordinates are 4.688 mm and -0.880 mm, respectively. This means the radial distance from the brick CG to the axis of rotation is 4.77 mm. The inertia of the system about the axis passing through the origin of the disk is calculated using the average natural frequencies in Table 19 along with the manufacturer-provided and calibrated spring rates. The same is done for the platform data in Table 20, and the results are shown in Table 21 and Table 22. To find the inertia of the brick about the origin of the disk, simply take the difference between the inertia of the system and that of the platform. The results are shown in Table 23. Taking into account the parallel axis term due to the brick CG coordinates being nonzero, the inertia of the brick about its CG is computed and listed in Table 24.

Table 21. Validation test (one brick): inertia of the system about the disk origin (kg-m^2)

		Effective Spring Rate Method				
		mfr	zero	maxima	minima	fft
Natural Frequency Estimation Method	zero	3.3170	3.5215	3.4218	3.5057	3.4699
	maxima	3.3299	3.5352	3.4350	3.5192	3.4833
	minima	3.3288	3.5340	3.4339	3.5181	3.4822
	fft	3.3426	3.5487	3.4482	3.5327	3.4967

Table 22. Validation test (one brick): inertia of the platform about the disk origin (kg-m^2)

		Effective Spring Rate Method				
		mfr	zero	maxima	minima	fft
Natural Frequency Estimation Method	zero	3.2767	3.4787	3.3802	3.4631	3.4277
	maxima	3.2917	3.4946	3.3956	3.4789	3.4434
	minima	3.2908	3.4937	3.3948	3.4780	3.4425
	fft	3.3073	3.5112	3.4117	3.4953	3.4597

Table 23. Validation test (one brick): inertia of the brick about the disk origin (kg-m^2)

		Effective Spring Rate Method				
		mfr	zero	maxima	minima	fft
Natural Frequency Estimation Method	zero	0.0403	0.0428	0.0416	0.0426	0.0421
	maxima	0.0382	0.0405	0.0394	0.0404	0.0400
	minima	0.0380	0.0403	0.0392	0.0401	0.0397
	fft	0.0353	0.0375	0.0365	0.0373	0.0370

Table 24. Validation test (one brick): inertia of the brick about its CG (kg-m^2)

		Effective Spring Rate Method				
		mfr	zero	maxima	minima	fft
Natural Frequency Estimation Method	zero	0.0402	0.0426	0.0414	0.0425	0.0420
	maxima	0.0381	0.0404	0.0393	0.0402	0.0398
	minima	0.0379	0.0402	0.0391	0.0400	0.0396
	fft	0.0352	0.0374	0.0363	0.0372	0.0368

It is clear from a comparison of Table 23 and Table 24 that the CG offset has little effect on its inertia. The relative percent error of each inertia value in Table 24 with respect to the theoretical inertia derived in (101) is tabulated in Table 25.

Table 25. Validation test (one brick): relative error of test object inertia (%)

		Effective Spring Rate Method				
		mfr	zero	maxima	minima	fft
Natural Frequency Estimation Method	zero	34.6545	42.9829	38.9209	42.3367	40.8801
	maxima	27.6219	35.5167	31.6661	34.9041	33.5234
	minima	26.9380	34.7905	30.9606	34.1812	32.8079
	fft	18.0635	25.3688	21.8058	24.8020	23.5244

Clearly, these results are unacceptable due to the large amount of error. The FFT natural frequency estimation method appears to have the most favorable results, with a minimum error of 18.0635% using the manufacturer-provided spring rate. While there may be systematic errors in the system due to resolution-based uncertainty in the measurement instruments, the large amount of error in this test is probably just an indication of the overall inertia resolution of the device. To understand this concept, consider that the total inertia of the brick from Table 23 is approximately 1% of the total system inertia. Therefore, this validation test does not show that the iMachine is incapable of measuring inertia accurately, but rather that it cannot effectively measure an inertia *change* of 1% or less.

In order to explore the accuracy of the inertia measurement further, the inertia of the test object was increased by adding four bricks in the square configuration shown in

Figure 41. The platform and wooden board are not pictured as before, but are used in practice for this particular test.

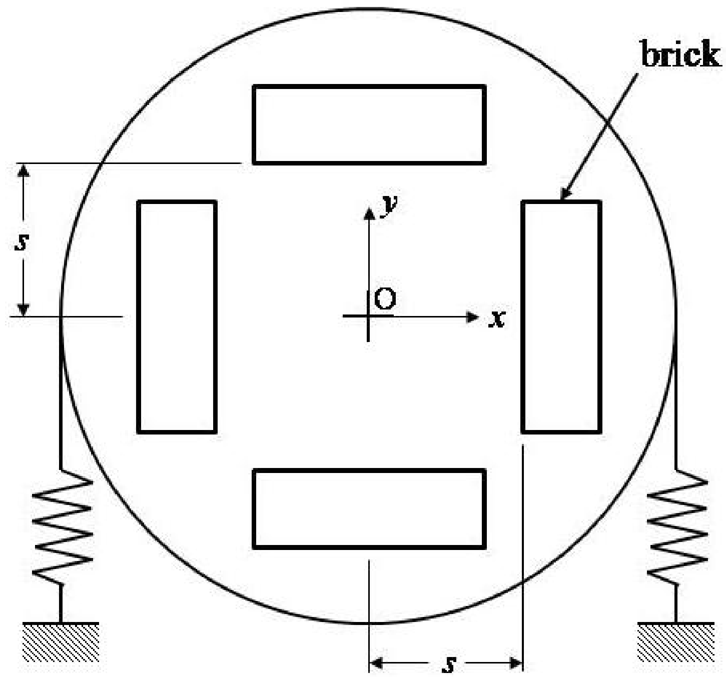

Figure 41. Validation test model (four-brick configuration)

Taking the series of bricks to be one test object, the inertia of the object can be determined by

$$I_{\text{theoretical}} = 4\left[\frac{m_{\text{brick}}}{12}\left(l^2 + w^2\right) + m_{\text{brick}}\left(s + \frac{w}{2}\right)^2\right] \tag{102}$$

where s in this case equals 0.1524 m (6 in). The resulting theoretical inertia is 0.9182 kg-m^2, which, utilizing the platform inertia from the previous test, should account for more than 20% of the total system inertia. The iMachine was run five times with and without the test object mounted on the platform. The change in natural frequency when the test object is removed from the platform is clearly visible in Figure 42 and Figure 43, which illustrate a portion of the time response and frequency response, respectively. The maximum amplitude of the time response has been normalized for clarity. The average peak frequency (N=5) according to the FFT is 5.036 rad/s for the case with the test object and 5.622 rad/s when the object is removed.

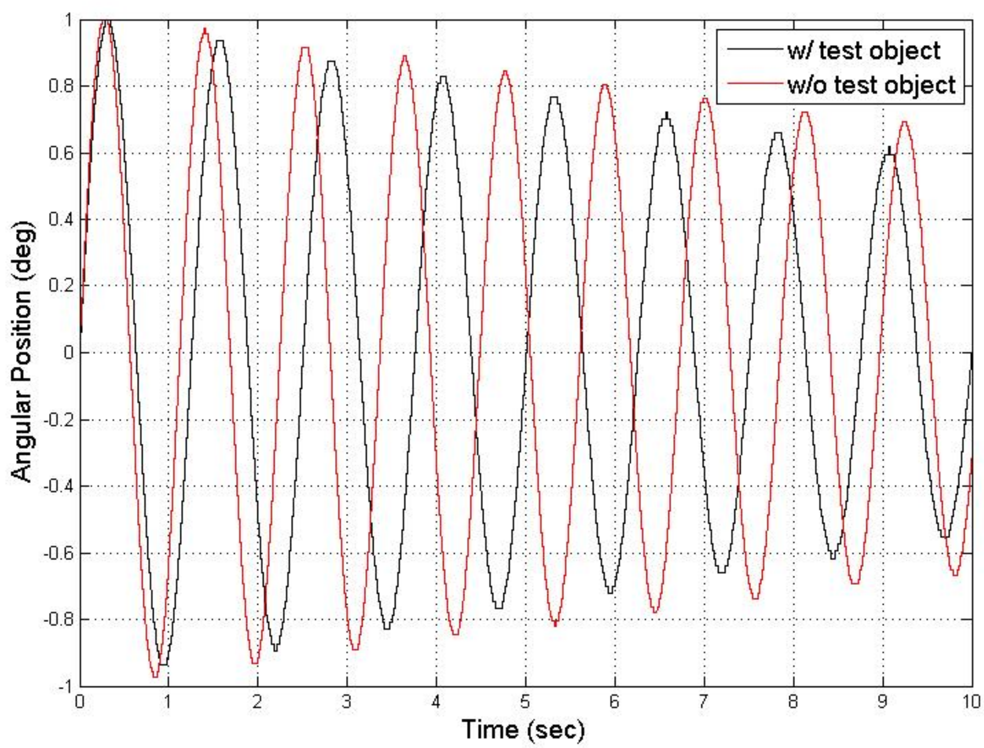

Figure 42. Comparison of the time-domain response of the system with and without the test object (four-brick configuration on platform)

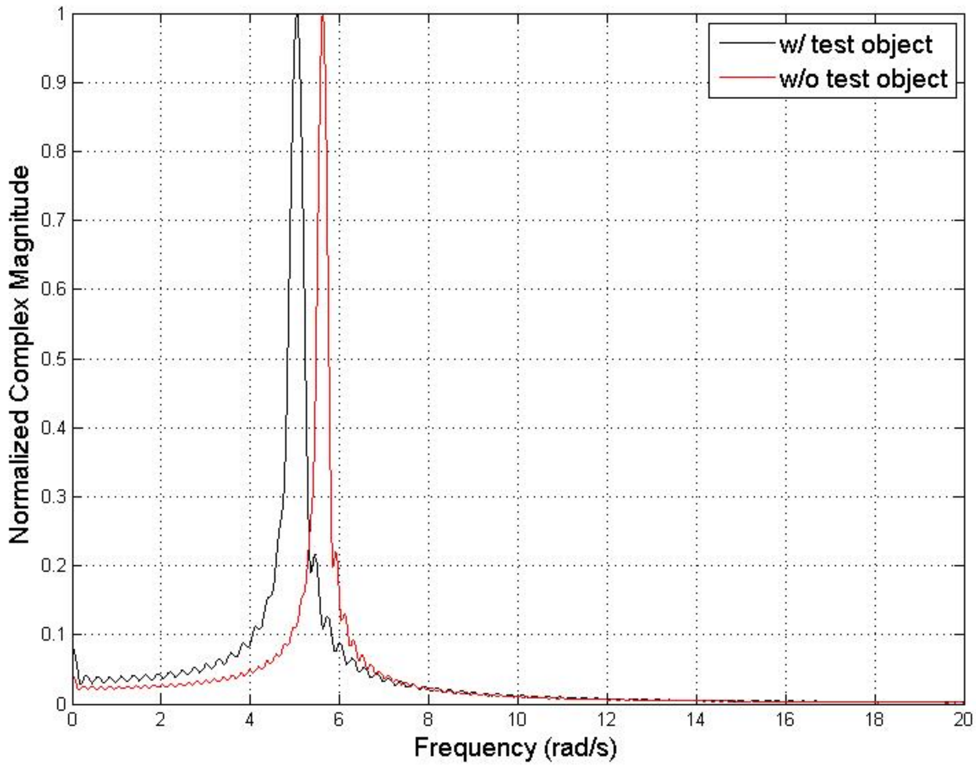

Figure 43. Comparison of the frequency-domain response of the system with and without the test object (four-brick configuration on platform)

Using the same computational approach as before, the mass of the test object equals 22.291 kg (98.77% accuracy), and the distance of the test object CG to the disk origin equals 3.828 mm. This CG offset has a negligible effect on the inertia of the test object (0.0003 kg-m^2). The important inertia terms involved in the derivation of the test object inertia are listed in Table 26-Table 29, and the relative error of the final result is computed in Table 30.

Table 26. Validation test (four-brick configuration on platform): inertia of the system about the disk origin (kg-m^2)

		Effective Spring Rate Method				
		mfr	zero	maxima	minima	fft
Natural Frequency Estimation Method	zero	4.0974	4.3501	4.2268	4.3305	4.2863
	maxima	4.1185	4.3724	4.2486	4.3527	4.3083
	minima	4.1278	4.3824	4.2582	4.3626	4.3181
	fft	4.1339	4.3888	4.2644	4.3690	4.3244

Table 27. Validation test (four-brick configuration on platform): inertia of the platform about the disk origin (kg-m^2)

		Effective Spring Rate Method				
		mfr	zero	maxima	minima	fft
Natural Frequency Estimation Method	zero	3.2957	3.4989	3.3998	3.4831	3.4476
	maxima	3.3078	3.5117	3.4122	3.4959	3.4602
	minima	3.3074	3.5113	3.4119	3.4955	3.4599
	fft	3.3169	3.5214	3.4217	3.5055	3.4698

Table 28. Validation test (four-brick configuration on platform): inertia of the test object about the disk origin (kg-m^2)

		Effective Spring Rate Method				
		mfr	zero	maxima	minima	fft
Natural Frequency Estimation Method	zero	0.8017	0.8512	0.8270	0.8473	0.8387
	maxima	0.8107	0.8607	0.8363	0.8568	0.8481
	minima	0.8204	0.8710	0.8463	0.8671	0.8582
	fft	0.8170	0.8673	0.8428	0.8634	0.8546

Table 29. Validation test (four-brick configuration on platform): inertia of the test object about its CG (kg-m^2)

		Effective Spring Rate Method				
		mfr	zero	maxima	minima	fft
Natural Frequency Estimation Method	zero	0.8014	0.8508	0.8267	0.8470	0.8383
	maxima	0.8104	0.8604	0.8360	0.8565	0.8478
	minima	0.8201	0.8707	0.8460	0.8668	0.8579
	fft	0.8166	0.8670	0.8424	0.8631	0.8543

Table 30. Validation test (four-brick configuration on platform): relative error of test object inertia (%)

		Effective Spring Rate Method				
		mfr	zero	maxima	minima	fft
Natural Frequency Estimation Method	zero	12.7183	7.3347	9.9604	7.7524	8.6939
	maxima	11.7378	6.2937	8.9490	6.7162	7.6683
	minima	10.6810	5.1717	7.8588	5.5992	6.5627
	fft	11.0580	5.5720	8.2477	5.9976	6.9571

These results are much better than the previous test, indicating that a larger inertia change can be measured more accurately. In this case, the calibrated effective spring rates yield better results than the manufacturer-provided data. This is expected because the spring calibration was performed *in situ* and should reflect the nominal operating conditions of the machine better. The average relative error when using the calibrated spring rate is 7.20%, with a minimum value of 5.17%.

To optimize the accuracy of the inertia measurement, the same brick configuration was tested on the disk alone. With the platform removed, the test object now accounts for almost 70% of the total system inertia. The iMachine was run five times with and without the test object mounted on the disk. The change in natural frequency when the test object is removed from the disk is clearly visible in Figure 44 and Figure 45, which illustrate a portion of the time response and frequency response, respectively. The maximum amplitude of the time response has been normalized for clarity. The average peak frequency (N=5) according to the FFT is 9.043 rad/s for the case with the test object and 16.037 rad/s when the object is removed.

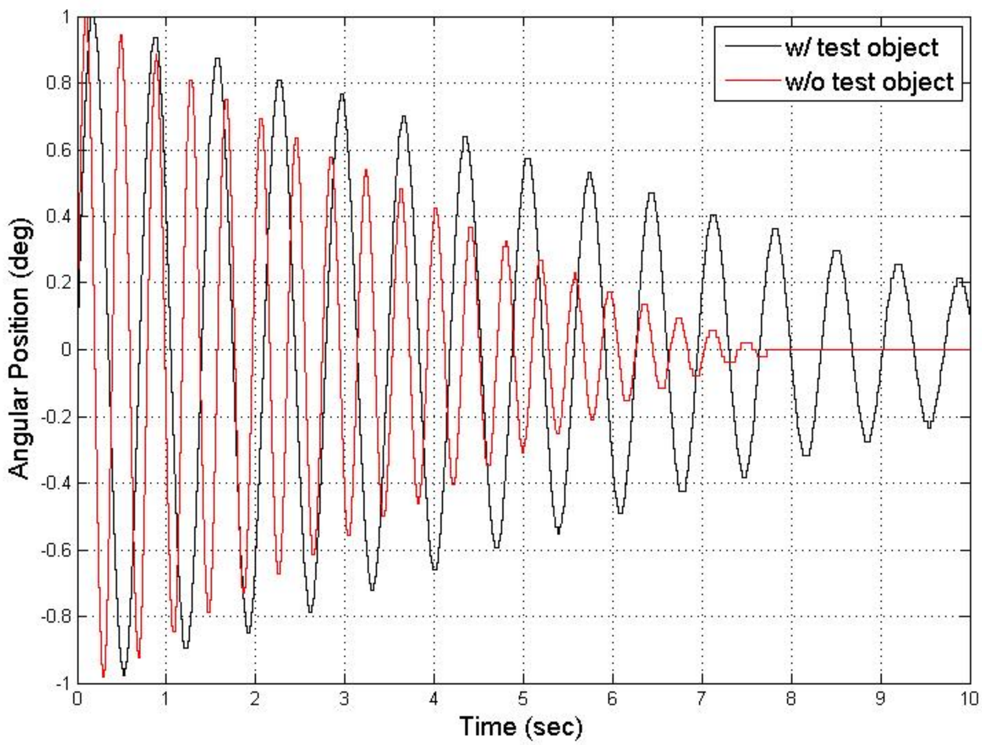

Figure 44. Comparison of the time-domain response of the system with and without the test object (four-brick configuration on disk)

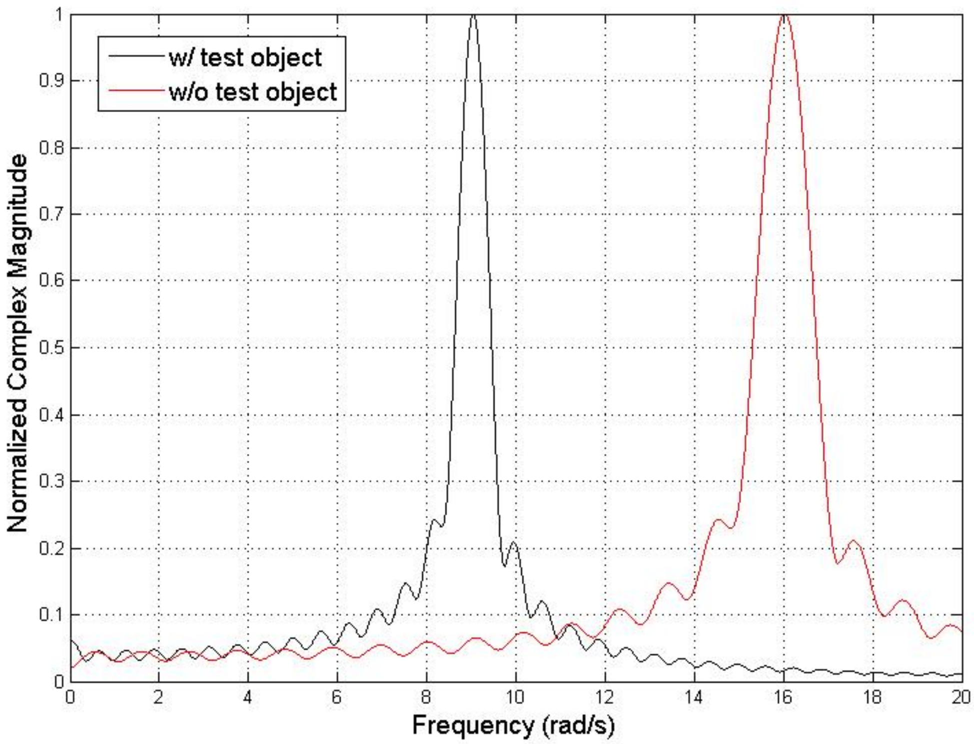

Figure 45. Comparison of the frequency-domain response of the system with and without the test object (four-brick configuration on disk)

Unfortunately, the mass and center of mass cannot be derived empirically using the iMachine in this configuration because the weight of the test object is not transferred through the load cells. Therein, for the inertia computation, the mass value measured by the scale is used and it is assumed that any offset in the test object CG has negligible effect on its inertia. This assumption is justified by noting that the mass measurement has been greater than 98% accurate in all tests and the parallel axis term due to CG offset has accounted for less than 0.4% of the total inertia. With this in mind, the important inertia terms involved in the derivation of the test object inertia are listed in Table 31-Table 33, and the relative error of the final result is computed in Table 34.

Table 31. Validation test (four-brick configuration on disk): inertia of the system about the disk origin (kg-m^2)

		Effective Spring Rate Method				
		mfr	zero	maxima	minima	fft
Natural Frequency Estimation Method	zero	1.2772	1.3559	1.3175	1.3498	1.3361
	maxima	1.2806	1.3596	1.3211	1.3535	1.3397
	minima	1.2842	1.3634	1.3248	1.3572	1.3434
	fft	1.2831	1.3622	1.3236	1.3561	1.3422

Table 32. Validation test (four-brick configuration on disk): inertia of the disk about the origin (kg-m^2)

		Effective Spring Rate Method				
		mfr	zero	maxima	minima	fft
Natural Frequency Estimation Method	zero	0.4058	0.4308	0.4186	0.4289	0.4245
	maxima	0.4078	0.4329	0.4206	0.4310	0.4266
	minima	0.4063	0.4314	0.4191	0.4294	0.4250
	fft	0.4076	0.4327	0.4204	0.4307	0.4263

Table 33. Validation test (four-brick configuration on disk): inertia of the test object about its CG (kg-m^2)

		Effective Spring Rate Method				
		mfr	zero	maxima	minima	fft
Natural Frequency Estimation Method	zero	0.8714	0.9251	0.8989	0.9209	0.9115
	maxima	0.8729	0.9267	0.9004	0.9225	0.9131
	minima	0.8779	0.9320	0.9056	0.9278	0.9184
	fft	0.8755	0.9295	0.9032	0.9253	0.9159

Table 34. Validation test (four-brick configuration on disk): relative error of test object inertia (%)

		Effective Spring Rate Method				
		mfr	zero	maxima	minima	fft
Natural Frequency Estimation Method	zero	5.0964	0.7550	2.0989	0.3010	0.7224
	maxima	4.9333	0.9281	1.9307	0.4733	0.5518
	minima	4.3860	1.5092	1.3660	1.0518	0.0208
	fft	4.6436	1.2357	1.6318	0.7796	0.2487

This test produced the most accurate results, with relative error as low as 0.02%. Once again, the calibrated spring rates appear to better than the manufacturer-provided data. The FFT method is a good choice for both estimating the spring rate during calibration and the natural frequency during testing. Therefore, it will be used as the method of choice in all future tests.

To show the resolution of the inertia calculation of the iMachine, define the ratio of the testpiece inertia to total system inertia as

$$I_{\text{ratio}} = \frac{\left(I_{zz}\right)_{\text{testpiece}}}{\left(I_{zz}^{\text{O}}\right)_{\text{sys}}} \tag{103}$$

Using the results from the three inertia validation tests described here, the relationship between I_{ratio} and the relative error of the inertia is graphically depicted in Figure 46. An exponential curve has been fitted to the data, resulting in the approximate relationship

$$e_{\text{rel}} = 26.59\exp\left(-6.78 I_{\text{ratio}}\right) \tag{104}$$

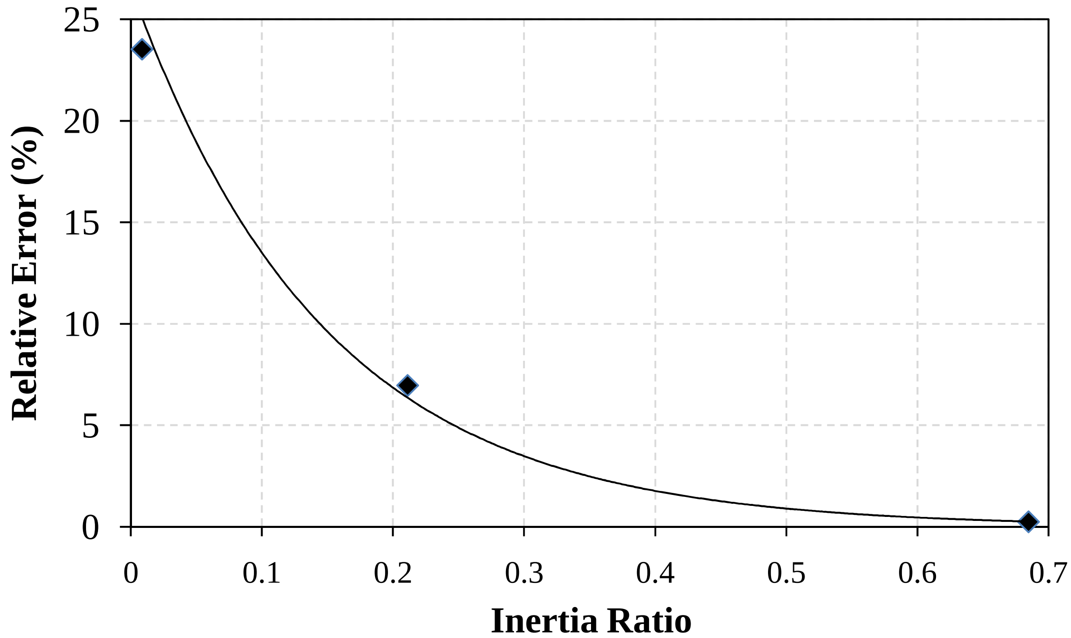

Figure 46. Plot of relative error versus inertia ratio

5.4 Wheelchair Testing

Now that accuracy estimates have been established through validation testing, a manual wheelchair is tested to gain an understanding of the effectiveness of the iMachine in measuring the inertial parameters of the primary object for which it was designed. The wheelchair that was tested is a Quickie GT model (Sunrise Medical, Longmont, CO) as shown mounted to the iMachine in Figure 47. The inertial properties of the wheelchair that were calculated from the test data are summarized in Table 35.

Figure 47. Quickie GT chair mounted on iMachine

Table 35. Wheelchair inertial properties, as determined by the iMachine

Parameter	Value	Units
m_{wc}	13.17	kg
x_{wc}	0.00348	m
y_{wc}	0.03525	m
$(I_{zz})_{WC}$	1.213	kg-m^2

The center of mass coordinates refer to the distance of the wheelchair CG from the origin of the disk. If a different relative point is desired, say the point of contact of the rear wheels, simply add the distance from that point to the origin to the coordinate results in Table 35. For the purpose of wheelchair energy estimation, however, the CG coordinates do not arise in the energy equation and are less important than the mass and moment of inertia. The inertia was computed using the FFT method for estimating both the calibrated spring rate and the natural frequency. The 95% confidence interval for the data (*N*=10) is [1.2042, 1.2225], which exhibits strong repeatability. Based on the assumption that the exponential fit described by (104) is valid, the wheelchair inertia measurement should have greater than 95.66% accuracy.

CHAPTER 6

CONCLUSIONS AND RECOMMENDATIONS

In this thesis, the design of an inertial properties measurement device has been presented. The analysis of validation tests demonstrates that the iMachine provides reliable and repeatable results. In particular, the mass of the test object had an average relative error less than 1%. The average relative error in the calculation of the *x* and *y*-coordinates of the center of mass was 0.891% and 1.99%, respectively. Despite the larger error in the *y*-direction, the CG offset proved to have negligible effect on the inertia calculation. The accuracy of the moment of inertia measurement relies upon the proportion of the system inertia represented by the test piece. As the inertia of the test piece increases relative to the platform, the measurement accuracy also increases. The wheelchair that was tested accounted for approximately 25% of the system inertia, and tests on objects with known mass properties show this case should have errors less than 5%. For tests when the AMPS is occupying the wheelchair, the error will be even less.

There are several recommendations that may improve the design and analysis of the iMachine for future research studies. With regard to the structural design, custom parts could be machined with greater precision to reduce errors. In particular, the current shaft tolerances allow the disk to tilt slightly, which adds to the measurement error because the system then rotates about an axis that is not vertical. Also, the rotating disk could be redesigned to decrease its inertia relative to the object being tested. A wheel with spokes is an example of a design that would achieve this goal, while maintaining the strength requirements due to the load transferred through the load cells.

With regard to the hardware, the optical encoder is a good choice for measuring the angular position of the rotating platform, especially with the commercial availability and relative inexpensiveness of high-precision encoders. Load cells with lower capacity could be used to improve resolution, so long as they meet the required maximum load of the device.

With regard to the measurement and data analysis approach, the FFT method of estimating the natural frequency yielded the best results. However, there is a tradeoff between accuracy and computational speed because decreasing the resolution of the transform requires an increase in the length of data, usually by a method such as zero padding. A curve-fitting algorithm for parameterizing a damped harmonic curve to the data would most likely improve the natural frequency estimation even more. In addition, the spring calibration test could be improved by increasing the difference between distances s_1 and s_2. Also, similarly to the mass variance test that was described in this thesis, an analysis of variance in the spring rate calculation could be improved by testing the diametrically-opposed bricks at a greater number of distinct distances. Finally, the relationship between the inertia ratio, I_{ratio}, and the relative percent error is most likely not best described by an exponential curve. Testing more objects with varying inertia could improve the development of the relationship described by the data in Figure 46 and would be a good avenue for further study.

Since the primary application of the iMachine is manual wheelchairs, the device has been designed to accommodate inertial properties ranging from an unoccupied manual wheelchair to a wheelchair occupied by the AMPS. However, the device could be used to estimate the moment of inertia of any irregularly-shaped rigid body. By altering the orientation of the test object on the platform, it is possible to compute the inertia about several different axes. If six distinct configurations are possible, the entire inertia tensor could theoretically be extracted from the test data. Ease of mounting the object rigidly to the platform may become an issue depending on shape complexity, so a more universal mounting design would be beneficial for future studies. If necessary, multiple platforms could be developed for specific ranges of inertia. Another way to increase the range of allowable inertia is to make the rotating risk modifiable. For instance, adding mounting locations for the load cells and springs increases the number of system configurations that could be altered depending on the object being tested.

This thesis lays the foundation for further study of wheelchair inertia by providing an apparatus and method capable of generating reliable and repeatable results for the inertial properties of irregular bodies. To characterize the system capability better, a Gauge Repeatability and Reproducibility (GRR) test based on the Analysis of Variance (ANOVA) random effects model should be conducted. In this way, the measurement variance due to instrumentation, operators, and test objects could be quantified. Other future research may include cataloguing the inertial properties of different wheelchairs, perhaps even on a component level such as the wheels, casters, frame, footrests, etc. An investigation into the cause of inertial differences could lead to improved wheelchair design for maximum propulsion efficiency. Other interesting topics of exploration for the iMachine include exploring the effect of caster orientation or varying occupant load distribution on wheelchair inertia.

REFERENCES

[1] Boynton, R.S., “Moment of Inertia Measuring Instrument.” U.S. Patent #3,693,413, 1972.

[2] Carpenter, D.A., “Mass Properties Measurement System.” U.S. Patent #4,161,876, 1979.

[3] Mastinu, G., Gobbi, M., and Doniselli, C., “Device for Measuring the Inertia Tensor of a Rigid Body.” U.S. Patent #7,278,295 B2, 2007.

[4] Pegram, J.P. and Anemaat, W.A., “Preliminary estimation of airplane moments of inertia using CAD solid modeling,” SAE Paper 2000-01-1700, 2000.

[5] Almeida, R.A.B., Urgueira, A.P.V., and Maia, N.M.M., “Further developments on the estimation of rigid body properties from experimental data,” *Mechanical Systems and Signal Processing*, vol. 24, pp. 1391-1408, 2010.

[6] Ogata, K., System Dynamics, 4th ed., Pearson Prentice Hall, Upper Saddle River, New Jersey: 2004, pp. 60-70, 82-83, 388-396.

[7] du Bois, J.L., Lieven, N.A.J., and Adhikari, S., “Error Analysis in Trifilar Inertia Measurements,” *Experimental Mechanics*, vol. 49, issue 4, pp. 533-540, 2009.

[8] Ringegni, P.L., Actis, M.D., and Patanella, A.J., “An experimental technique for determining mass inertial properties of irregular shape bodies and mechanical assemblies,” *Measurement*, vol. 29, issue 1, pp. 63-75, 2001.

[9] Zhi-Chao, H., *et al.*, (2009). “A new trifilar pendulum approach to identify all inertia parameters of a rigid body or assembly,” *Mechanism and Machine Theory*, vol. 44, issue 6, pp. 1270-1280.

[10] Griffiths, I.W., Watkins, J., and Sharpe, D., “Measuring the moment of inertia of the human body by a rotating platform method,” *American Journal of Physics*, vol. 73, issue 1, pp. 85-93, 2005.

[11] Kauzlarich, J.J. and Thacker, J.G., “A theory of wheelchair wheelie performance,” *Journal of Rehabilitation Research and Development*, vol. 24, no. 2, pp. 67-80, 1987.

[12] Ding, D., *et al.*, “Analysis of Driving Backward in an Electric-Powered Wheelchair,” *IEEE Transactions on Control Systems Technology*, vol. 12, no. 6, pp. 934-943, 2004.

[13] Wang, H., *et al*., "An Experimental Method for Measuring the Moment of Inertia of an Electric Power Wheelchair," *Proceedings of the 29th Annual International Conference of the IEEE EMBS*, Lyon, France, 2007.

[14] Gere, J.M., Mechanics of Materials, 6th ed., Brooks/Cole, Belmont, CA: 2004, pp. 313-314, 614-616, 914.

[15] Ginsberg, J.H., Mechanical and Structural Vibrations, John Wiley and Sons, Inc., New York, NY: 2001, pp. 74-98, 121-175, 306-317.